Phase-field investigation on the non-equilibrium interface dynamics of rapid alloy solidification

by

Jeong Yun Choi

A dissertation submitted to the graduate faculty

in partial fulfillment of the requirements for the degree of

DOCTOR OF PHILOSOPHY

Major: Materials Science and Engineering

Program of Study Committee:
Ralph E. Napolitano, Major Professor
Iver Anderson
Scott Chumbley
Richard LeSar
Xueyu Song

Iowa State University

Ames, Iowa

2011

TABLE OF CONTENTS

LIST OF TABLES

LIST OF FIGURES

EXECUTIVE SUMMARY

The research program reported here is focused on critical issues that represent conspicuous gaps in current understanding of rapid solidification, limiting our ability to predict and control microstructural evolution (i.e. morphological dynamics and microsegregation) at high undercooling, where conditions depart significantly from local equilibrium. More specifically, through careful application of phase-field modeling, using appropriate thin-interface and anti-trapping corrections and addressing important details such as transient effects and a velocity-dependent (i.e. adaptive) numerics, the current analysis provides a reasonable simulation-based picture of non-equilibrium solute partitioning and the corresponding oscillatory dynamics associated with single-phase rapid solidification and show that this method is a suitable means for a self-consistent simulation of transient behavior and operating point selection under rapid growth conditions. Moving beyond the limitations of conventional theoretical/analytical treatments of non-equilibrium solute partitioning, these results serve to substantiate recent experimental findings and analytical treatments for single-phase rapid solidification.

The departure from the equilibrium solid concentration at the solid-liquid interface was often observed during rapid solidification, and the energetic associated non-equilibrium solute partitioning has been treated in detail, providing possible ranges of interface concentrations for a given growth condition. Use of these treatments for analytical description of specific single-phase dendritic and cellular operating point selection, however, requires a model for solute partitioning under a given set of growth conditions. Therefore, analytical solute trapping models which describe the chemical partitioning as a function of steady state interface velocities have been developed and widely utilized in most of the theoretical investigations of rapid solidification. However, these solute trapping models are not rigorously verified due

to the difficulty in experimentally measuring under rapid growth conditions. Moreover, since these solute trapping models include kinetic parameters which are difficult to directly measure from experiments, application of the solute trapping models or the associated analytic rapid solidification model is limited. These theoretical models for steady state rapid solidification which incorporate the solute trapping models do not describe the interdependency of solute diffusion, interface kinetics, and alloy thermodynamics.

The phase-field approach allows calculating, spontaneously, the non-equilibrium growth effects of alloys and the associated time-dependent growth dynamics, without making the assumptions that solute partitioning is an explicit function of velocity, as is the current convention. In the research described here, by utilizing the phase-field model in the thin-interface limit, incorporating the anti-trapping current term, more quantitatively valid interface kinetics and solute diffusion across the interface are calculated. In order to sufficiently resolve the physical length scales (i.e. interface thickness and diffusion boundary length), grid spacings are continually adjusted in calculations.

The full trajectories of transient planar growth dynamics under rapid directional solidification conditions with different pulling velocities are described. As a validation of a model, the predicted steady state conditions are consistent with the analytic approach for rapid growth. It was confirmed that rapid interface dynamics exhibits the abrupt acceleration of the planar front when the effect of the non-equilibrium solute partitioning at the interface becomes significant. This is consistent with the previous linear stability analysis for the non-equilibrium interface dynamics. With an appropriate growth condition, the continuous oscillation dynamics was able to be simulated using continually adjusting grid spacings. This oscillatory dynamics including instantaneous jump of interface velocities are consistent with a previous phenomenological model by and a numerical investigation, which may cause the formation of banded structures. Additionally, the selection of the steady state growth dynamics in the highly undercooled melt is demonstrated. The transition of the growth morphology, interface velocity selection, and solute trapping phenomenon with increasing melt supersaturations was described by the phase-field simulation. The tip selection for the dendritic growth was consistent with

Ivantsov's function, and the non-equilibrium chemical partitioning behavior shows good qualitative agreement with the Aziz's solute trapping model even though the model parameter(V_D) remains as an arbitrary constant. This work is able to show the possibility of comprehensive description of rapid alloy growth over the entire time-dependent non-equilibrium phenomenon.

In addition, the simulations carried out here predict, for the first time, the full scope of behavior, from the initial transient to the steady-state conditions, where departure from equilibrium partitioning may lead to oscillations in composition, velocity, and interface temperature or may lead to a far-from-equilibrium steady-state. Such predictive capability is a necessary prerequisite to more comprehensive modeling of morphological evolution and, therefore, of significant importance.

CHAPTER 1. INTRODUCTION

The solidification microstructure from the liquid of a metal system shows a variety of morphologies, which are determined by the competition and selection between phases depending on the solidification process. Understanding the influence of solidification conditions and the corresponding selection mechanism of the growth dynamics to form the morphologies is the key research issue in the solidification study. Much has been analyzed about solidification microstructure evolution and the associated growth dynamics, experimentally and theoretically. In the conventional theoretical investigations, the local equilibrium constraint at the interface is applied and this is valid for low and moderate growth rates.

However, the local equilibrium condition at the solid-liquid interface is no longer valid in a highly driven solidification condition. When the growth rate is comparable with the atomic diffusion velocity across the solid-liquid interface, the solutal element cannot be rejected fast enough into the liquid ahead of the interface and is trapped in the solid phase, which results in the failure of the retainment of the local equilibrium condition at the interface. This thermodynamically non-equilibrium chemical partitioning at the solid-liquid interface alters the driving force for growth, the growth velocity, and the morphologies. As a result, the phases with non-equilibrium concentration have been observed in the rapidly solidified materials. This non-equilibrium interface concentration cannot be predicted by the purely thermodynamical approach which gives us only a range of thermodynamically possible interface compositions[1]. Semi-empirical models for the non-equilibrium chemical partitioning have been widely used for the analysis of rapid alloy solidification[53, 3]. However, the dependency of the degree of chemical partitioning on the interface velocity which the models describe is not rigorously verified since the quantitative experimental measurement of rapid growth dynamics

is very challenging[33, 36, 93]. Moreover, these models require adjustable parameters which are also difficult to measure experimentally. And more critically, the interface compositions, velocity, and morphology are selected by the interplay of themselves during the growth process. Therefore, the interface concentration may not be able to be simply described as a function of the interface velocity, as in the solute trapping models.

The analytical theories of the rapid solidification of alloys have been developed by considering the limitation of atomic kinetic attachment as well as the solute trapping phenomenon. The steady state temperature of the planar interface has been described as a function of the steady state velocities[25]. In addition, by incorporating the dendrite tip selection theories, it could be possible to analyze the steady state rapid dendritic growth[51, 56, 58]. The rapid dendritic models have been fitted to the experimental measurements and the good agreement has been shown. However, these fit has been done with several adjustable parameters which can be hardly determined experimentally. These models are limited to the steady state dendritic growth, and thus it is not appropriate to describe the dynamic morphology evolution which might be controlled by the dynamic interplay of the chemical partitioning and the interface dynamics.

Banded structure is the interesting morphology which is considered that the dynamic selection of the interface conditions is the main mechanism of the structure formation in the rapid alloy solidification process. This microstructure is characterized by the alternating structures of dendritic/eutectic and planar growth, and has been observed in many alloy solidifications[66]. By considering both the velocity dependent solute partition model and the limitation of atomic kinetic attachment, the interface stability analysis has found the time-dependent oscillatory instability of planar interface with the velocities near the absolute stability limit velocity of a planar interface[77, 78]. In this stability analysis, it also has been shown that the oscillatory instability is controlled by the non-equilibrium solidification effects, i.e. velocity dependent chemical partitioning and the atomic kinetic attachment, and it has been presumed that this time-dependent instability may trigger the interface dynamics for the banded structure formation. In regard to the interface dynamics, the phenomenological model has been suggested

for the banded structure formation by Kurz and co-workers[54]. In this model, cyclic interface dynamics occurs between the stable dendritic/eutectic growth state and stable planar growth state, when the pulling velocity in the directional solidification condition corresponds to the velocity range where the steady state interface temperature increases with velocities. Karma and Sarkissian showed that the time-dependent cyclic instability of planar interface can actually leads the oscillatory interface dynamics, by a numerical analysis with a sharp phase interface and the solute trapping model[80, 81]. In this numerical analysis, the time-periodic change of the interface dynamics which is consistent with the previous phenomenological banded structure formation dynamics, and the effect of the latent heat have been successfully shown. For more rigorous description of non-equilibrium interface dynamics, the microstructure evolution has to be considered, but it is very challenging to describe the morphology evolution associated with the non-equilibrium interface dynamics with the sharp-interface numerical analysis.

Phase-field simulation has been extensively used for studies of microstructure evolution, due to the fact that the phase-field method has some advantages over other numerical/analytical models. Without tracking the interface position, the evolution of phases and the diffusion process for the entire system can be calculated simultaneously. Moreover, it has the capability of installing the surface tension and interface anisotropy effects straightforwardly. In the phase-field simulation, the interface dynamics is driven by only the dissipation process of the thermodynamical solidification driving energy. Thus, the phase-field model is not limited to the alloy concentration or the shape of the equilibrium phase-diagram as long as the thermodynamical solidification driving energy could be properly given. During a recent decade, a more quantitatively reliable phase-field model was developed and validated through comparison with experimental data, analytical theory, and other numerical simulation results. It has been used as a tool to investigate a number of aspects of solidification phenomena.

The phase-field simulation is a promising method specifically to investigate the non-equilibrium interface dynamics and the corresponding morphology evolution. The diffused interface in the phase-field model allows calculating spontaneously the non-equilibrium growth effects of alloys and the associated time-dependent growth dynamics, without the help of the pre-

scribed theories such as the solute trapping model[104]. In regard to rapid alloy solidification, the phase-field simulation has been widely used to show the phenomenological morphology evolutions[88, 89, 90]. In more quantitative studies, phase-field investigations have been used to describe the velocity-dependent chemical partitioning at the steady state planar interface and to compare it with the solute trapping models and some experimental measurements[92, 93]. In most phase-field investigations, it has been focused on a separate event which occurs during alloy rapid growth dynamics, and comprehensive interface dynamics has not been clearly shown. Conti demonstrated the time-periodic interface dynamics of planar direction growth[94], but the calculated dynamics was deviated from those in the previous phenomenological model and the sharp-interface numerical model. This might be caused by the failure to retain the numerical stability by allowing a sufficiently small grid spacing to resolve the dynamically changing length scales of physical properties around the solid-liquid interface. And also, the sharp-interface limit phase-field model which Conti used may gives rise the unphysical solute diffusion process in the interface region.

In the current work, we demonstrated the phase-field calculation results which describe the rapid interface dynamics associated with the non-equilibrium chemical partitioning. We utilized the thin-interface limit phase-field model with the anti-trapping current to ensure more quantitatively valid prediction. In addition, the grid spacings are adjusted to ensure the sufficient resolution for the interface region. By calculating transient planar growth behavior under directional growth conditions and the steady state morphologies in undercooled melts, we examined the influence of non-equilibrium chemical partitioning on the rapid growth dynamics and morphological selection. Since the interface conditions and the corresponding growth dynamics in extremely rapid solidification process is difficult to analyze experimentally, it is very important to present the possibility of such a comprehensive description of rapid growth dynamics as shown in the current work.

Chapter 2 will give the necessary background of the solute redistribution and associated transient interface dynamics in alloy solidification. Then, the studies of rapid alloy solidification including the investigation on the banded structure formation relevant to the current work

will be briefly reviewed. At the end of the Chapter 2, the previous significant studies of rapid solidification introduced throughout the chapter will be summarized in a table arranged in chronological order. Chapter 3 will present the critical questions that this work tackles. In Chapter 4, the phase-field model is briefly introduced and the governing equations and numerical methods used for the current work will be exposited. The Chapter 5 will show the calculated non-equilibrium interface dynamics and compare them with the analytical models for planar front and equiaxed growth morphologies. Finally, general conclusions from the present work and a brief suggestion for future work are provided in Chapter 6.

CHAPTER 2. LITERATURE REVIEW

2.1 Transient Growth Dynamics And Interface Stability

2.1.1 Local equilibrium condition at the solid-liquid interface

For more than fifty years, great effort has been focused on describing the solidification process of alloys from the melt. During the solidification of alloys, solute is emitted from the solid phase to the liquid phase due to the finite solubility of the solute in the solid phase. This limited accommodation of the solvent in the solid phase causes the rejected solute to pile up in front of the interface. For typical metallic alloy castings, crystal growth occurs sufficiently slowly, so as to ensure that the interface concentrations in both the solid and the liquid phases are equal to the values given by the equilibrium phase diagram of the alloy system (Figure 2.1); this interface condition is called the *local equilibrium* condition and the equilibrium partition coefficient, k_e, is defined as the ratio of the equilibrium solute concentration in the solid phase, c_S^e, to that in the liquid phase, c_L^e. In that case, the speed of solidification is controlled mostly by the transport rate of latent heat and solute atoms released from the solidifying crystal at the solid-liquid interface. If the interface temperature or the interface concentrations are known, the interface velocity and the evolving morphology can be described. To date, much of what has been studied regarding solidification has assumed a local equilibrium condition and, as a result, a valid description has been established.

2.1.2 Original observation of the planar front breakdown into perturbations

The breakdown of planar solid-liquid interface into cellular undulations was observed experimentally by Rutter-Chalmers[4] during directional solidification of dilute Sn-base binary

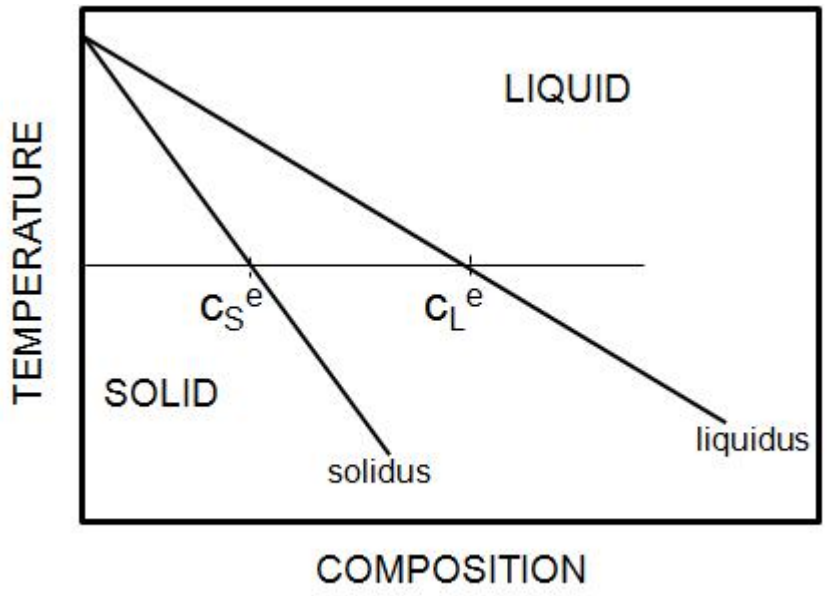

Figure 2.1 A portion of a schematic equilibrium phase diagram of a binary alloy. For a certain interface temperature, the interface solute concentration in the solid and the liquid, c_S^e and c_L^e, respectively, can be determined for the phase diagram.

alloys containing small amount of impurity such as Pb, Bi, Fe, Ag, and Cu and Pb-Sb alloys. A specimen was placed in a graphite boat and the solidification proceeded by movement of the furnace which surrounded the boat. By controlling the rate of the furnace motion, desired solidification rate was achieved. To observe morphologies of the solid-liquid interface, the interface was exposed by rapidly pouring the melt out from the boat. Figure 2.2 is an example of free solidification surface morphology obtained by decantation of the melt, showing cellular structures. The hexagonal shapes of the cells with straight cell boundaries were presumed to be a result of lateral growth near the cell tip during the decantation of the melt. Cross-sections of the cells further behind the tips were circular[5]. Transverse segregation of impurities in cell structures was also detected. The solute elements were most heavily concentrated at cell boundaries. In addition to this transverse segregation between cells, the average impurity concentration also gradually increased in the growth direction. In regard to the effect of growth conditions on the breakdown of planar front, it was observed that the appearance of cellular

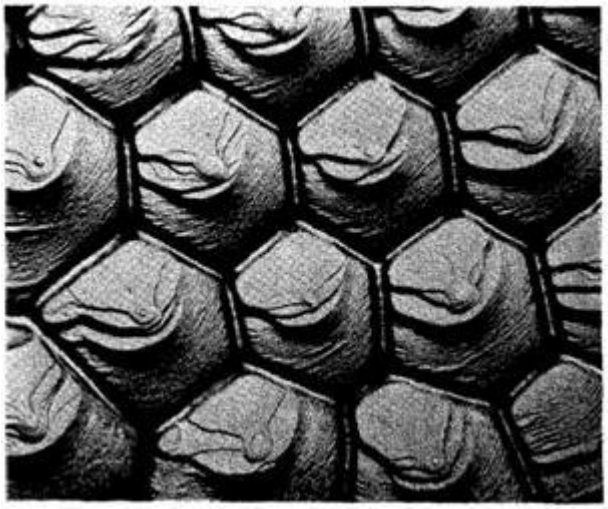

Figure 2.2 Cellular solid-liquid interface of a directionally solidifying Pb single crystal containing 88 ppm Ag exposed by decantation of the melt, observed by J. W. Rutter[6]

structures was suppressed with lower growth velocities, V, and a steeper temperature gradient, G. The cell size also depended on the V, G, and the solute concentration, c_0, in the alloys. Cell diameters decreased with increasing c_0 and decreased with increasing in V and G in the liquid.

A more extensive experimental investigation was carried out by Tiller-Rutter[7] to obtain a quantitative relationship between growth parameters at the onset of breakdown of a planar solid-liquid interface into cellular structures with Pb-base binary alloys. Results from experiments using wide ranges of G, V, and c_0 show that the breakdown of a planar front occurs when $c_0/(G/V)$ equals a critical value. For this transition, G/V was found to be an important parameter, rather than G or V individually. Cell diameters were inversely proportional with GV, and increased with c_0. The existence of a solute-rich layer in the liquid ahead of the solid-liquid interface was also experimentally confirmed in their investigation.

2.1.3 Solute redistribution analysis

Once the melt starts to solidify, solute gradually piles up in front of the solid-liquid interface in the liquid. After this short transient state, the growth reaches a steady state, after which

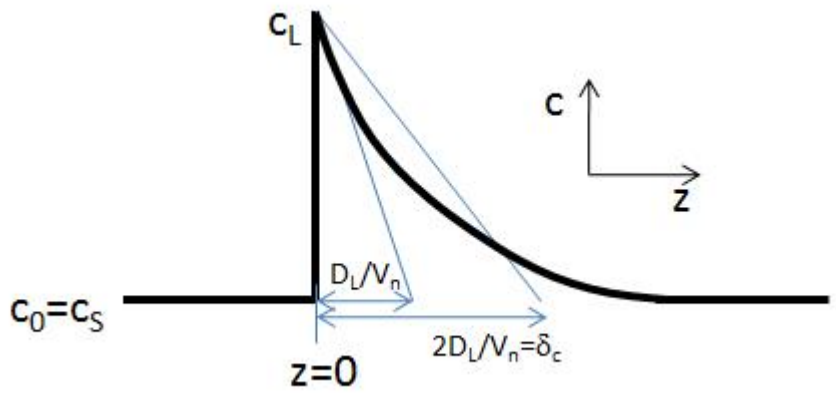

Figure 2.3 Steady state solute profile in front of the solid-liquid interface. The solid-liquid interface is at z=0 in the moving frame with V_n. At the steady state, the solid concentration is the same as c_0. The solute profile in the liquid can be described as an exponential function (Eq. 2.1a).

the solid concentration is uniform and equal to the far-field liquid concentration (or initial liquid concentration), c_0 (Figure 2.3). This solute redistribution during alloy growth was theoretically analyzed by Tiller-Rutter-Jackson-Chalmers[8]. To solve this simple case, we first consider one-dimensional steady-state growth of alloys with a velocity, V_n. In the moving frame with a velocity equal to V_n, the differential equations for chemical diffusion in the bulk phases can be simplified by considering only the steady state:

$$c_L(z) = c_0 + \Delta c_0 \exp(-\frac{V_n z}{D_L}) \tag{2.1a}$$

$$c_S = c_0 \tag{2.1b}$$

where z is the coordination of the moving frame (z=0 being the solid-liquid interface), $c_L(z)$ is the solute concentration in the liquid at z, $\Delta c_0 = c_0 \left[(1-k)/k\right]$, k is the partition coefficient which is the ratio of interfacial solute concentration in solid to that in liquid phase, and D_L is the solute diffusivity in the liquid. We can define the effective solute boundary layer thickness,

δ_c (Figure 2.3) which is the length scale where solute piles up in front of the interface:

$$\delta_c = 2D_L/V_n \tag{2.2}$$

This length scale is an important measure for the effect of solute diffusion on the growth process.

During the solidification of a small one-dimensional alloy system of which the size is shorter than the diffusion boundary layer thickness, δ_c, (such as the lateral growth of the second dendrite arms) we cannot expect the solute profile shown in Figure 2.3; thus, the solidification process cannot reach a steady state before it completely solidifies. In this case, the Scheil model can be used to predict the composition profile in the solid and liquid phases in the system, as a function of the solid phase fraction. In this small system, solute in the liquid can be regarded as completely mixed within a very short period of time compared to the time required for the interface to advance, whereas the solute diffusion in the solid is much slower than the interface velocity. Therefore, the assumptions of infinite solute diffusivity in the liquid and no solute diffusivity in the solid are reasonable. Under these assumptions, mass balance across the interface gives the solute concentration in the liquid phase as a function of solid phase fraction, f_S (Figure 2.4):

$$c_L = c_0/(1 - f_S)^{1-k_e} \tag{2.3}$$

This Scheil equation is valid for a normal growth rate where the local equilibrium condition at the interface can be assumed.

A more extreme case occurs when the solute diffusion in the solid phase is also faster than the growth velocity, resulting in a uniform concentration within each phase. The concentration profile as a function of f_S is described by the 'lever rule':

$$c_L = \frac{c_0}{1 - (1 - k_e)f_S} \tag{2.4}$$

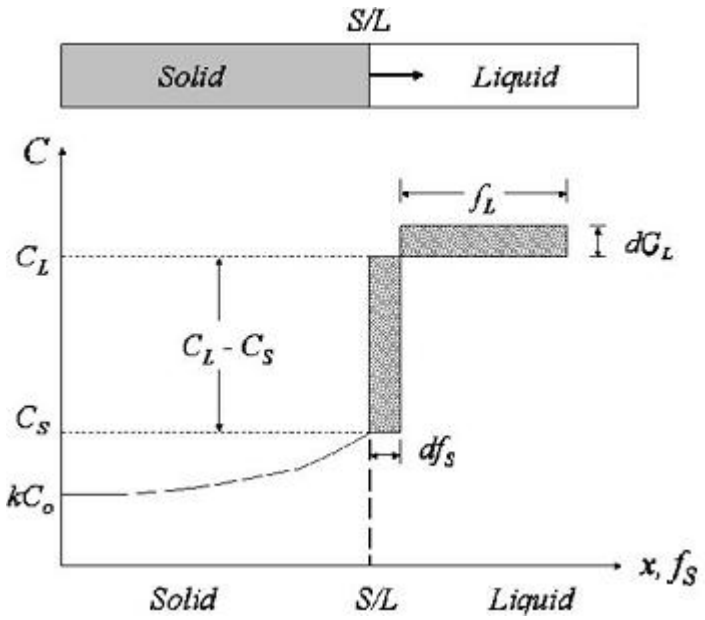

Figure 2.4 Scheil model assuming complete mixing in liquid and no diffusion in solid

For general solidification, the system size is much larger than δ_c and the steady state solute profile shown in Figure 2.3 can be obtained. Before a planar growth process reaches a steady state (Figure 2.5 b), an initiation stage is required to develop the solute boundary layer (Figure 2.5 a). This regime is called the initial transient. In this regime, the interfacial concentration on the liquid side, c_L^*, increases from c_0 to c_0/k, and the interfacial concentration on solid side, c_S^*, increases from kc_0 to c_0 until the steady state is reached. Figure 2.5 shows the directional solidification under the condition of a constant temperature gradient and a constant cooling rate. When we assume that the interface is in local equilibrium, the solidification starts at $T_L^e(c_0)$ (Figure 2.5 e). As the growth proceeds, solute piles up in front of the interface, and increases c_L^*, so that a lower interface temperature is required to freeze the more concentrated liquid phases. Therefore, during the initial transient period, T^* decrease from $T_L^e(c_0)$ to $T_S^e(c_0)$. When $T^* = T_S^e(c_0)$, mass flux balance, and therefore a steady state is achieved.

Smith, Tiller, and Rutter [9] obtained the analytical solution for the initial transient region, which is the stage before the steady state. Their assumptions include no diffusion in the solid, no convection, constant partition coefficient, local equilibrium at the interface, planar growth,

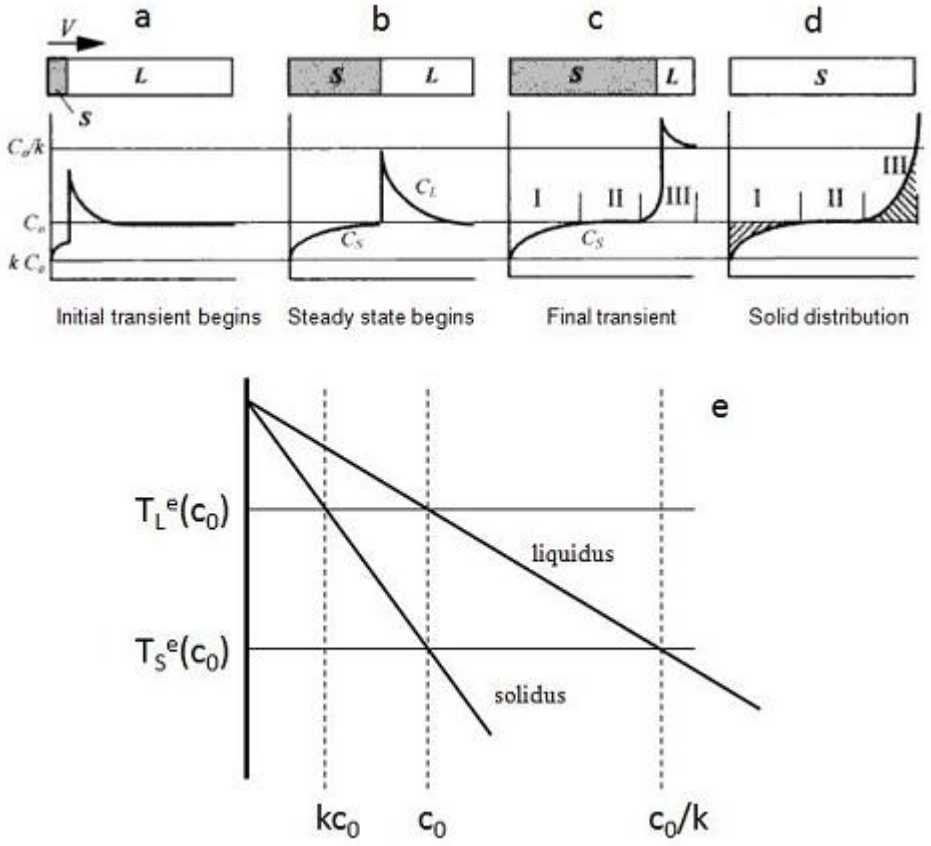

Figure 2.5 Solute distribution change during directional growth with a planar front. During directional growth of a confined specimen of alloys with nominal composition, c_0, solute distribution exhibits three different regimes: the initial transient regime (region I) for building up a solute boundary layer in front of the solid/liquid interface as the temperature decreases from $T_L^e(c_0)$ to $T_S^e(c_0)$, the steady state regime (region II) where the interface temperature maintains $T_S^e(c_0)$, and the final transient regime (region III) by end-effect.

and constant interface velocity. They calculated the liquid concentration at the interface for the transient region as

$$c_L^* = \frac{c_0}{2k}\left[1 + erf\left(\frac{\sqrt{(V_n/D_L)z}}{2}\right) + (2k-1)exp\left(-k(1-k)\frac{V_n}{D_L}z\right) erfc\left(\frac{2k-1}{2}\sqrt{\frac{V_n}{D_L}z}\right)\right] \tag{2.5}$$

When the tail of the solute boundary layer reaches the end of the system, the solute diffusion in liquid phase is obstructed such that c_L^* increases and T^* decreases below $T_L^e(c_0)$ (Figure 2.5 c).

2.1.4 Constitutional undercooling criterion

Based on the solute profile analysis, Tiller-Rutter-Jackson-Chalmers[8] explained the breakdown of a planar front during directional growth using the notion of *constitutional undercooling*. Planar growth is a special case, and it is easily perturbed by thermal, solutal or other types of noise. For pure materials, when the thermal gradient in the liquid phase is negative, the perturbed interface is more unstable and driven for growth so that it forms dendrites. For alloys, even if the thermal gradient in the liquid phase is positive, the constitutional undercooling in front of the interface makes the interface instable. The constitutional undercooling is caused by the solute diffusion boundary layer in front of the interface. In this boundary layer, the concentration exponentially decreases away from the interface, as shown by the dotted curve in Figure 2.6. For a system with $k_e < 1$, the liquidus temperature which depends on the concentration in the liquid, increases nonlinearly as shown by the Figure 2.6. When the thermal gradient is smaller than the liquidus temperature gradient, $G < mG_c$, where G_c is the solute concentration gradient in the liquid and m is the liquidus slope. When this is case, there is a region in front of the interface where the actual temperature (the broken line in Figure 2.6) is lower than the equilibrium liquidus temperature. Because the liquid in this region is constitutionally undercooled, the planar interface tends to be unstable, and if a small solid perturbation is created, it tends to grow. By substituting $V_n c_0 \left(1/k - 1\right)/D_L$ for $-G_c$,

the critical velocity for constitutional undercooling can be calculated as:

$$V_c = -\frac{GD_L}{mc_0(1/k-1)} = \frac{GD_L}{\Delta T_0} \tag{2.6}$$

where ΔT_0 is the temperature difference between the liquidus and the solidus for c_0. If the interface growth rate is lower than this constitutional undercooling limit, V_c, the planar interface is stable, otherwise it is unstable and likely to be transformed into cells or dendrites.

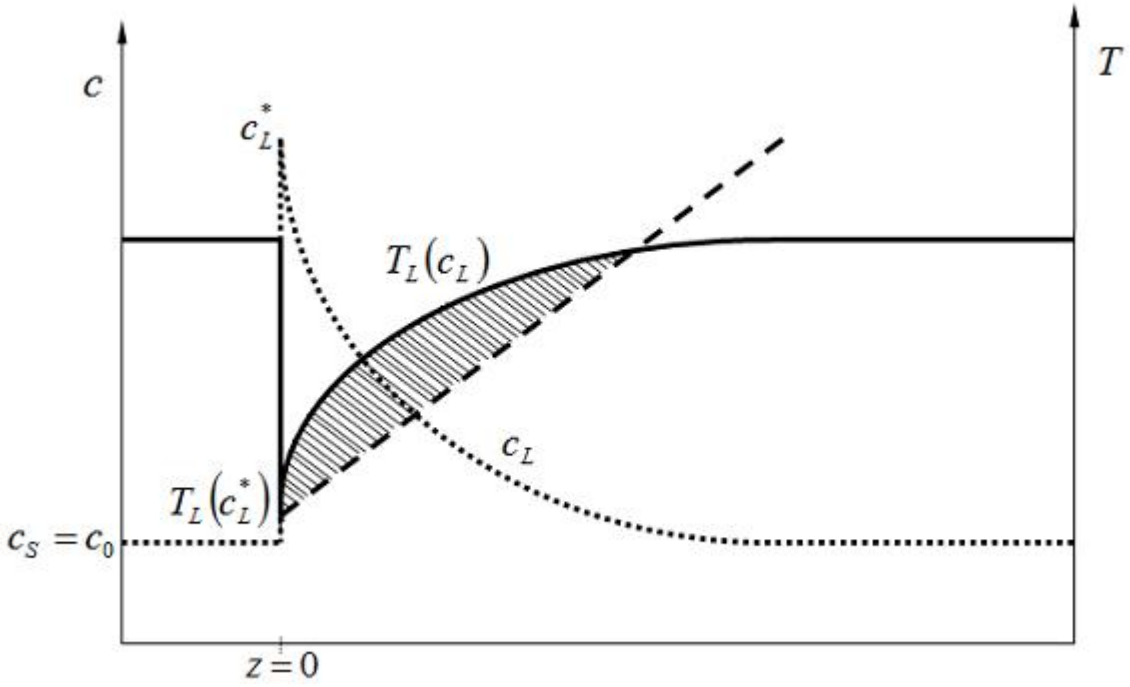

Figure 2.6 Schematic of constitutional undercooling. z=0 is the solid-liquid interface position during solidification. The dotted curve indicates solute concentration. The solid curve is the melting temperature for the solute concentration. The broken line represents the actual melt temperature. Due to the solute pile-up in front of the solid-liquid interface, the melting temperature increases with the distance, z. If the temperature gradient in the melt is lower than the gradient of T_L, the constitutional undercooling (the hatched region) occurs.

2.1.5 Instability criterion of steady state planar front

Mullins and Sekerka [10] performed a more precise analysis of instability of the perturbed interface by accounting for the capillary effect. They analyzed the scale of perturbation which makes the planar interface at steady state unstable. For this analysis they assumed local equilibrium at the interface, isotropic surface energy, no solute diffusion in the solid, and a constant partition coefficient. They introduced the mathematically perturbed interface as a sinusoidal function, $z = \epsilon \sin(\omega y)$ where ϵ is the amplitude of the perturbation, and ω is the wavenumber of the perturbation ($= 2\pi/\lambda$) (Figure 2.7), and calculated the concentration and temperature diffusion field in liquid phase. If we assume that the thermal gradient is identical in the liquid and the solid phases and ignore the latent heat effect, the original result of Mullins and Sekerka regarding the rate of the perturbation amplitude, $\dot{\epsilon}$, as a function of the wavelength of the perturbation, λ, can be simplified as:

$$\frac{\dot{\epsilon}}{\epsilon} = \frac{V_n}{mG_c}\left[-\Gamma\omega^2\left(\omega^* - \frac{V_n(1-k)}{D_L}\right) - G\left(\omega^* - \frac{V_n(1-k)}{D_L}\right) + mG_c\left(\omega^* - \frac{V_n}{D_L}\right)\right] \tag{2.7}$$

where $\omega^* = V_n/2D_L + \left[(V_n/2D_L)^2 + \omega^2\right]^{1/2}$. Figure 2.8 is the schematic of this result. Positive $\dot{\epsilon}/\epsilon$ means that the perturbation tends to grow, and negative $\dot{\epsilon}/\epsilon$ means that the perturbation tends to shrink so that the planar interface is favorable. As shown in Figure 2.8, the planar interface is only stable for very small wavelengths. As λ increases, a flat interface becomes unstable. For much larger λ, the rate of perturbation decreases due to the limitation of diffusion.

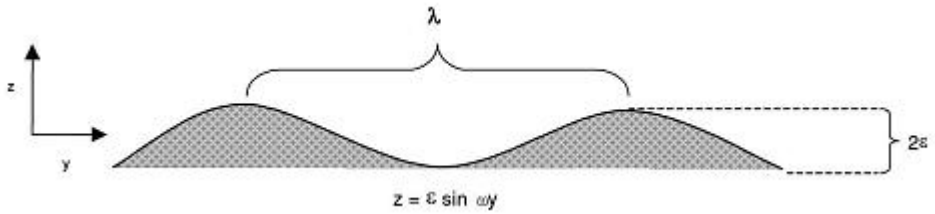

Figure 2.7 Mathematical perturbation of an interface for Mullins-Sekerka's instability analysis, with a wavelength, λ, and an amplitude, ϵ

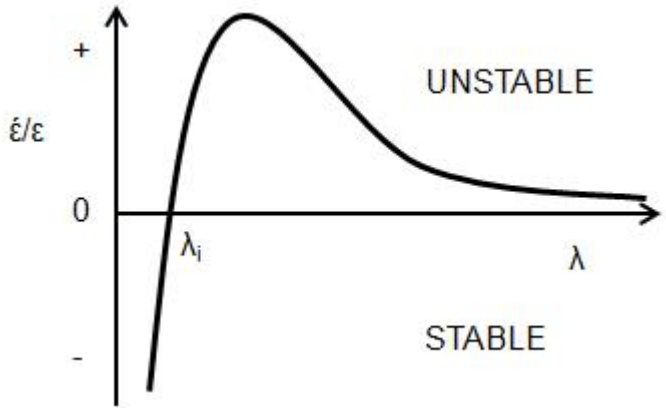

Figure 2.8 Rate of advancing amplitude of interface perturbations, $\dot{\epsilon}$, depending on the wavelength, λ, calculated by Mullins-Sekerka's perturbation analysis. λ_i is the critical wavelength of the stable perturbation.

2.1.6 Instability observations of planar front

While the instability of a planar interface for a given solidification condition has been predicted by Mullins-Sekerka[10], the way that an unstable plane front evolves with time has been experimentally observed by Trivedi-Somboonsuk[11], after the initial breakdown of a planar front in well characterized systems with a transparent material. The dynamics of pattern formation was examined from the time that an interface became unstable until the unstable pattern reorganized into a stable morphology. Figure 2.9 shows the sequence of events observed from the experiments. Solidification took place from left to right in the figures. Initially the system remained still and the solid-liquid interface was flat. The sequential events that occur after the abrupt starting motion of the thermal gradient with a constant rate are as follows:

1. The interface temperature, T^*, decreases since the initial interface velocity, V^*, might be slower than the constant rate of motion of the thermal gradient which is called the pulling velocity, V_P. While T^* decreases, the solidification starts and solute elements are rejected into the liquid ahead of the solid-liquid interface in order to maintain the local thermodynamic equilibrium at the interface. The rejected solute establishes a solute

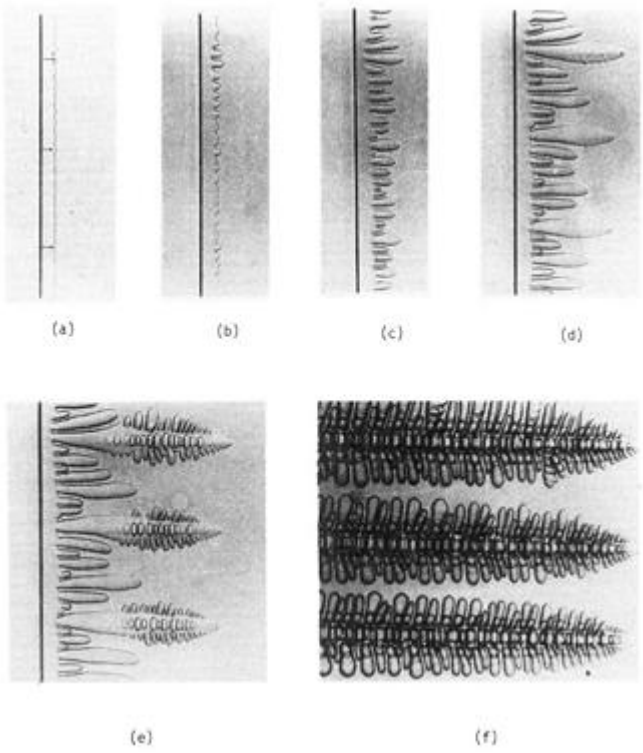

Figure 2.9 The morphology evolution in directional solidification of succinonitrile-acetone system observed by Trivedi-Somboonsuk[11]

boundary layer in front of the interface.

2. When solidification accelerates, the plane front becomes unstable as Mullins-Sekerka[10] predicted (Figure 2.9 (a) and (b)). The wavelength of perturbations at the initial breakdown of a planar interface which is clearly shown in Figure 2.9 (b) was found to be about an order of magnitude larger than the predicted one from Mullins-Sekerka's instability analysis with V_P. The initial breakdown of planar interface occurred during initial transient regime when $V^* < V_P$, whereas the classical Mullins-Sekerka analysis predicts the instability of a steady state planar interface; i.e. the interface becomes unstable during build-up of solute boundary layer in front of the solid-liquid interface. Trivedi-Somboonsuk[11] discussed that this instability of a planar front in a transient regime might govern the final steady state dendritic morphology.

3. As V* keeps increasing toward V_P, the perturbations grow into cell-like structures (Fig-

ure 2.9 (c)). While the cells grow and coarsen, they go through competitive selection. Some cells fall behind their neighbors and are eventually eliminated (Figure 2.9 (c) and (d)).

4. The cells that survive maintain a constant spacing and start to develop side branches (Figure 2.9 (d)) and (e)). The side-branching seems to be a noise-induced transition[12]. These dendrites are accelerated until they exhibits the steady state dendritic morphology with V_P (Figure 2.9 (f)).

As shown in the above sequence of evolution, the final steady state dendrite spacing is determined by a coarsening process of cells and dendrites that are grown from the initial breakdown of a planar front. As a result, the final steady state primary dendrite spacing is expected to be several times longer than the wavelength of the initial perturbation of the planar interface[11, 13, 14, 15].

Experimental observations have shown that final state morphologies actually have history dependency [11, 14]. Under precisely prescribed growth conditions and sample preparation, the same 'history' could be achieved and the final dendrite spacing was reproducible. Since the pattern selection process starts to operate during transient growth as shown in Figure 2.9, precise prediction of a final steady state pattern requires detailed knowledge of the entire history-dependent morphology evolution dynamics[16].

2.1.7 Analytical model of initial transient dynamics

Motivated by the Trivedi-Somboonsuk's observation[11] in the transient growth regime, Warren and Langer[13] developed the boundary layer model by which the acceleration of flat interface can be predicted during the initial transient directional solidification. In Tiller *et al.*'s analysis (Eq. 2.5), a constant interface velocity equal to the pulling velocity, V_P, was assumed. For real transient dynamics, however, the growth rate varies until it reaches the steady state. Warren and Langer assumed that: local equilibrium is always maintained at the solid-liquid interface, that G is spatially and temporally constant, and that the boundary layer concentration profile during the initial transient is the same as the equilibrium solute boundary

layer profile, i.e. Eq. 2.1a with $k = k_e$. Thus, $\delta_c = 2D_L/V^*$ where V^* is the interface velocity. After solving the solutal diffusion equation in a moving frame with velocity V_P, the resultant interface position in the moving frame, z^* is

$$\frac{dz^*}{dt} = \frac{2D_L(z^* - z_L^e)}{\delta_c(1-k_e)z^*} - V_P \tag{2.8}$$

and

$$\frac{d\delta_c}{dt} = \frac{4D_L(z_L^e - k_e z^*)}{\delta_c(1-k_e)z^*} - \frac{1}{z^* - z_L^e}\frac{dz^*}{dt} \tag{2.9}$$

where z_L^e is the position which corresponds to $T_L^e(c_0)$ in the moving frame given as $z_L^e = -mc_0/G$. m is the slope of the liquidus line and it is assumed to be constant. The numerical calculation of equations, Eq. 2.8 and Eq. 2.9, for z^* and δ_c gives the time-dependent interface velocity and solute profile information for the initial transient. This calculation can be started with the approximated analytical values of z^* and δ_c for a small time, t,

$$\delta_c \approx \sqrt{\frac{8D_L t}{3}} \tag{2.10}$$

and

$$z^* \approx z_L^e - V_P t + \frac{V_P\sqrt{2D_L}}{\sqrt{3}|z^*|(1-k_e)}t^{3/2} \tag{2.11}$$

As shown in Figure 2.10, this model can predict the oscillation behavior of z^* and δ_c with time. The results show the oscillatory dynamics of z* and δ_c, but these parameters directly represent the interface temperature, T*, and the interface velocity, V*, respectively, since $\delta_c = 2D_L/V^*$ was assumed in this calculation and the temperature profile was fixed in the system with a moving frame.

For a low enough V_P, there are no oscillatory dynamics. The amplitude of this oscillation increases with V_P. Therefore, δ_c becomes zero for a critical V_P and the calculation cannot proceed after that moment. This limitation of the model is a result of the purely solute diffusion-controlled growth that this model is based on. This is reasonable only for 'low/moderate' rate growth. In rapid growth, the solute pile-up in front of the solid-liquid interface decreases with

velocity, resulting in the transition from diffusion-controlled growth to kinetic-limited growth. Thus, the interface mobility should be considered.

Based on this calculation of the initial transient planar interface dynamics, Warren-Langer [13] then calculated the initial instability wavelength at the onset of instability of a planar interface in a transient regime and subsequently the final steady state primary dendrite spacing. The result of this model was in good agreement with Trivedi-Somboonsuk's measurements[11] and deviated from Mullins-Sekerka's stability analysis result in the steady state. This result reassures the Trivedi-Somboonsuk's observation that the initial breakdown on the planar interface occurs during the initial transient growth regime, instead of the steady state.

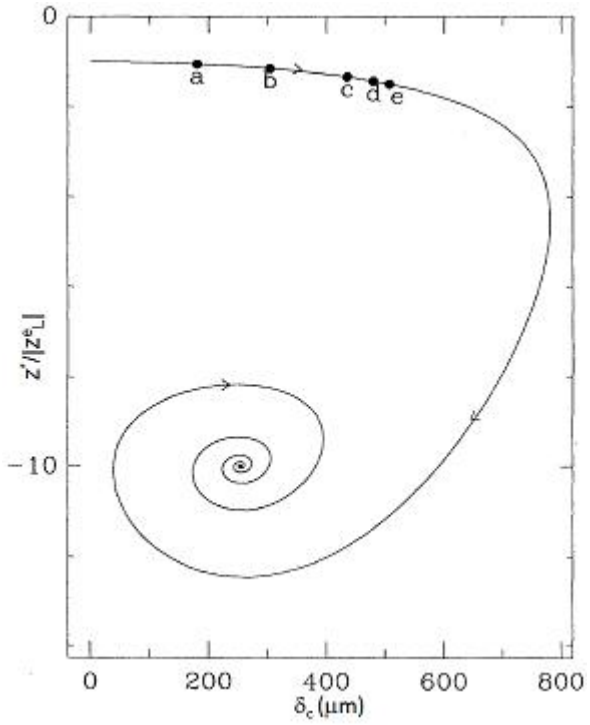

Figure 2.10 Interface trajectory during planar directional growth in terms of interface position (z^*) and boundary layer thickness (δ_c) calculated by the Warren and Langer's boundary-layer model [13] with $V_P = 10\mu m/s$ and $G = 67K/cm$. Time a corresponds to 10 sec, b to 30 sec, c to 70 sec, d to 90 sec, and e to 105 sec.

2.2 Rapid Solidification

2.2.1 Early interesting observation of solute trapping in rapid solidification

In the typical solidification condition, the local equilibrium condition at the solid-liquid interface is always retained; for a given interface temperature, T^*, the liquid-side and the solid-side interface concentrations, c_L^* and c_S^*, are determined by the equilibrium phase diagram and the values are c_L^e and c_S^e, respectively (Figure 2.1). It was observed, however, that the solute concentration in rapidly solidified alloy materials could deviate from the value of the equilibrium phase diagram[17]. In a chill casting of molten Al-Cu binary alloys[18], the Cu concentration in the solid phase was found to be the same as the initial melt composition although the corresponding k_e is about 0.17. In a splat quenching of Zn-Cd alloys[19], solid compositions higher than the maximum solid solute solubility of Zn rich Zn-Cd alloy were observed. Since the maximum solid solubility of Zn-Cd alloys occurs at a temperature above that of the eutectic temperature, this observation implies that the deviation of the solid composition from the equilibrium solid composition might not be just a metastable solidus composition, i.e. extension of the equilibrium solidus curve to the eutectic region into the phase-diagram. Re-growth of alloys from laser-induced melting[20, 21] also showed remarkable deviation of solid composition from the equilibrium values. In White *et al.*'s work[22], Si substrates doped with B, As, P, Sb, Ga, In and Bi elements were laser annealed. The partition coefficients were obtained from the measured concentration profiles of doped elements [22, 23, 24]. The resultant partition coefficients were higher than the equilibrium values. It was concluded that with such a fast interface motion, the local equilibrium condition was no longer valid.

2.2.2 Early theoretical treatment of rapid solidification

The mathematical description of solidification can be given by differential equations for heat and solute diffusions in solid and liquid phases, that describe the transport of excess solute atoms and the latent heat released from the moving interface into the bulk phases. To solve these diffusion equations, the initial conditions and the interface boundary conditions are required since these diffusion equations are separately applied for each phase. The bound-

ary conditions are comprised of the continuity equation of the temperature field across the interface, the conservation equations of heat and mass, and the interface response functions. The interface response function describes the response of the interface to the instantaneous interface condition and shows the relationship between the all of the variables which represent the interface condition, such as the interface velocity, the interface concentrations at the solid-side and the liquid-side, the interface temperature, the interface orientation, and the defect structure of the interface[1].

If we consider only thermodynamic variables, the response functions of binary alloys could be expressed by two functions which describe the interface temperature, T^*, and the solid-side interface concentration, c_S^*, in terms of the interface velocity, V^*, and the liquid-side interface concentration, c_L^*, written as follows when the interface curvature effect on T^* is ignored[1]:

$$T^* = T\left(V^*, c_L^*\right) \tag{2.12}$$

$$c_S^* = c_L^* k\left(V^*, c_L^*\right) \tag{2.13}$$

where k is a chemical partition coefficient at the interface, representing the ratio of c_S^* to c_L^*.

With regard to the second response function (Eq. 2.13), Baker and Cahn[1] thermodynamically analyzed the interface concentration during rapid solidification and showed that the possible ranges of c_S^* and c_L^* for a given T^* are bounded by thermodynamics. Figure 2.11 shows the molar free energy of solid and liquid phases vs. composition at a fixed temperature. The equilibrium between the two phases can be represented by the common tangent line, implying that the equal chemical potentials of the solute element between the phases ($\mu_L^B = \mu_S^B$). This common tangent gives c_S^e and c_L^e for the equilibrium phase diagram of the system shown in Figure 2.1. Figure 2.12 represents the non-equilibrium state at the interface for a given temperature. ΔG represents the free energy decrease when an infinitesimal amount of solid with c_S^* forms from a large amount of liquid with composition c_L^*. During solidification with

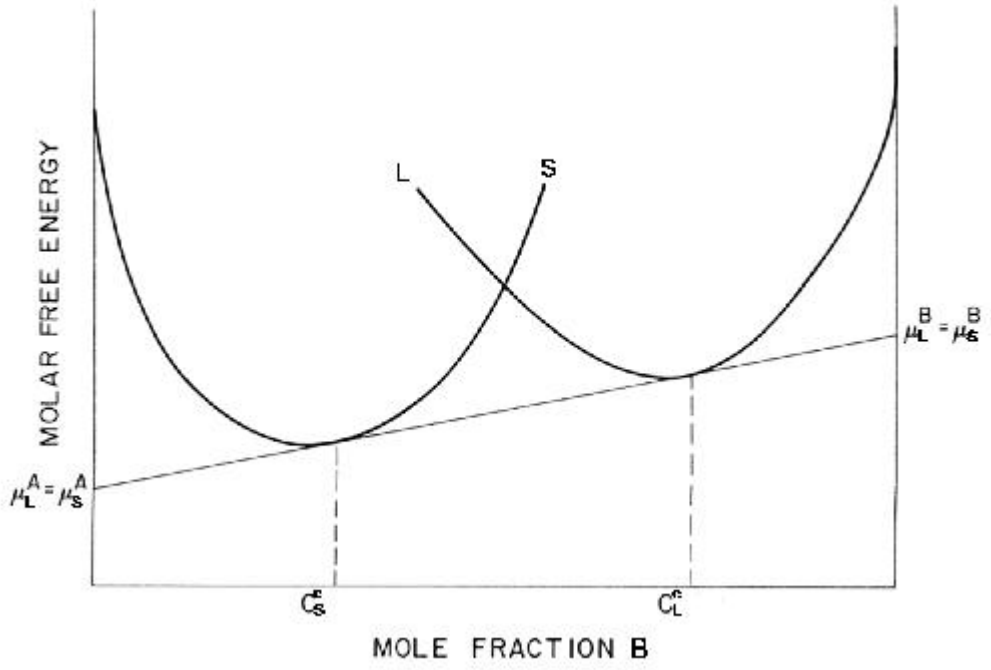

Figure 2.11 Molar free energy curves of the liquid phase (L) and the solid phase (S) for a binary system: μ is the chemical potential, and superscripts, A and B, represents the solvent and solute elements, respectively.

this interface condition, the chemical potential of a solute element could increase across the phase interface, i.e. $\mu_L^B < \mu_S^B$. Baker and Cahn[19] introduced the notion of "solute trapping" during rapid solidification of alloys for which the chemical potential of the solute element increases. This results in a larger partition coefficient at the solid-liquid interface compared to the equilibrium value. Since a net decrease in free energy, ΔG, should occur for the solidification of a liquid with composition c_L^*, the range of thermodynamically possible compositions for which a solid phase could solidify with a composition c_L^* is from c_S^1 to c_S^2. This range of possible c_S^* is schematically represented for various c_L^* at a fixed temperature in Figure 2.13[1] and, alternatively, for various temperatures for a fixed c_L^* in Figure 2.14[25]. The T_0 curve in Figure 2.14 indicates the concentration where the Gibbs free energy curves of the solid and the liquid phases at a fixed temperature are overlapping.

This thermodynamic analysis can give a general range of possible k values for a given c_L^*

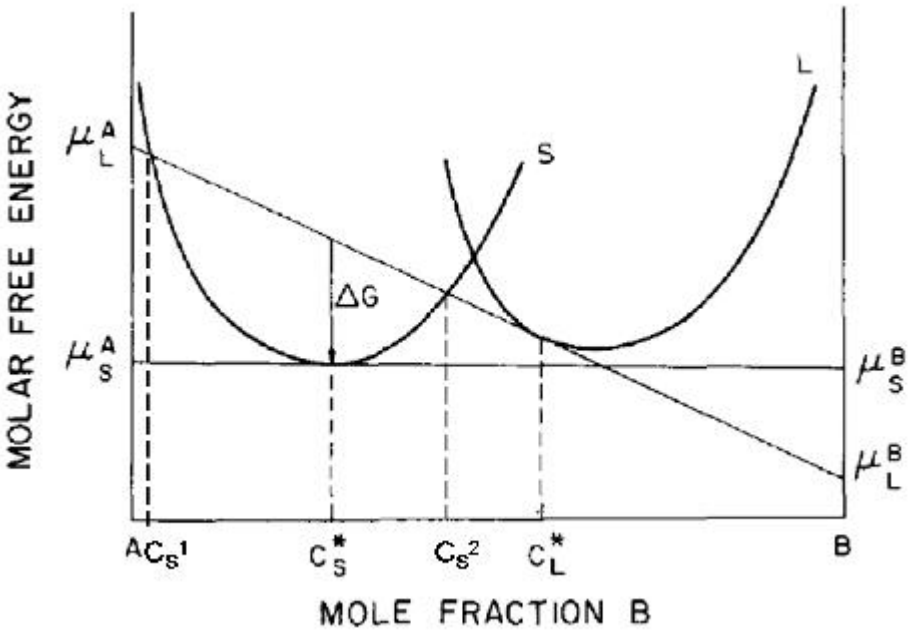

Figure 2.12 When the solid phase with c_S^* grows from the liquid with c_L^*, the molar free energy change is ΔG. The solid phase only with concentrations between c_S^1 and c_S^2 is thermodynamically possible to grow since $\Delta G < 0$.

and T^*. However, for the response function (Eq. 2.13), a specific value of k, which depends on V^* is required for a given solidification condition. The solute trapping phenomenon occurs when the interface velocity is comparable to or larger than the diffusive velocity of solute atom across the solid-liquid interface. At high V^*, there is not enough time to reject solute atoms into the liquid ahead of interface in order to retain local equilibrium. Thus, to determine the specific value of k_V for a given V, the atomic diffusive kinetics of the solute atoms across the interface region needs to be evaluated.

To describe this solute trapping phenomenon at the interface during the rapid growth of alloys, Aziz[2] proposed a simple model which predicts the monotonic variation of k_V from k_e to unity with steady state interface velocities. For dilute solutions, this model is given by

$$k_V = \frac{k_e + V/V_D}{1 + V/V_D} \tag{2.14}$$

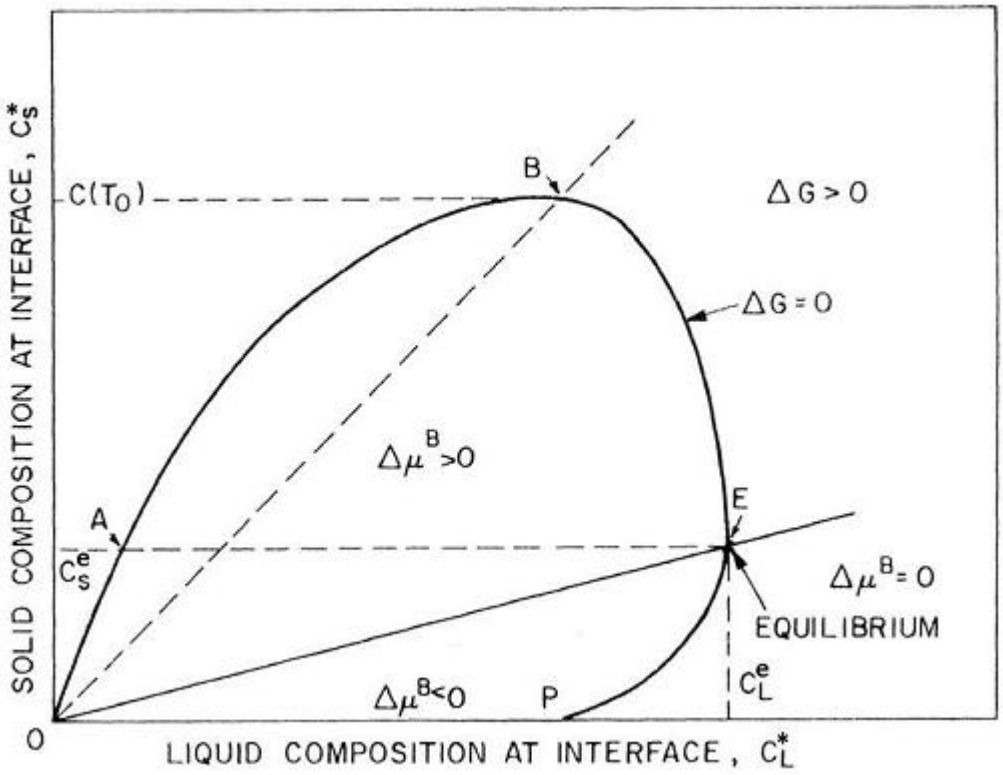

Figure 2.13 The area inside the curve OABEPO is the thermodynamically possible interface composition range in solidification. The point E represents the equilibrium condition. On the line OB, c_S^* and c_L^* are identical and the point B is the composition on the T_0 line.

where V_D is a characteristic velocity of the solute trapping. V_D is the diffusive velocity of a solute atom across the solid-liquid interface, usually represented by the ratio of a solute diffusivity across the interface, D_i, to an interface thickness a_0 which is normally in the nanometer range for metallic systems. Figure 2.15 represents the k_V as a function of V, calculated with Eq. 2.14. The partition coefficient monotonically increases from the equilibrium value, k_e, to unity within a finite velocity range around V_D.

Now the response function for T* (Eq. 2.12) needs to be formulated. Boettinger-Coriell-Sekerka[25, 26] derived a thermodynamically consistent model for T^* as a function of V^* and the interface concentration. In order to relate T^* to V^*, Turnbull's collision-limited growth model[27] was employed. This collision-limited growth model was originally derived for pure

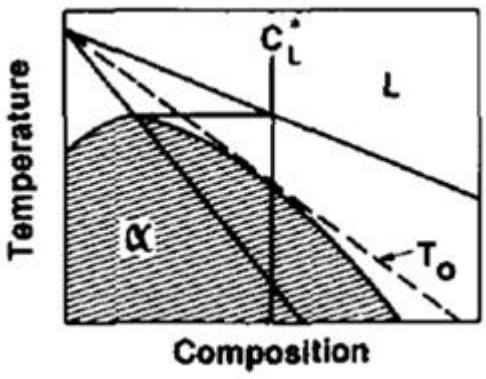

Figure 2.14 The thermodynamically possible c_S^* for a fixed c_L^* (the hatched region) is presented on the phase diagram.

materials and it assumes that during crystal growth the rate of atom attachment on the solid surface is only limited by the collision rate of the atoms on the solid phase. It is expressed as

$$V = fV_0 \left\{ 1 - exp\left(\frac{\Delta G}{RT^*} \right) \right\} \tag{2.15}$$

where f is the fraction of possible sites for the atom attachment on the solid-liquid interface, V_0 is a speed of sound in the liquid metal, ΔG is the molar free energy for solidification, and R is the gas constant. For most closed-packed systems, f is thought to be close to unity and V^* is much lower than V_0. Thus, Eq. 2.15 can be reduced to

$$V = -V_0 \frac{\Delta G}{RT^*} \tag{2.16}$$

ΔG in Eq. 2.16 for alloy solidification corresponds to ΔG in Figure 2.12 and formulated as

$$\Delta G = \left(\mu_S^A - \mu_L^A \right) \left(1 - c_S^* \right) + \left(\mu_S^B - \mu_L^B \right) c_S^* \tag{2.17}$$

For dilute Henrian solutions,[1]

$$\frac{\Delta G}{RT^*} = \left\{ \ln \left[\frac{1 - c_S^*}{1 - c_L^*} \cdot \frac{1 - c_S^e}{1 - c_L^e} \right] \right\} \left(1 - c_S^* \right) + \left\{ \ln \left[\frac{c_S^*}{c_L^*} \cdot \frac{c_S^e}{c_L^e} \right] \right\} c_S^* \tag{2.18}$$

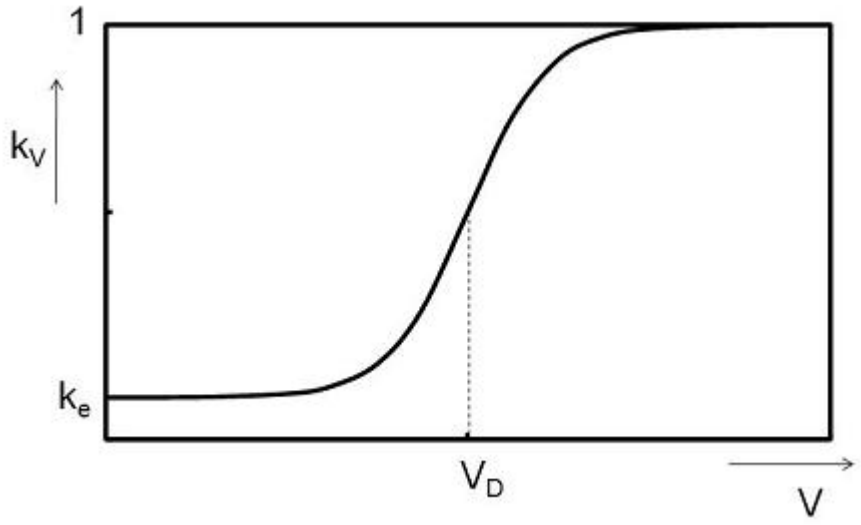

Figure 2.15 Aziz's solute trapping model (Eq. 2.14)

and if straight solidus and liquid lines in the phase diagram are assumed with slopes of m_L^e and m_S^e, respectively,

$$c_L^e = \frac{T^* - T_M}{m_L^e} \tag{2.19a}$$

$$c_S^e = \frac{T^* - T_M}{m_S^e} \tag{2.19b}$$

Since $m_L^e/m_S^e = k_e$, Eq. 2.18 can be further reduced into

$$\frac{\Delta G}{RT^*} = \frac{1-k_e}{m_L^e}\left(T_M + m_L^e c_L^* - T^*\right) + c_L^*\left[k_e - k_V\left(1 - \ln\frac{k_V}{k_e}\right)\right] \tag{2.20}$$

Substitution of Eq. 2.16 into Eq. 2.20 gives

$$T^* = T_M + m_L^e c_L^* + \frac{m_L^e c_L^*}{1-k_e}\left[k_e - k_V\left(1 - \ln\frac{k_V}{k_e}\right)\right] + \frac{m_L^e}{1-k_e}\frac{V^*}{V_0} \tag{2.21}$$

and this Eq. 2.21 could be the response function (Eq. 2.12) for a flat interface. In the last term, the expression $(1-k_e)/m_L^e$ can be replaced by $-L/RT_M^2$ where L is the latent heat per

mole of the solvent element. The interface mobility, μ, can be defined as

$$\mu \equiv \frac{LV_0}{RT_M^2} \tag{2.22}$$

For k_V in the Eq. 2.21, a separate solute trapping model can be used, such as Aziz's solute trapping model, Eq. 2.14. Figure 2.16 shows this response function on a phase diagram for a given c_0. The solid curve depicts non-equilibrium steady state values of T^* and c_L^* as a function of V* for a fixed c_S^* which is equal to c_0. If V^* is low enough to hold $k_V = k_e$ and $V^* << V_0$, c_L^* is always c_0/k_e. The dashed curve represents the case of $\mu = \infty$: the atomic kinetic attachment is ignored, i.e. $V^* << V_0$. As V* increases and solute trapping occurs, c_L^* approaches c_S^* and T* increases. Then with an influence of atomic attachment kinetics at the solid-liquid interface, T* rapidly drops as c_L^* approaches c_S^*.

2.2.3 Critical experiments and models of rapid solidification

The solute trapping model, Eq. 2.14, has been tested by the pulsed laser melting (PLM) experimental technique and it has been experimentally shown that the partition coefficient actually increase with growth velocities. The sample alloys were prepared by implanting the solute atom into the pure metal. The solute concentration profiles were measured before and after the pulsed laser melting. The time-resolved interface velocity and temperature were measured by exploiting the electrical conductivity and resistance during melting and solidification. The velocity dependent partition coefficient can be determined by comparing the measured solute concentration profile with the profile calculated using one-dimensional time-dependent diffusion calculation results that neglect solute diffusivity in the solid phase.

Several dilute Si- and Al- binary alloys have been used for these measurements[28, 29, 30, 31, 32]. The experimental data was reasonably good agreement with the solute trapping model as shown in Figure 2.17[28]. Since the parameter V_D in Aziz's solute trapping model is difficult to be directly measured experimentally, it is obtained by being considered as an adjustable parameter for best fitting in comparison of these experimentally measured $k_V\,(V)$ with Aziz's solute model (Eq. 2.14). V_D values determined in this way for various alloy systems are listed

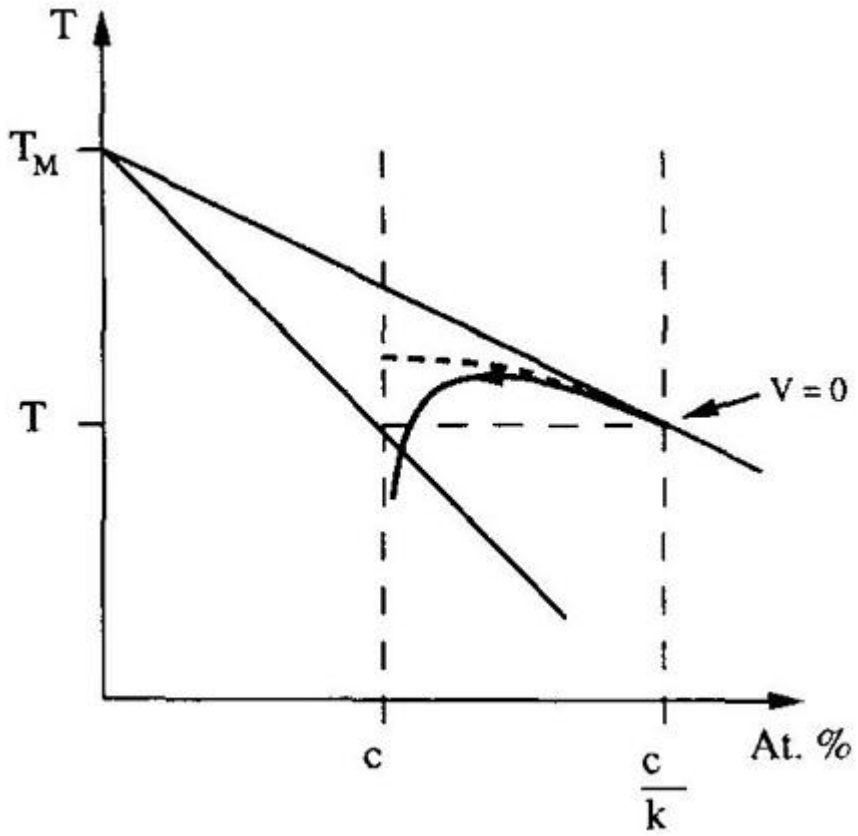

Figure 2.16 Interface temperature and interface concentration in the liquid with increasing V* for a given c_0 (the solid curve). The dashed curve shows the case of $\mu = \infty$.

in Table 2.1.

However, these experimentally obtained k_V data had been obtained mainly in relatively low $V\,(\leq V_D)$ regime. Later, Kittl *et al.*[33, 36] has measured $k_V\,(V)$ for higher V regime $(V > V_D)$ with non-dilute Al-As binary alloys. Their measured $k_V\,(V)$ data shows generally good consistency with Aziz's solute trapping model. However, there was a slight discrepancy for a very high V in both Al-4.5 at.%As and Al-9 at.%As (Figure 2.18). The measured $k_V\,(V)$ for both alloys are rather larger than predicted $k_V\,(V)$ curves at around 2 m/s when the V_D obtained by best fitting of Aziz's solute trapping model (Eq. 2.14) was 0.37 m/s[36]. The authors argued that the data which showed the discrepancy have uncertainty in measurement of c_L^* in such a high velocity regime.

Table 2.1 Measured diffusive speeds across the solid-liquid interface, V_D, using the pulsed laser melting (PLM) technique

Materials	V_D (m/s)	References
Si-As	0.46	[33]
Si-Ge	2.03	[34]
Si-Bi	32	[28]
Si-Sn	17	[30]
Si-Ge	22	[31]
Si-In	57	[31]
Si-Sb	0.64	[31]
Al-Sn	36	[31]
Al-In	38	[31]
Al-Ge	6.1	[31]
Al-Cu	6.7	[31]
Ni-Zr	26	[35]

Besides the partition coefficient, the rapid dendritic solidification kinetics are experimentally measured by Herlach *et al.*[37] using an electromagnetic levitation device for containerless rapid solidification of pure metal and alloys to measure the interface velocity as a function of the given undercooling. A melt drop suspended in levitation coil was undercooled to a desired temperature, and solidification was triggered using a solid needle. This technique allows controlling the initial melt undercooling and the initial nucleation site, and direct observation of solidification process. By monitoring the temperature change by recalescence during crystallization at two different positions, the rate of the interface advancement during growth can be derived. Using this technique, the dendrite growth velocity as a function of undercooling has been measured for many pure materials and alloys: pure Ni and $Cu_{70}Ni_{30}$ alloy[38], pure Fe[39], dilute Ni-B[40], Ni-C alloys[41], Fe-Ni[42], Ni-Si[43], FeSi and CoSi[44], Ni-Al[45], Fe-Ni-Cr[46] alloys.

In Willnecker *et al.*'s measurements[38], the velocity-undercooling relationships for pure Ni and Ni-Cu alloy follow a power-law up to a critical undercooling, ΔT^*. For undercoolings higher than ΔT^*, V increases linearly for the increasing undercooling (Figure 2.19). The experimental evidence for Ni-B alloys by Eckler *et al.*[40] showed that this critical undercooling, ΔT^*, strongly depends on the alloy composition; higher solute concentration results in higher

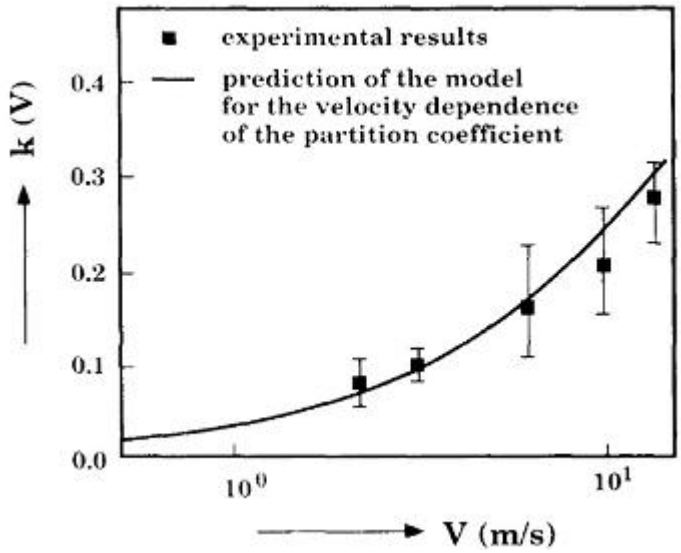

Figure 2.17 Dependence of the partition coefficient on the interface velocity: squares indicate the experimentally measured data from Bi-doped Si, and the solid curve is the prediction of Aziz's solute trapping model with V_D=32 m/sec.[28]

ΔT^*. In addition, several experimental data[47, 48] show a plateau may appear at a velocity for lower than ΔT^*.

2.2.4 Rapid dendritic growth theory

To describe the rapid dendritic growth dynamics, the interface curvature effect needs to be considered in addition to the solutal redistribution effect and kinetic effect in the rapid planar front dynamics (Eq. 2.21).

The first dendrite growth theory was introduced by Lipton-Glicksman-Kurz (LGK)[49], predicting the growth rate of an isolated dendrite which is growing into the undercooled melt as a function of undercooling and alloy composition, assuming the local equilibrium at the solid-liquid interface and the low solutal and thermal Peclet numbers. Because of these assumptions, this LGK theory can be applied only to a non-rapid growth where the solute trapping does not occur. This LGK theory includes the effects of solute redistribution, latent heat release, and interface curvature at the tip, and uses the marginal stability criterion to predict the growth

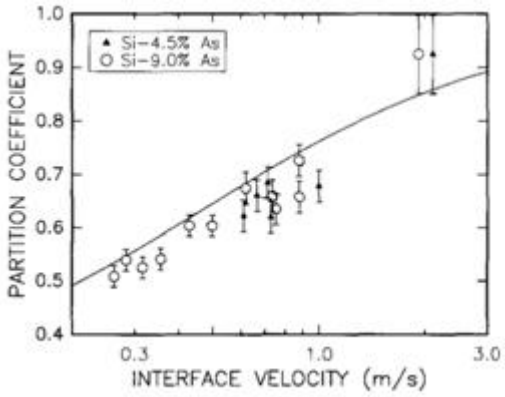

Figure 2.18 The measured partition coefficient on the interface velocity for Al-4.5 and 9 at.%As and model predictions. Aziz's solute trapping model for dilute solution (Eq. 2.14) is fitted with V_D=0.46 m/sec[33]

rate and the tip radius. In this theory, the total undercooling, ΔT, is composed of three parts: the thermal undercooling, ΔT_t, the solute undercooling, ΔT_c, and the curvature undercooling, ΔT_r,

$$\Delta T = \Delta T_t + \Delta T_c + \Delta T_r \tag{2.23}$$

These undercoolings are described in Figure 2.20 and Figure 2.21. When a steady state isolated alloy dendrite grows into the melt with temperature T_∞, solute pile-up in front of the tip increase the melting temperature with the distance from the tip. Latent heat rejected from the solid increase the tip temperature from T_∞. Due to the capillary force at the tip, the curvature undercooling exists.

The undercoolings are given for dilute alloys and linear solidus and liquidus lines by

$$\Delta T = \Delta T_L^e \left(c_0\right) - T_\infty \tag{2.24}$$

$$\Delta T_t = Iv \left(P_t\right) L/C_P \tag{2.25}$$

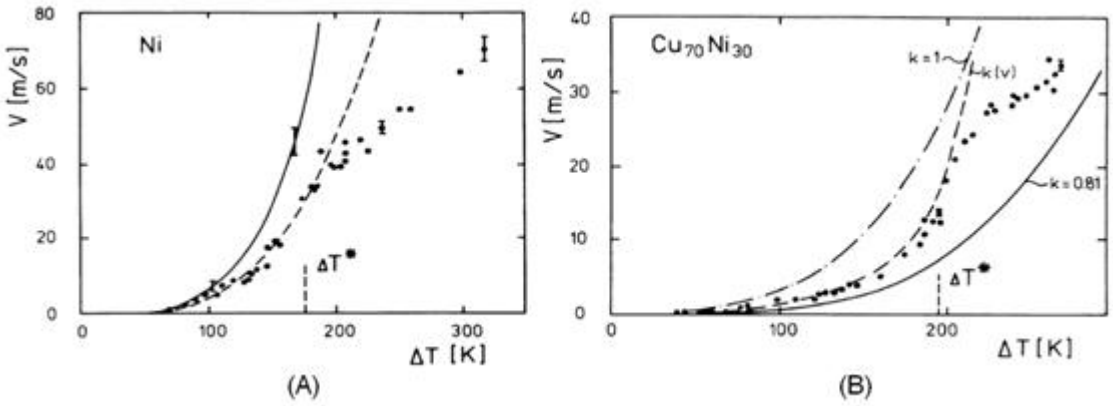

Figure 2.19 Measured solidification velocity as a function of melt undercooling for (A) pure Ni and (B) $Ni_{70}Cu_{30}$ binary alloy. For both materials, the growth mode was changed at a critical undercooling ΔT^*. The solid curve is a theoretical prediction with LKT model[50]. With considering the kinetic undercooling, the dashed curve was fitted to the measured data with $\mu = 1.6$ m/sK. Using the same value of μ, the experimented data of $Ni_{70}Cu_{30}$ was fitted by the BCT model with Aziz's solute trapping model[51]. For comparison, the prediction with k=1 (partitionless growth) and k=0.81 (the equilibrium partition coefficient) are also shown.[38]

$$\Delta T_c = k_e \Delta T_0 \left\{ \frac{Iv\left(P_c\right)}{1-\left(1-k_e\right) Iv\left(P_c\right)} \right\} \tag{2.26}$$

$$\Delta T_r = 2T_M \Gamma / R^* \tag{2.27}$$

where $T_L^e\left(c_0\right)$ is the equilibrium liquidus temperature for the nominal concentration of the alloy, c_0, and T_∞ is the liquid melt bath temperature. L is the latent heat per unit volume, C_P is the heat capacity per unit volume, and ΔT_0 is the freezing range of the alloy for c_0, $m_L c_0\left(k_e-1\right)/k_e$ when the liquidus line is straight (i.e. m_L is constant). Ivantsov function, Iv(P), is given by

$$Iv\left(P\right) = Pe^P E_1\left(P\right) \tag{2.28}$$

where the function $E_1\left(P\right)$ is the first exponential integral function. The parameters P_t and

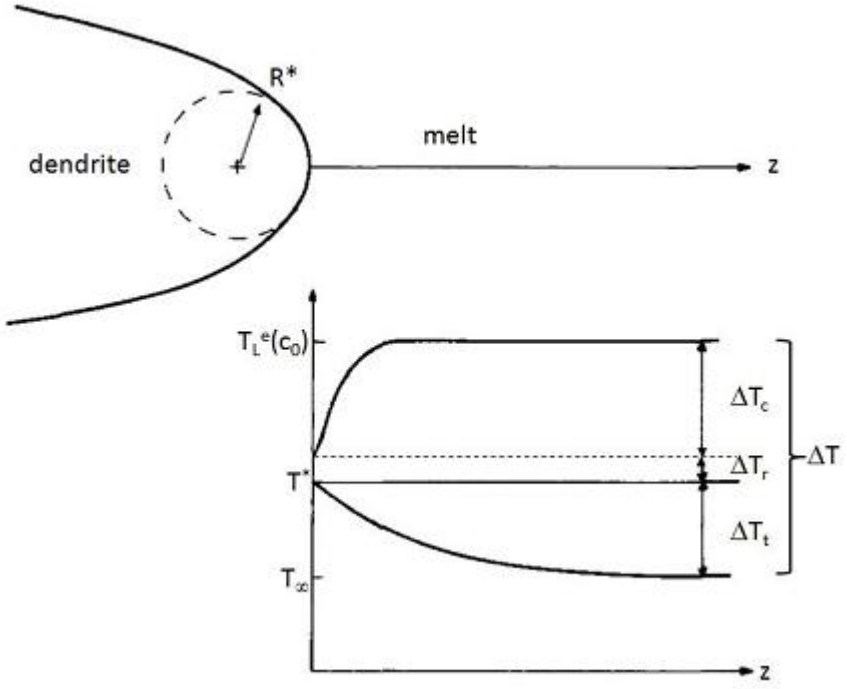

Figure 2.20 Melt temperature and the liquidus temperature ahead of a dendrite tip which is growing into an undercooled melt[49]

P_c are thermal and solute Peclet numbers, respectively, and given by $VR/2\alpha$ and $VR/2D_L$, respectively. R* is a dendrite tip radius, α is a liquid thermal diffusivity, and D_L is a solute diffusivity in the melt.

For a given ΔT, specific values of R* and V cannot be uniquely specified by the Eq. 2.24-2.28 which only give the relation between ΔT and the product of V and R*. To specify the value of R* under a given solidification condition, the LGK model employed the marginal stability criterion by Langer and Muller-Krumbhaar[52]. According to this stability criterion, the observed R* is equal to the shortest wavelength, λ_i, of a perturbation which can grow under the local growth condition at the tip. This wavelength is given by the minimum unstable wavelength in the result of the linear stability theory for planar interface at low velocity (Figure 2.7). With this marginal stability criterion, all the parameters at the dendrite tip could be successfully obtained.

However, the marginal stability criterion in LGK model is for small k_e and small P_c. Thus,

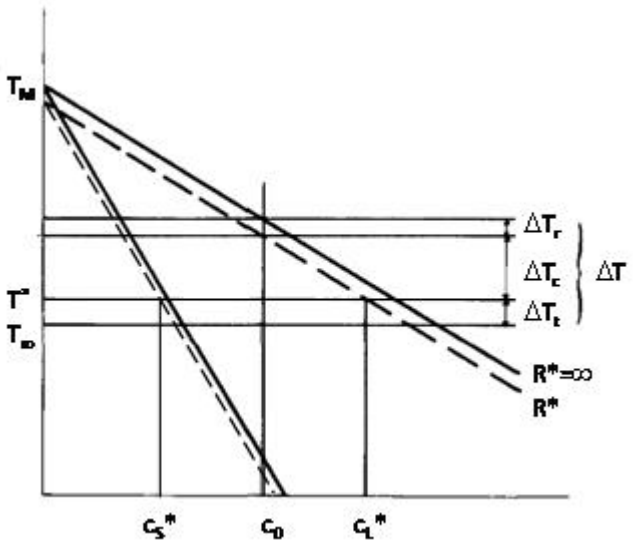

Figure 2.21 A schematic binary phase diagram, describing tip temperature T* and tip concentration c_L^* and c_S^* of a steady state dendrite growing into the undercooled melt with T_∞[49].

Boettinger-Coriell[26] obtained more rigorous expression for minimum wavelength which can be employed even for large P_c (but small P_t) using Mullins-Sekerka's stability criterion (MS)[10], and later Lipton-Kurz-Trivedi (LKT)[50] extended it for large P_c and large P_t. The wavelength obtained by LKT model is

$$\lambda_i = R^* = \left\{ \frac{T_M \Gamma/\sigma^*}{(L/C_P)\, P_t \xi_t + \frac{2m_L^e c_0 (k_e - 1)}{1-(1-k_e) Iv(P_c)} \xi_c} \right\}^{1/2} \tag{2.29}$$

where $\xi_t = 1 - \frac{1}{\sqrt{1+1/(\sigma^* P_t^2)}}$ and $\xi_c = 1 + \frac{2k_e}{1-2k_e-\sqrt{1+1/(\sigma^* P_c^2)}}$. The parameter σ^* is $1/4\pi^2$. With Eq. 2.23-2.29, V* and R* can be predicted with a given melt undercooling, ΔT.

Boettinger, Coriell, and Trivedi (BCT)[51] modified the previous dendritic growth theory by considering the thermodynamic driving force of solidification process, Eq. 2.17[1], and Turnbull's linear kinetic model[27], Eq. 2.16. They also applied interface solute trapping model[2, 53] (Eq. 2.14) and the marginal stability criterion from LKT model (Eq. 2.29) to predict the tip radius. In this analysis,

$$\Delta T = \Delta T_t + \Delta T_c + \Delta T_r + \Delta T_k \tag{2.30}$$

where ΔT_k is the kinetic undercooling. For ΔT, ΔT_t, and ΔT_r, Eq. 2.24, Eq. 2.25, and Eq. 2.27 can be applied, respectively. For R*, the marginal stability criterion for high P_c and P_t from LKT model (Eq. 2.27) was used, but k_e was replaced by k_V to describe the solute trapping phenomenon. ΔT_c and ΔT_k are same as the third and fourth terms in Eq. 2.21, respectively, and can be rewritten as

$$\Delta T_c = m_L^e c_0 \left[1 - \frac{m_L^v/m_L^e}{1-(1-k_V)\,Iv\,(P_c)}\right] \tag{2.31}$$

$$\Delta T_k = V^*/\mu \tag{2.32}$$

where m_L^v is the kinetic liquidus slope, which is

$$m_L^v = m_L^e \left\{\frac{1-k_V-k_V\ln(k_V/k_e)}{1-k_e}\right\} \tag{2.33}$$

for dilute alloys, and the interface mobility, $\mu = LV_0/\left(RT_M^2\right)$. According to this solution, when the solidification rate becomes sufficiently high, the steady state interface temperature might be sensitively influenced by the degree of solute trapping and the interface attachment kinetics represented by ΔT_k, both of which are varying with the interface velocity, V*.

The broken curve in the Figure 2.19 (B) shows the prediction from this BCT model. μ for ΔT_k and V_D for k_V are treated as adjustable parameters to best fit the theoretical model on the experimental results. This gives a good agreement with the experimental data below ΔT^* as shown in Figure 2.19. But, the linear growth mode above ΔT^* could not be predicted by the BCT model.

2.2.5 Kinetic phase diagram and steady state interface temperature during rapid solidification

The interface response function for a planar growth front (Eq. 2.21) can be used to plot non-equilibrium phase diagrams. At a given V*, the Eq. 2.21 gives the relationships of the interface temperature versus the interface compositions, i.e. non-equilibrium solidus and liquidus lines

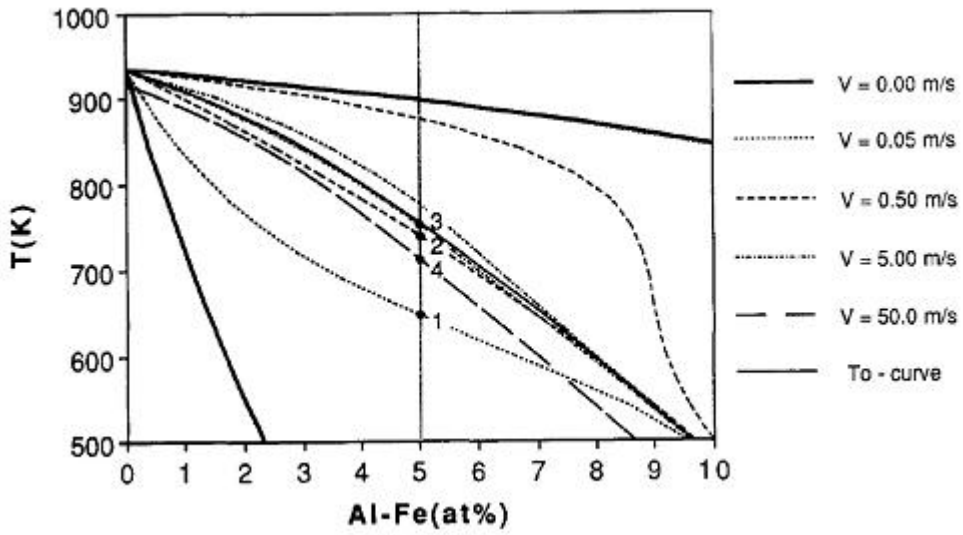

Figure 2.22 Kinetic phase-diagram of Al-Fe binary alloys with different growth rates calculated by Carrard *et al.*[54]. The points 1,2,3, and 4 indicate the steady state planar front temperature for an Al-5 at.%Fe alloy.

for a dilute binary alloy with straight equilibrium solidus and liquidus lines. These kinetic phase diagrams depend on the parameter, μ and V_D. Figure 2.22 is one example of kinetic phase diagrams calculated by Carrard *et al.*[54] for Al-Fe binary alloys. Instead of constant m_L^e and k_e, concentration-dependent m_L^e and temperature-dependent k_e are used for this result. This result shows a typical variation of the steady state interface temperature of a planar front with V*. For Al-5 at.% Fe alloy, the steady state T* with the local equilibrium condition is much lower than 500 K. When V* increases and solute trapping at the interface occurs, the slope of the solidus curve increases and that of the liquidus curve decreases with V*. Thus, the solidus and liquidus curves approach each other and the steady state T* of the planar front increases (points 1,2, and 3 in Figure 2.22). If μ is large enough that the ΔT_k term can be ignored, those two curves would eventually converge on the T_0-curve. For general metallic systems, the effect of the kinetic undercooling becomes important at very high velocities. Then the whole solidus and liquidus curves may drop toward lower temperatures in the phase diagram, depending on V* (point 4 in Figure 2.22).

Based on kinetic phase diagrams for a given alloy composition, c_0, the liquidus and solidus

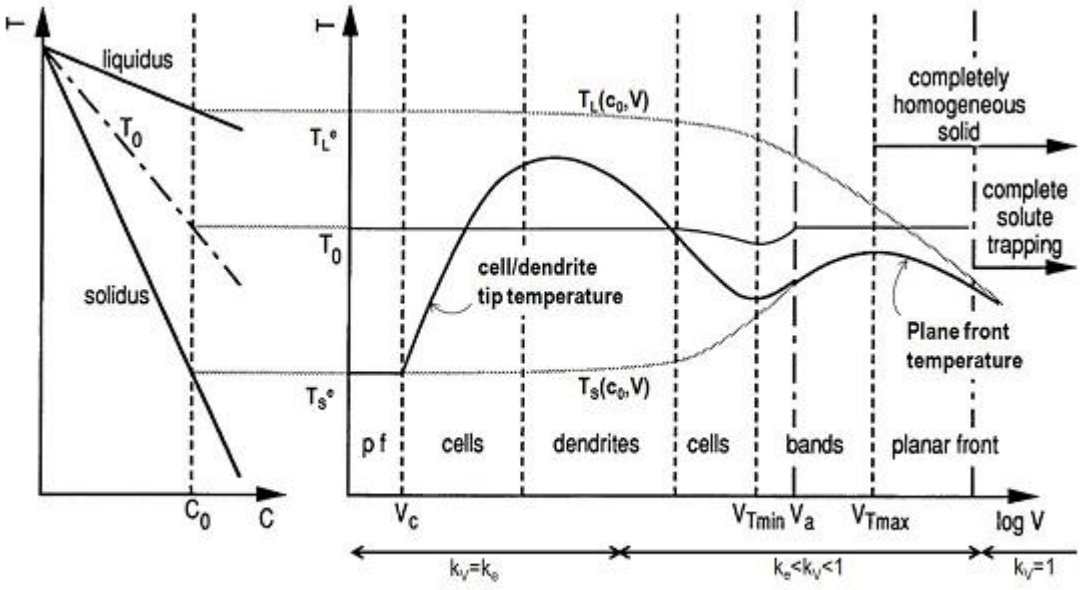

Figure 2.23 Schematic solidus and liquidus temperatures, $T_S(c_0, V)$ and $T_L(c_0, V)$, respectively, for a given alloy composition, c_0, with different growth velocities. The steady state planar front temperature is equal to $T_S(c_0, V)$, and dendrite tip temperatures can be obtained by the theories which are described in the previous section

temperatures, $T_L\,(c_0)$ and $T_S\,(c_0)$, could be represented in terms of V as shown in Figure 2.23. With low or moderate V* where the local equilibrium condition can be retained, T_L and T_S remain constant and are same as the equilibrium values. As V* increases, T_S and T_L approach T_0 first due to the solute trapping phenomenon, and then both T_L and T_S decrease due to the influence of ΔT_k. Decrease of T_S might happen when the effect of the kinetic undercooling become significant enough to compensate the undercooling decrease due to the solute trapping, and T_S may have a maximum. While both T_S and T_L are decreasing with V*, the values approach each other with V* until k_V=1.

For a steady state planar-front growth, c_S^* is the same as c_0 and T* is equal to $T_S(c_0, V)$. If planar-front growth were to happen for all velocities, the variation of T* with V* would follow the T_S curve in Figure 2.23. In metallic alloy systems, the thermal and solutal fluctuations

in front of the interface induce the interface instability, the planar front breaks down, and dendrite or cell structure develops under a general solidification condition. Theories for each of these events with various V* have been extensively developed as described in the previous section, whereas the mechanism of rapid solidification of alloys has not been fully clarified yet.

2.2.6 Modified solute trapping and dendritic growth models

Galenko and Sobolev[3, 55] expended Aziz's solute trapping model, considering the relaxation time of non-equilibrium chemical diffusion process in the bulk liquid phase by introducing a parameter, V_{DL}, which is defined as a maximum speed for the front of the solute diffusion propagation[55]. For dilute solutions, the model was formulated as

$$k_V = \frac{k_e\left(1 - V^2/V_{DL}^2\right) + V/V_D}{1 - V^2/V_{DL}^2 + V/V_D} \quad (V < V_{DL}) \tag{2.34}$$

$$k_V = 1 \quad (V \geq V_{DL}) \tag{2.35}$$

Figure 2.24 shows the difference between Galenko's model and Aziz's model with the same V_D. While k_V can converge onto the value of unity only at infinite velocity with Aziz's solute trapping model, Galenko's model allows for a description of the complete partitionless (k_V=1) interface at above a finite velocity (V_{DL}).

Figure 2.25 shows the comparisons of this Galenko's model with Aziz's solute trapping model fitted to the experimentally measured k_V (squares and circles) by Kittl *et al.*[33, 36]. While Aziz's solute trapping model (dashed curves) fits well only with moderate solidification velocities, Galenko's model (solid curves) provided better agreement with this experiment even for very high velocity ($V > V_D$) where k_V becomes close to 1.

However, due to the lack of experimental data for such an extremely high velocity range, these solute trapping models have not been thoroughly validated. More exact experimental data is required especially for the high interface velocity where k_V is approaching to 1.

For the prediction of steady state rapid dendritic growth, Galenko and Danilov[56, 57] extended the previous models by considering the non-equilibrium solute diffusion in the melt with Galenko and Sobolev's solute trapping model instead of Aziz's model. By utilizing another

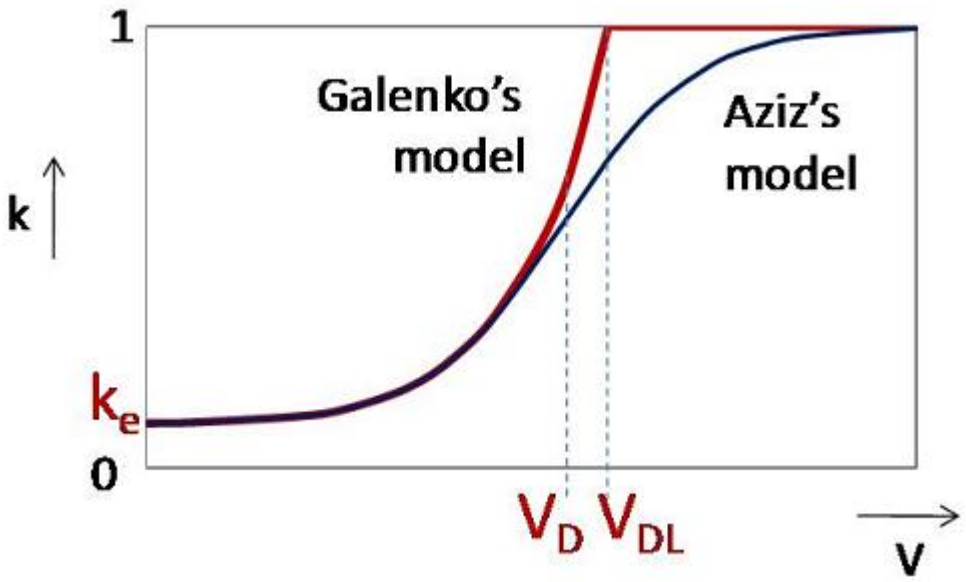

Figure 2.24 The variations of the partition coefficient with growth velocity from Aziz's solute trapping model and Galenko's solute trapping model

adjustable parameter, V_{DL}, the model predictions for a whole range of undercoolings agree reasonably well with experimental data even at an undercooling higher than $\Delta T*$. Wang *et al.*[58] further extended this model considering the non-linear liquidus and solidus lines. By fitting with several adjustable parameters, the model calculation is in reasonably good agreement with experimental data as shown in Figure 2.26.

According to these analytical models, dendritic growth should be controlled by purely solutal diffusion field ahead of the dendrite tip at low undercoolings. This undercooling range corresponds to ΔT <180 K in the Figure 2.26. During this solutal-controlled dendritic growth, V* increases with ΔT, and at the same time solute trapping may start. In this relatively low-rate growth, thermal diffusion length is much longer than the tip radius, and thermal diffusion might have almost no influence on the growth. As V* increases further, thermal diffusion length becomes shorter, and both solutal and thermal fields control the dendritic growth. The onset velocity of the solutal/thermal dendrite corresponds to the solutal absolute stability velocity, V_{AS}, obtained by the stability analysis[58]. In the analytical modeling in

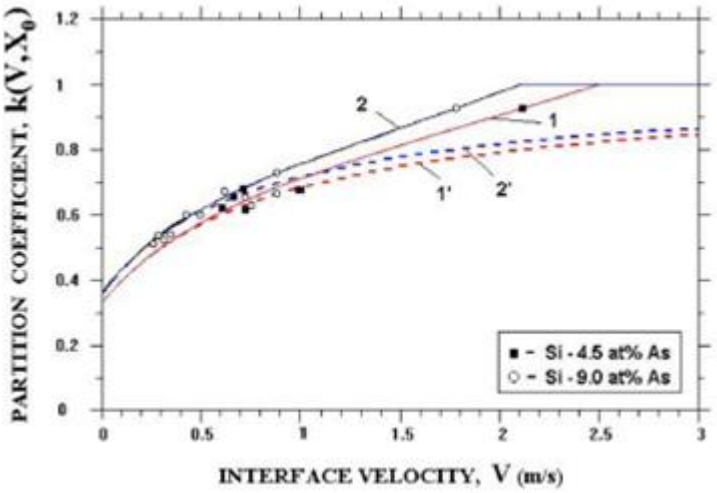

Figure 2.25 Partition coefficient versus interface velocity from Galenko's solute trapping model (curves 1 and 2) fitted to the Kittl *et al.*'s experimental data which is shown in Figure 2.18. V_D=0.8 m/s, V_{DL}=2.5 m/s for curve 1 and 2.1 m/s for curve 2 are used. The curves 1' and 2' are given by Eq. 2.34 with $V_{DL} = \infty$ which is identical with Aziz's solute trapping model[55].

Figure 2.26, V_{AS} corresponds to the undercooling around ΔT =180 K where the $V - \Delta T$ behavior starts to change. For $\Delta T > \Delta T(V_{AS})$, the solute trapping phenomenon results in the gradual transition from solute and thermal dendritic growth to purely thermal dendritic growth. According to Galenko's solute trapping model, the degree of solute partitioning at the interface abruptly decreases over a finite velocity range, and complete solute trapping occurs when $V^* \geq V_{DL}$. When the complete solute trapping takes place, the dendritic growth would be controlled by pure thermal diffusion. According to Galenko and Danilov, this transition causes the growth mechanism change from power law to linear law at a critical undercooling, ΔT^*, and this ΔT^* is the undercooling where $V = V_{DL}$. For $\Delta T > \Delta T(V_{DL})$, solute pile-up in front of dendrites vanishes, the concentration of solid phase behind the tip becomes same as the nominal concentration of the alloy system, and the dendritic growth should be purely thermal-controlled.

To describe the phenomenon that happens at and near the interface, these steady state dendrite growth models utilize many separate analytic models: collision-limited growth model,

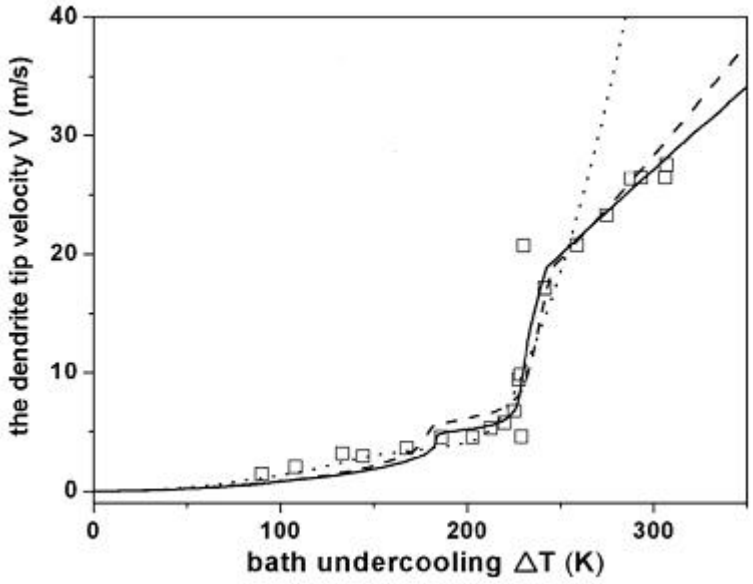

Figure 2.26 Dendritic growth velocity versus bath undercooling. The squares are experimental data of Ni-0.7 at.% B alloys by Eckler *et al.*[40, 59], the dotted curve is the prediction of the BCT model, the broken curve is that of Galenko's model[56], and the solid curve is Wang's prediction.

solute trapping model, marginal stability criterion (or microscopic solvability theory), and solute drag model. The values of many physical parameters for these separate models have been approximated or obtained by fitting the model into experimental data since those are hard to be obtained experimentally are considered as adjustable fitting parameters.

Despite these attempts to describe rapid growth kinetics with analytical models, the fundamental and comprehensive mechanism regarding the rapid solidification dynamics has not been clearly enlightened yet. So far, no conclusive answer has been given to the $V^* - \Delta T$ behavior: the behavior above ΔT^* and the physical interpretation of ΔT^* as well as the quantification of the value itself. This question still remains far from fully answered even though there have been several accounts and conjectures that point to the reason of the growth mode change at ΔT^* such as; residual oxygen[47], effects of the anisotropy of kinetic interfacial mobility and change of the solute diffusion field due to the dramatic change of morphology such as dendrite to cell (or seaweed structure) transition and side branch development[60], termination

of the steady state dendritic growth[60, 61, 62], and transition from solutal-controlled growth to thermal-controlled growth[63, 64] which has been described above. Although the modeling results could be in good agreement with experimental data, those are limited to the description of steady state dendritic growth. These analytic steady state dendrite models ignored the various morphological changes with growth dynamics. In order to investigate rapid growth dynamics with morphology evolution, a numerical approach is more appropriate than analytical modeling with combination of separate models for each process.

2.3 Banded Structure Formation

2.3.1 Early interesting observation of banded structure in rapid solidification

In rapid alloy solidification experiments, Sastry-Suryanarayana[65] first showed a periodic band structure as an independent phenomenon in their rapid quenching experiments of Al-Pd droplets. This band structure is characterized by regular succession of alternating light and dark bands parallel to the solidification front (Figure 2.27). It has been shown that the formation of this structure is a common phenomenon, in laser- or electron-beam melting, melt-spinning or splat quenching experiments with various alloy systems:

Dendritic alloys: Ag-1˜65% Cu[66, 67, 68, 69, 70, 71], Al-20˜33%Cu[72], Al-0.5˜4%Fe[73], Al-20%Pd[65], Al-6%Zr[74]

Eutectic alloys: Ag-28%Cu[66], Al-33%Cu[75, 76]

Formation of this banded structure occurs at velocities near the limit of the absolute stability: the absolute stability velocity can be calculated from Mullins-Sekerka's stability analysis of planar front and the velocity, a perturbation with any wavelength tends to diminish, i.e. a planar front is the most stable. In the dark bands, cellular, dendritic or eutectic structures have been seen, depending on the nominal composition of the alloy. The light band is segregation free and has uniform composition, so that it has been presumed that the planar growth results in these light bands.

From the series of electron beam solidifications of Ag-Cu binary alloys with various beam scanning velocities and alloy compositions, the microstructure map, Figure 2.28, was estab-

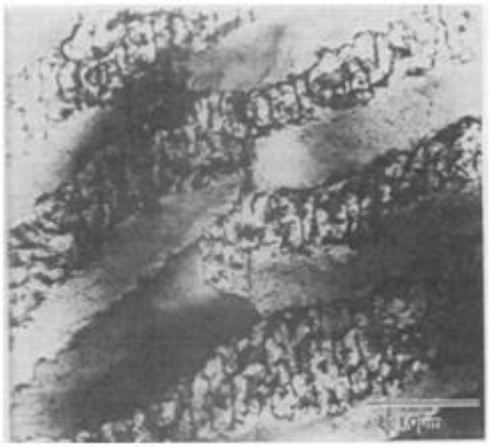

Figure 2.27 Typical banded structure observed in electron beam solidification of Ag-Cu alloys. The electron beam scan velocity is 17 cm/sec.[66]

lished [66]. The band structure was observed with the velocities between those for cell/dendrites and for microsegregation-free structures. Band structure did not appear in dilute alloys. The velocities for the transitions from cells/dendrites to bands, and from bands to microsegregation-free structures decrease with c_0.

2.3.2 Interface stability analysis for banded structure formation

Banded structure formation is an interesting phenomenon since it cannot be explained by the classical Mullins-Sekerka's linear absolute stability analysis[10] for planar interface. The modified linear absolute stability analysis accounting for local non-equilibrium effect, such as solute trapping[77, 78], may be related with the band structure formation. The result of the modified linear absolute stability analysis for planar interface showed that the velocity of absolute stability limit, V_{AS}, is higher than that from the classical Mullins-Sekerka's stability analysis, and at velocities slightly less than V_{AS}, there is an oscillatory instability with time for rather long wavelengths.

Coriell-Sekerka[77] modified the classical Mullins-Sekerka's linear stability theory[10] by considering the velocity-dependent chemical partition coefficient for the first time. In the result of this analysis, it was shown that at high velocities there exists oscillatory instability

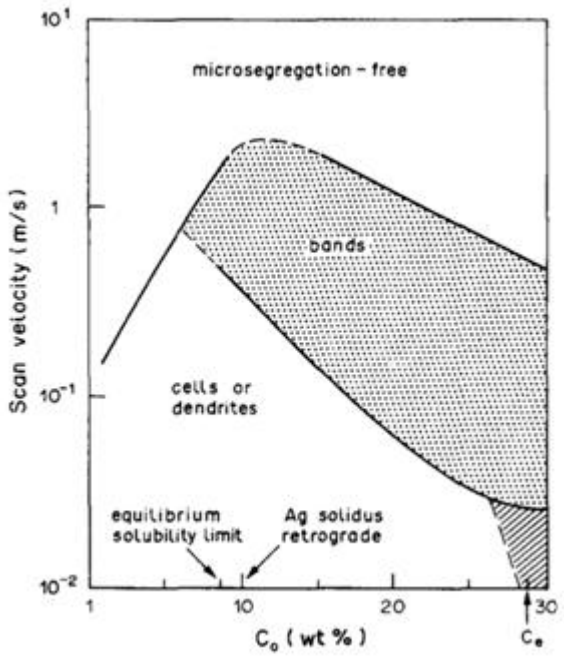

Figure 2.28 Experimentally determined microstructure selection map for Ag-Cu alloys by electron beam solidification[66]

for relatively long wavelength perturbations, in addition to the instability predicted by Mullins-Sekerka's theory. This modified stability analysis suggested that the instability may occur with so called "solute pump mechanism." For V* with large $\partial k_V/\partial V$, the local interface velocities along the perturbed solid-liquid interface is varying, and so as k_V. Thus, there exists variation of solute rejection rate along the interface. For any perturbation, the local interface velocity and k_V reach maxima at the peak of the perturbation and thus the least amount of solute would be rejected at the peak. This makes lateral solute segregation which does not required lateral solute diffusion. This is the suggested "solute pump mechanism" which explains how the relatively long wavelength perturbation can be unstable even at high velocities. Since the wavelength is quite long, capillarity is not very effective in stabilizing the plane front. This is in contrast with the situation in the classical Mullins-Sekerka's stability model; solute diffusion drives the lateral segregation, only a short wavelength of perturbation which can produce lateral segregation would exist at high velocities because of decreasing solute diffusive time, and this short wave is strongly stabilized by capillarity. Such instability of long wavelength

perturbations may exist at even higher interface velocities than that of the absolute stability limit by Mullins-Sekerka's theory. This is because capillarity does not strongly affect the instability of this long wavelength perturbation, whereas in the classical Mullins-Sekerka's stability analysis the plane front stabilizes by the strong capillarity effect. The result of the modified linear stability analysis critically depends on the parameters, μ and V_D. For V* with small derivative, $\partial k_V/\partial V$, classical Mullins-Sekerka absolute stability theory may be valid with direct substitution of k_V for k_e.

This instability in the solute pump mechanism has oscillatory characteristics. Since solute is least rejected at the peak of a perturbation, the decreased local concentration gradient makes the local velocity at the peak of the perturbation slower. With a decreasing peak velocity, k_V decreases at the peak. Then more amount of solute is rejected from solid and the local concentration gradient increases again. Subsequently, the local interface velocity increases. This cycle repeats.

This long wavelength oscillatory instability had been considered as a possible mechanism of banded structure formation[66, 79]. However, even if the diffusionless lateral solute segregation occurs, the degree of the segregation is not big enough to explain the high solute concentration of precipitations in dark bands. Furthermore, this lateral solute segregation cannot directly explain the evolution of alternating morphologies in banded structures.

Merchant-Davis[78] modified the analysis of Coriell-Sekerka[77]. Using Aziz's solute trapping model for dilute solutions[2] and incorporating the kinetic undercooling at the interface, the Merchant-Davis's model allows velocity-dependent k_V and T* in a thermodynamically consistent way. Based on the fixed temperature gradient condition, latent heat release is ignored. In this analysis, new oscillatory instability for the infinite wavelength, i.e. planar front, has been identified. Above a certain critical growth velocity, zero-wave number of perturbation becomes most unstable. This is schematically illustrated in Figure 2.29 and Figure 2.30. Figure 2.29 represents a spectrum of amplification rates of perturbations for a given V at which plane front oscillatory instability occurs. If a perturbation has a positive amplification rate, the plane front tends to be unstable and the perturbation with corresponding wavelength would

grow. In addition to the instability of perturbations with a finite range of wavelengths predicted in the Mullis-Sekerka's model (solid curve), it has been shown that there exists another instability with very high wavelengths (dashed curve) and the most unstable perturbation is one with infinite wavelength. Figure 2.30 shows conditions where amplification rate becomes zero (neutral stability) for any wavelength in $V - c_0$ space. The solid curve in a low velocity range represents the neutral stability condition for non-oscillatory instability, and the dashed curve in a high velocity range shows that for the oscillatory planar front instability identified by Merchant-Davis. The interface mobility,μ, affects the stabilization of this oscillatory instability as well as $\partial k_V/\partial V$. With a k_V close to unity or smaller value of μ, planar front tends to stabilize. A smaller μ leads to a shifted dashed curve to the higher c_0 range in the Figure 2.30. It has been proposed that this instability of planar front should trigger the oscillatory interface dynamics which yields banded structures[80, 81]. Later, Huntley-Davis[82] extended the linear stability analysis for better understanding of the role of thermal diffusion in banding phenomena.

2.3.3 Phenomenological analysis and schematics of banded structure formation

The linear stability analysis has been shown that planar front has oscillatory instability at high growth rates and this instability might trigger the interface dynamics for banded structure formation. This, however, cannot explain the interface dynamics itself which could give rise to banded structures. Thus Boettinger *et al.*[66], Gremaud *et al.*[73], and Carrard *et al.*[54] have proposed a phenomenological interface dynamics model to elaborate the time-periodic structure change. The Figure 2.31 schematically shows the steady state velocity-dependent interface temperature of planar and dendritic growth for high velocity range. For a directional growth condition with a constant temperature gradient, G, a given pulling velocity, V_P, lower than V_1 gives dendritic structures, and planar growth occurs with V_P higher than V_3. According to Carrard *et al.*'s explanation[54], if V_P is between V_1 and V_3, the steady state cannot be achieved because planar front is unstable under a directional growth condition with a pulling velocity in the range of $dT_S/dV > 0$; the driving force for the solidification decreases

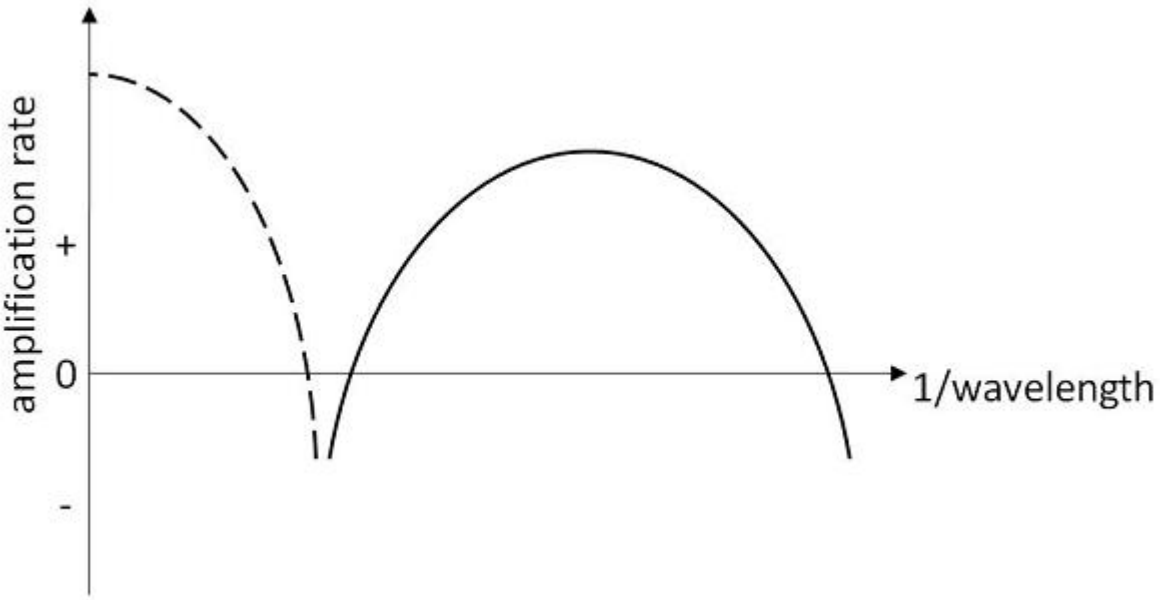

Figure 2.29 A schematic of amplification rate of perturbations on a planar front with wavelengths. The solid curve and the dashed curve represent the non-oscillatory and oscillatory instabilities, respectively. For a certain growth condition, a planar front (the infinite wavelength) with the oscillatory instability can have the maximum amplification rate as shown in this schematic

as the velocity increases. This instability with $V_1 < V < V_3$ might be directly related with the oscillatory instability of planar front at high growth rates[77, 78]. During the transient growth, when the interface velocity reaches V_1, the growth appears unstable. The interface velocity jumps to V_2. At this time the interface temperature remains still since the velocity jump occurs instantaneously. Then interface temperature and velocity follow the steady state curve for planar front ($V_2 \rightarrow V_3$). When the temperature becomes T_{MAX} with V_3, the interface motion becomes unstable again because of the positive slope of the steady state curve. Then the velocity jumps to the steady state dendrite tip velocity, V_4, instantaneously, and then increases again along with the steady states dendritic growth curve. By repeating this cycle, the interface motion will never reach its steady state, and periodic bands of dendrites and planar front will be shown alternately. In this model, it is assumed that when the solidification mode changes from cellular/dendritic to planar growth and from planar to cellular/dendritic growth, abrupt

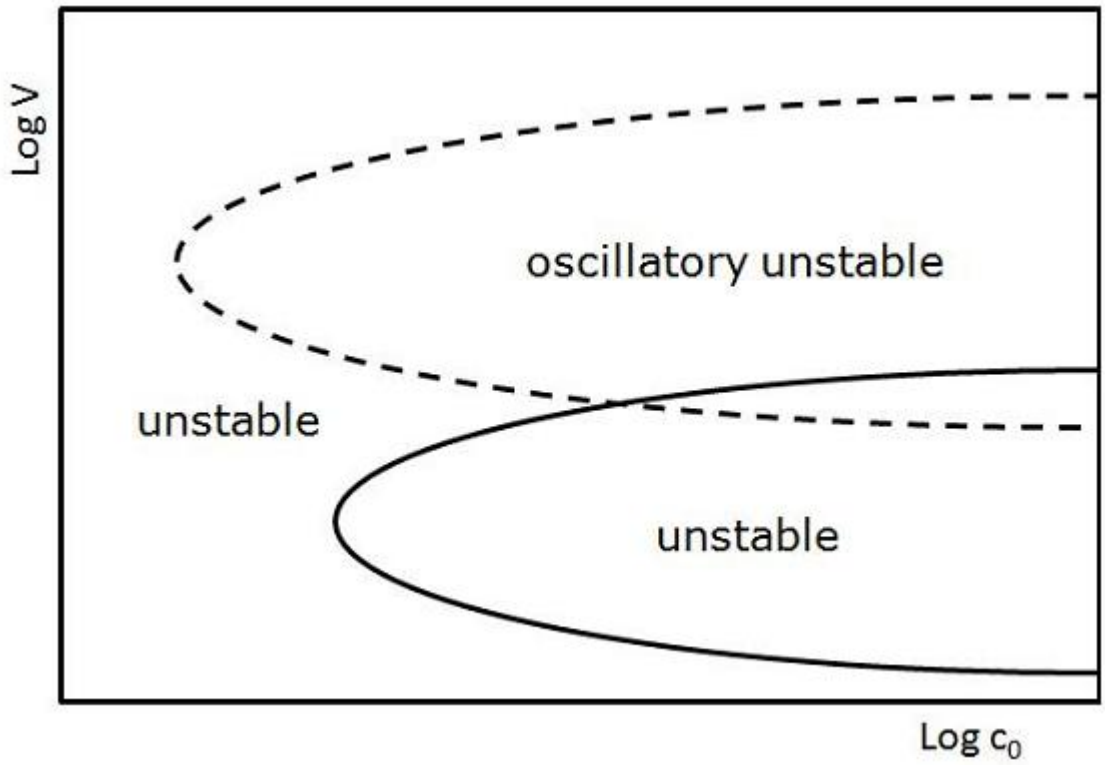

Figure 2.30 A schematic of the neutral stability conditions where the maximum amplification rate is zero for non-oscillatory (solid curve) and oscillatory (dashed-curve) instabilities. For the growth conditions corresponding to the right side of the curves, the planar front becomes unstable.

quasi-instantaneous transition occurs, and between the transitions the steady state is retained. This model is able to explain the alternating occurrence of dark and light bands, and to be used for predicting the quantitative band spacings. However, this phenomenological model is ignored the latent heat generation which might significantly affect the rapid growth dynamics. In order to describe this oscillating dynamics of banded structures quantitatively, the transient interface kinetics as well as morphology evolution should be considered[83, 84, 85, 86, 54].

2.3.4 Numerical analysis of banded structure formation dynamics

Motivated by the phenomenological interface dynamics by Kurz *et al.*[54] for the formation of banded structures and the presumption that oscillatory instability of planar interface

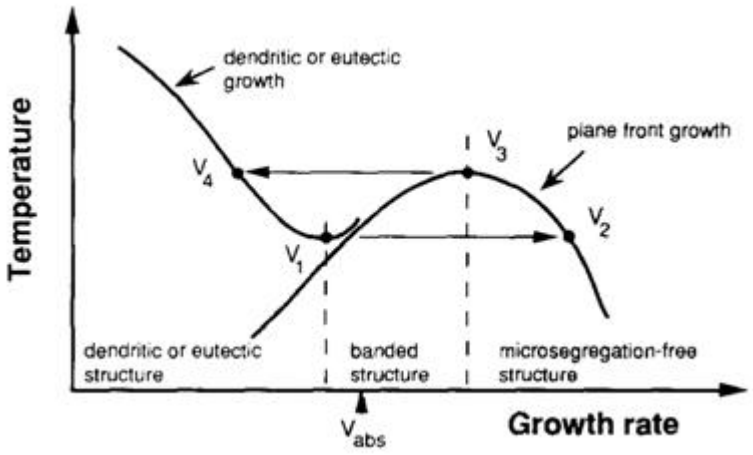

Figure 2.31 The phenomenological model for formation of banded structures. In directional solidification, when $V_1 < V_P < V_3$, the interface dynamics may follow the cycle $V_1 \rightarrow V_2 \rightarrow V_3 \rightarrow V_4 \rightarrow V_1$ and never reach the steady state.[54]

(Merchant-Davis[78]) may trigger the dynamics for the banded structure formation, a numerical analysis was carried out and confirms that the growth condition predicted by Merchant-Davis's stability analysis actually leads to the oscillatory interface dynamics of planar front[80, 81] as suggested in a phenomenological model[54]. Their sharp-interface numerical model of directional solidification[87] employed the solute trapping model of Aziz[2], attachment kinetic effect, and velocity-dependent liquidus from thermodynamically consistent model by Boettinger-Coriell[26] for the boundary conditions at the solid-liquid interface. When the calculation started from a point on the up-sloping part of T_S curve (between V_1 and V_3 in Figure 2.31) under the condition where latent heat is ignored, instantaneous jump of V* to the steady state planar growth branch, followed by the steady state dynamics along the T_S curve toward V_3, and subsequently instantaneous deceleration of V* at T_{MAX} are calculated.

It was also shown that the consideration of latent heat strongly affects the oscillatory instability of planar interface and the time-periodic interface dynamics. A larger thermal diffusivity decreases the range of V_P and c_0 where the oscillatory instability of planar interface should occur and the variation range of V* during oscillatory interface dynamics.

Even though this one-dimensional analysis does not include the effect of the transverse

morphological instability, it still shows an essential feature of interface dynamics responsible for banding phenomenon.

2.4 Phase-Field Simulation Of Rapid Solidification

Since the phase-field model employs a diffuse interface, the interface dynamics can be predicted without any prescribed interface conditions. The interfacial conditions can be implicitly calculated. All the events that occur during growth processes are selected in the direction of decreasing Gibbs free energy density of the system. By considering only Gibbs free energy density of the whole system, the only fundamental force which drives the growth, the natural selection process of rapid growth dynamics can be numerically calculated. More detail of the phase-field model will be described in the next chapter.

In regard to rapid solidification, a couple of phenomenological calculations have been reported. Boettinger and Warren[88] calculated 2-dimensional morphological evolution of a binary alloy under the directional solidification conditions. Starting from the initial planar front, the calculated morphology successfully showed the breakdown of the planar front, evolution of cell structures, and transition of cell structures into planar front during initial transient process. But the calculations were primarily focused on the phenomenological evolution itself, rather than the rapid growth characteristics. In Kim-Kim's calculation[89], it was demonstrated that the banded structure evolution could be simulated by the phase-field calculation. The alternative evolution of dendritic and planar growth has also been successfully shown. Fan *et al.*'s calculation[90] shows the morphology transition from dendrite to planar growth with increasing melt undercooling in the isothermal system.

Solute trapping phenomenon has been investigated with the phase-field model by calculating the steady state planar interface temperature and the solute distribution across the interface in an isothermal system with a given steady state interface velocity. Wheeler *et al.*[91] first showed the possibility of describing the velocity-dependent solute trapping by the phase-field model with a constant chemical diffusivity in both phases. Then Ahmad *et al.*'s calculation[92] with different diffusivities in bulk phases was fitted by Aziz solute trapping

model and showed a good agreement. It was also shown that the solute trapping occurred when D_i/V is comparable to the interface thickness and that the smaller equilibrium partition coefficient may lead to higher characteristic velocity for solute trapping, V_D. D_i is the solute diffusivity across the interface region. In an effort to fit the phase-field simulation result to the Kittl *et al.*'s experimental data[33, 36] which has a slight deviation from Aziz's model at high V range, Danilov and Nestler[93] introduced a new definition of interface concentrations in the phase-field calculation results. The resultant k_V as a function of growth rates deviates with Galenko's model as well as Aziz's model. More extensive experimental data is needed to validate the k_V description.

$V - \Delta T$ behavior of steady state rapid dendritic growth was simulated by Galenko *et al.*[63, 64] in an undercooled melt considering both solutal and thermal diffusion processes. The result could show the $V - \Delta T$ behavior change at a specific undercooling, ΔT^*. The calculated solute and temperature field around the steady state dendrite tip confirmed that there is only a temperature gradient in front of the tip for the undercooling higher than ΔT^*.

The continuous oscillation dynamics of planar front growth under fixed temperature gradients was calculated by Conti[94] in a one-dimensional system. Although the calculation successfully shows oscillating interface dynamics, the calculated cycle of the interface dynamics in T-V space showed some deviation from the model suggested by Carrard *et al.*[54] and the calculation by Karma *et al.*[80, 81]. In the latter model and calculation, there exist the instantaneous acceleration and deceleration of interface velocity with an almost constant interface temperature when the latent heat release is ignored, but Conti's result failed to demonstrate the feature. It can be presumed that the fixed grid spacing used in this work may not be able to sufficiently resolve the phase- and concentration-fields across the interface region, especially when the interface velocity is strongly accelerating.

Table 2.2 Summary of critical investigation in rapid solidification (in chronological order)

AUTHORS (YEAR)	DESCRIPTIONS		MAT.	REF.
Rutter-Chalmers(1953)	Experimental observation of planar interface breakdown Constitutional undercooling criterion	The breakdown of planar interface into cellular morphology was experimentally observed by decanting the melt during growth. The constitutional undercooling criterion in front of the interface was first suggested as a cause of breakdown of planar interface.	Sn- and Pb-base alloys	[4]
Tiller-Jackson-Rutter-Chalmers(1953)	Solute redistribution analysis during the transient Constitutional undercooling criterion	Theoretical analysis of solute redistribution near the solid-liquid interface of binary alloys was made for initial transient and steady state conditions, with a constant interface velocity. A quantitative analysis of constitutional undercooling zone was made.		[8]
Duwez-Willens-Klement(1960), Baker-Cahn(1969), White-Narayan-Young(1979)	The fist observations of solute trapping in rapid solidification	By chill casting, splat quenching, or laser surface melting, it was found that the concentration of solid grown with rapid growth rate could exceed the equilibrium value or even the maximum solid solubility.	Cu-Ag,Zn-Cd,Si-based binary alloys	[17, 19, 20]
Mullins-Sekerka(1964)	Stability analysis of planar interface	The stability of perturbations on a plane front of dilute binary alloys was analyzed under directional growth conditions. For a specific range of interface velocity, perturbations with a specific range of wavelength may grow into cells.		[10]
Baker-Cahn(1971)	Thermodynamic analysis of solute trapping	Thermodynamically possible range of interface concentrations for a given temperature was shown. The notion of 'solute trapping' was first introduced.		[1]

Table 2.2 (Continued)

Sastry-Sryanarayana (1981), Boettinger-Shechtman-Schaefer-Biancaniello (1984)	The first observation of banded structure in rapid solidification	By electron-beam surface melting and splat quenching, banded structure was observed at a velocity range between those for cellular/dendritic or eutectic growth and for planar growth.	Al-Pd, Ag-Cu	[65, 66]
Aziz(1982)	Solute trapping model	A solute trapping model for a dilute binary alloy was presented, which represents the partition coefficient as a function of interface velocity. The model shows that the solute trapping occurs in a finite range of velocity around the diffusive speed of solute in the liquid.		[2]
Coriell-Sekerka(1983)	Non-equilibrium planar interface stability analysis for rapid growth rate	Extension of Mullins-Sekerka (1964)'s linear stability analysis under conditions where the partition coefficient varies with velocities. Novel oscillatory instability of perturbations with significantly large wavelengths was found.		[77]
Boettinger-Coriell-Sekerka(1984)	Analytic solution of T(V) for rapid planar growth	Steady state interface temperature for planar growth of binary alloys was derived as a function of the interface velocity and the initial melt concentration, using Baker-Cahn's thermodynamic driving energy of solidification (1971), Turnbull's collision limited growth model (1975), and Aziz's solute trapping model.		[25]

Table 2.2 (Continued)

Trivedi-Somboonsuk (1985)	Instability measurement during the transient	The morphology evolution from initial flat interface to fully grown steady state dendritic arrays was observed. It was found that the initial perturbation from flat interface starts during initial transient regime of the growth, and that the final steady state morphology is history-dependent.	SCN-acetone	[11]
Lipton-Kurz-Trivedi(1987)	Analytic model of dendrite tip radii and velocities for rapid solidification (LKT model)	The LGK model, analytic model of dendritic growth for small undercoolings by Lipton-Glicksman-Kurz (1984), was extended for high undercoolings by employing the marginal stability criterion for high Peclet numbers.		[50]
Boettinger-Coriell-Trivedi(1988)	Analytic model of rapid dendritic growth (BCT model)	The LKT model was extended by employing the kinetic undercooling and Aziz's solute trapping model.	Ag-Cu	[51]
Willnecker-Herlach-Feuerbacher (1989), Eckler-Gartner-Assadi-Norman-Greer-Herlach(1997)	The first experimental measurement of interface velocities versus undercoolings during rapid growth	By levitation melting, the growth velocities were measured with different melt undercoolings. The measured data was consistent with the prediction of BCT model only for undercoolings lower than a critical value. For undercoolings higher than the critical value, a different mode of growth was observed.	Ni-Cu, Fe-Ni	[38, 95]
Aziz-Tsao-Thompson-Peercy-White(1986), Smith-Aziz(1994)	Experimental measurements of solute trapping	Interface partition coefficients as a function of growth velocities were experimentally measured. Aziz's solute trapping model fits the measured data quite well.	Si-Bi, Al-Cu, Al-Ge, Al-In, Al-Sn	[28, 32]

Table 2.2 (Continued)

Merchant-Davis(1990)	Non-equilibrium planar interface stability analysis for rapid growth rate	The Coriell-Sekerka's stability analysis (1983) was extended by employing Aziz's solute trapping model and velocity dependent solidus from Boettinger-Coriell-Sekerka (1984), for directional solidification with no latent heat generation. For a specific range of pulling velocities and alloy compositions, time-periodic oscillatory instability for zero-wave number was found. This oscillatory instability was presumed as an origin of formation of banded structures.		[78]
Carrard-Gremaud-Zimmermann-Kurz(1992)	Phenomenological model of banded structure formation	A phenomenological model of interface dynamics which may yield banded structures was first suggested. According to this model, the banded structure forms by instantaneous transitions between dendritic and planar growth modes.	Al-Fe, Al-Cu, Ag-Cu	[54]
Karma-Sarkissian(1992, 1993)	Numerical analysis of oscillation dynamics	By numerical calculation of rapid planar directional growth, it was frist confirmed that the oscillatory planar instability predicted by Merchant-Davis (1990) actually leads to the oscillatory interface dynamics suggested by Carrard et al.(1992), and latent heat may significantly alter the oscillatory interface dynamics.	Al-Fe	[80, 81]

Table 2.2 (Continued)

Warren-Langer(1993)	Analytical model of initial transient dynamics	A theoretical analysis of morphology evolution was presented for a directional solidification from initially flat interface to a steady state dendritic array. First, the acceleration of flat interface concerning build-up of solute boundary layer, second, onset of instability of the flat interface during the transient, and last, a steady state primary dendrite spacing are sequentially calculated.	SCN-acetone	[13]
Wheeler-Boettinger-McFadden (1993), Ahmad-Wheeler-Boettinger-McFadden (1998)	Phase-field simulation of solute trapping at a 1D steady state interface	Solute trapping phenomena at the solid-liquid interface of binary alloys were calculated in a one-dimensional isothermal system at a steady state with given velocities. The results are fitted by Aziz's solute trapping model and/or compared with experimentally measured data.	Ni-Cu	[91, 92]
Kittl-Aziz-Brunco-Thompson (1995), Kittl-Sanders-Aziz-Brunco-Thompson (2000)	Experimental measurement of solute trapping	The first measurement of velocity-dependent partition coefficient for the high velocity regime and for non-dilute alloys was performed. The results were reasonably well fitted by Aziz's solute trapping model. The partition coefficient at a most high velocity was slightly deviated from the model, but authors argued that this is due to experimental uncertainty at such a high velocity regime.	Si-As	[33, 36]
Galenko-Sobolev(1997), Galenko(2007)	Solute trapping model	Aziz's solute trapping model was extended, concerning the relaxation time for solute diffusion in the liquid. In contrast with Aziz's model, this model predicts complete solute trapping at a specific interface velocity.		[3, 55]

Table 2.2 (Continued)

Galenko-Danilov (1997,1999)	Analytical prediction of dendritic growth	The BCT model was extended by using Galenko's solute trapping model. The model can be reasonably well fitted to experimentally measured data for very high undercooling range where the linear growth mode exists.	Ni-B, Ni-Cu	[56, 57]
Conti(1998)	Phase-field simulation of oscillatory interface dynamics during rapid solidification	Oscillatory rapid planar interface dynamics in directional growth condition was calculated by phase-field model. The growth parameter range where the oscillatory dynamics can occur was reasonably in agreement with Merchant-Davis's stability analysis, but the interface dynamics itself deviated from the previous model and numerical calculation result.	Ni-Cu	[94]
Boettinger-Warren(1999)	Phase-field simulation of morphology evolution during directional solidification	Time-dependent morphology evolution from initial planar interface to steady state planar or cellular structure was calculated under a directional growth condition by the phase-field model.	Ni-Cu	[88]
Kim-Kim(2001)	Phase-field simulation of banded structure formation	Morphology evolution of banded structure was shown by the phase-field simulation.	Al-Cu	[89]
Fan-Greenwood-Haataja-Provatas(2006)	Phase-field simulation of isothermal rapid crystal growth	Growth mode change with different melt undercoolings accompanied with morphology change and solute trapping was shown by phase-field simulation.	Ni-Cu	[90]

Table 2.2 (Continued)

Danilov-Nestler(2006)	Phase-field simulation of solute trapping at a 1D steady state interface	The velocity-dependent chemical partitioning at the solid-liquid interface of binary alloys was calculated in a one-dimensional isothermal system at a steady state with given velocities. In order to fit to the Kittl *et al.*'s experimental results which has a little deviation for very high velocity, new definition of interface concentrations was used. The results are fitted by the experimentally measured data and compared with several different solute trapping models.	Si-As	[93]

CHAPTER 3. OBJECTIVES AND APPROACH

The primary goal of this work is to investigate the response of the solid-liquid interface to the driving force and its effect on the morphology evolution of alloys in a highly driven solidification condition by means of the phase-field simulation. Toward this goal, the critical questions tackled in this thesis are:

- **How do initial transient dynamics of a planar front vary with pulling velocity during rapid directional growth?**

  The study on rapid alloy growth dynamics at 'non-steady state' has not been sufficiently conducted. The relevance of the non-steady state (transient) alloy growth dynamics to the final steady state growth morphologies have been shown in the Trivedi-Somboonsuk's experimental analysis[11] and Warren-Langer's theoretical analysis[13] for 'low/moderate' rate growth where the local equilibrium at the solid-liquid interface is retained. In rapid directional growth of alloys, it has been considered that the banded structure formation is the result of non-steady state interface dynamics in which the chemical partitioning, the interface kinetics, and morphology evolution are all correlated. However, the calculation of initial transient dynamics of planar directional solidification by Warren-Langer[13] did not consider the solute trapping phenomenon and also was based on the purely solutal-diffusion-controlled interface motion. Thus, Warren-Langer's analytical method cannot be applied to the rapid growth case where the effect of solute diffusion on the growth dynamics becomes diminished by solute trapping at the interface and the effect of atomic attachment kinetics on the growth control becomes stronger. Karma-Sarkissian[80, 81] used the Aziz's model to analytically describe the oscillatory dynamics. But the current research predicts the non-equilibrium partitioning in a more

natural way without a explicit velocity-composition function.

- **Can the phase-field method be used to accurately predict the rapid oscillation dynamics of planar front?**

  There have been a couple of phase-field studies on the banded structure formation which can be observed in rapid directional growth condition. Kim-Kim[89] only reproduced the phenomenological morphology evolution: alternating dendritic and planar growth modes occur in the growth direction. Conti[94] could successfully calculate non-steady oscillatory cycle of planar interface dynamics and the variation of the non-equilibrium chemical partitioning at the interface along the cycle which may form the banded structure. But, the trace of the cycle does not agree qualitatively with those of Carrard *et al.*'s phenomenological model[54] and Karma-Sarkissian's numerical calculation[80, 81]. Due to the sharp-interface limit phase-field model and the fixed 'thick' grid spacing, the Conti's work could not properly describe the instantaneous velocity jump during the cycle. The sharp-interface limit phase-field model could lead to the non-physical solute diffusion across the interface region, and in turn alter the rapid interface dynamics. Conti also used fixed grid spacing throughout the whole calculation. This could give rise to the numerical instability in the calculation: insufficient number of grid points over the interface region may cause invalid interface kinetics.

- **How does solute partitioning (k_V) vary during non-steady state dynamics, i.e. initial transient and oscillation dynamics?**

  Since solute trapping phenomenon is one of the main characteristics of rapid alloy solidification, a velocity-dependent partition coefficient at the steady state has been analyzed with theoretical approaches and numerical phase-field calculations as well as some experimental measurements. However, the experimental data for very high velocity regimes has been limited because of the uncertainties in the measurements as described in the Kittl's experimental studies[33, 36]. Accordingly, the dependency of the partition coefficient on the full range of the steady state growth rate has not been clearly validated. Moreover,

in the growth dynamics, the degree of chemical partitioning is not the parameter which is determined only by the interface velocity. The chemical partitioning, the interface velocity, and the evolving morphology should be mutually correlated. The investigation of this correlation during growth must be a critical factor in the rapid solidification study.

- **Can the phase-field method be used to probe the influence of solute partitioning on the morphology selection in rapid alloy solidification?**

  'Rapid' alloy solidification may be characterized by the non-equilibrium solute partitioning and significant effect of atomic attachment kinetics. Even with the phenomenological and analytical theories developed in the last half century, the understanding of the nature of selection mechanism of the interface dynamics and resulting morphology evolution is still lacking.This is in contrast with 'low/moderate' rate solidification for which the theories have been fairly well established based on numerous experimental observations and measurements. The precise experimental measurements of interface response and the solidification condition during rapid growth are very challenging to quantify, thus it is one of the critical reasons why the study of rapid alloy growth is difficult.

In order to describe the rapid alloy solidification and provide answers for the above questions, we performed the phase-field simulation in highly driven solidification conditions. For more quantitatively valid description of rapid growth dynamics, the phase field model in the thin-interface limit with the anti-trapping current term is utilized. First, one-dimensional calculations for a planar front growth were performed under directional growth conditions with a fixed temperature gradient, to study the initial transient dynamics under rapid solidification conditions. We applied seven different pulling velocities in the range of 1 mm/s˜10 m/s, in which Warren-Langer's model cannot predict the full transient dynamics. The calculations started with the interface temperature close to the equilibrium liquidus temperature for the alloy composition, and continued until the interface velocity and the solute composition in the solid are same as the pulling velocity and alloy composition, respectively. For a pulling velocity which never leads to the steady state and yields oscillatory interface dynamics, the calculations are terminated after several repeated cycles were computed. The computed transient interface

dynamics were compared with Warren-Langer's predictions and analytical descriptions of the steady state temperature of a planar interface with velocities, exposing the limitations of the analytical models and addressing the ability of the current approach to describe the appropriate rapid growth dynamics. The interface concentrations are measured during the transient growth and thus the correlation between chemical partitioning and interface dynamics was exhibited. Second, the steady state growth morphologies in isothermally undercooled melts have been simulated at a fixed melt temperature. With the increasing initial supersaturations, the steady state interface velocities, radii of the curvature, and interface concentrations were measured, and it was demonstrated that the phase-field method can appropriately describe the morphological section associated with the non-equilibrium chemical partitioning as well as the local equilibrium condition. For all computations in this research, materials parameters for Ni-Cu binary alloys were used.

CHAPTER 4. THE PHASE-FIELD MODEL AND THE CALCULATION METHOD

The traditional numerical modeling method used for solidification processes is the sharp-interface model. For this calculation, partial differential equations for each phase should be solved with boundary conditions at the sharp phase boundaries. The difficulty of this calculation comes from as solving all the partial differential equations and boundary conditions, while at the same time, tracing the position of interfaces to apply the boundary conditions.

During the last 20 years, the phase-field model has been utilized extensively to calculate the complex morphological evolution during phase transitions. The model does not explicitly need to track the interface position or to calculate the boundary conditions at the interface. Since those are calculated implicitly, the microstructural evolution in the whole system, i.e. for all the phases, is calculated simultaneously with the one or more order parameters or "phase-fields" along with the appropriate thermal and solutal diffusion parameters and equations. Interfacial properties are incorporated with the energetics of the phase field.

4.1 Basic Theory

4.1.1 Diffuse interface and phase-field variable

The phase-field model adapts the diffuse-interface theory[96, 97, 98], wherein an interface with a finite thickness is used in this model. The concentration or temperature profile is continuously differentiable in this finite interface region, and any other physical properties of the interface are diffused over this interface region.

In Phase-field model, a phase is described with the phase-field variable, ϕ, which is a kind of an order parameter. This variable has a unique value in each bulk phase, and varies

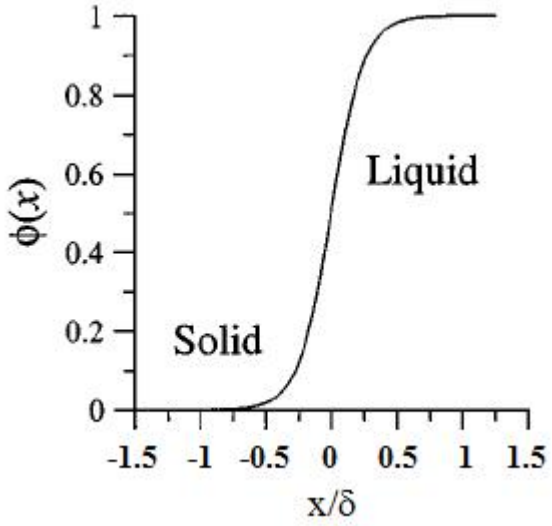

Figure 4.1 Phase-field variable profile over the solid/liquid interface[99] where x=0 is interface position. δ represents the interface thickness. ϕ is zero in solid and unity in liquid bulk phase. In between the bulk phases, the phase variable changes smoothly.

smoothly over the interface region. Thus, the phase-field variable is spatially continuous, and it is a function of time. The exact interface position could be assumed to be where the phase-field variable has the average value of those for the adjacent bulk phases. For example, Figure 4.1 shows the phase-field variable profile over the solid/liquid interface region where δ is the interface thickness, and the phase-field variable ϕ is 0 in solid and 1 in liquid. Other common conventions for phase-field variable is 1 in solid and 0 in liquid, or -1 in solid and 1 in liquid.

The phase-field variable within the interface region is physically meaningful in the order-disorder transition case, where we consider the phase-field variable as the degree of ordering of the state. In the case of solidification, one possible interpretation of the phase variable is the amplitude of atomic density wave function[99]. In the bulk solid and liquid phase, the amplitude of the atomic density function is constant, where as in the interface region, it is gradually changing. Although this could be a physical explanation of phase-field variable, it is originally developed as a purely mathematical concept.

4.1.2 Governing equations

The phase-field model is based on the assumption that the overall rate of evolution is proportional to the variational derivation, $\delta F/\delta\phi$,

$$\frac{\partial\phi}{\partial t} = -M_\phi \frac{\delta F}{\delta\phi} \tag{4.1}$$

where F is the total free energy functional of the system and M_ϕ is phase-field mobility which is a positive value [100, 101]. The total free energy of a system can be postulated as

$$F = \int [f(\phi, T, c, \cdots) + \frac{\epsilon_\phi^2}{2} |\nabla\phi|^2] dV \tag{4.2}$$

where the chemical free energy density, f, is a function of phase-field variable, temperature, composition, and so on. The chemical free energy density forms a double well potential with a free energy barrier between phases. This free energy density function should have the local minima at the value of phase-field variable for a bulk phase. To make this function in this form, auxiliary functions are applied. ϵ^2 is the gradient penalty due to the gradient of phase-field within the interfacial region, which has constant value for an isotropic interfacial energy. The second term in the square brackets represents the energy which is generated by the phase-field gradient over the diffuse interface region. Having a larger interface thickness is energetically favorable since it lowers the phase-field gradient. On the other hand, to decrease the chemical free energy, the interface needs to be sharper since the chemical free energy within the interfacial region is higher than that for the bulk phase. Therefore, the interface thickness is determined by the competitive action of these two energies. Depending on the purpose of the simulation, this free energy functional can include, elastic energy, electrostatic energy, and so on, as well as the bulk chemical free energy and interfacial energy.

Using the free energy functional (Eq. 4.2), the solute diffusion can be postulated as

$$\frac{\partial c}{\partial t} = \nabla \cdot \left[M_c \nabla \left(\frac{\delta F}{\delta c} \right) \right] \tag{4.3}$$

where M_c is the mobility of the solute diffusion field and it is a positive value [98, 102].

Therefore, the governing equations are

$$\frac{\partial \phi}{\partial t} = -M_\phi \frac{\delta F}{\delta \phi} = M_\phi \left(\epsilon_\phi^2 \nabla^2 \phi - \frac{\partial f}{\partial \phi} \right) \tag{4.4}$$

and

$$\frac{\partial c}{\partial t} = \nabla \cdot \left[M_c \nabla \left(\frac{\delta F}{\delta c} \right) \right] = \nabla \cdot \left[M_c \nabla \frac{\partial f}{\partial c} \right] \tag{4.5}$$

4.2 Quantitative Simulation

To decide the values of the phenomenological parameters in the phase-field equation, especially for the case of solidification, mathematical mapping of those parameters of the phase-field equation to the physical parameters of the sharp-interface model is needed since the goal of the phase-field model is to reproduce the results of the sharp-interface model. Especially for the quantitatively reliable simulations, developing an appropriate mapping method is the critical issue since the early ages of the phase-field model.

4.2.1 The Sharp-interface limit analysis

Caginalp[103] showed that the phase-field model in the limit of the vanishing interface thickness can be reduced to the classical sharp-interface model (Stefan problem), and Wheeler, Boettinger, and McFadden[104] and Wang *et al.*[105] obtained the value of the parameters in the phase-field model at this limit, as the simplest way of representing the parameters with the experimentally measurable quantities. In this limit, the temperature variation over the interface region can be regarded as zero and the interface temperature is fixed to the melting temperature in case of pure materials. That makes the analysis simple, and qualitatively reasonable solidification morphologies can be simulated. As results of the sharp-interface limit analysis, Wheeler, Boettinger, and McFadden represents the phase-field model parameters, W, ϵ_ϕ, and M_ϕ as

$$W = \frac{3 a_0 \sigma}{\delta} \tag{4.6}$$

$$\epsilon^2 = \frac{6\sigma\delta}{a_0} \tag{4.7}$$

$$M_\phi = \frac{\mu\sigma T_M}{L\epsilon^2} = \frac{a_0\mu T_M}{6L\delta} \tag{4.8}$$

where W is the height of the energy barrier between the free energies of two bulk phases, and a_0 is a scalar value which depends on the definition of the interface region.

However, because the parameters are derived in this limit, the simulation results cannot properly recover the sharp interface model results unless the interface thickness is very thin, i.e. thinner than or comparable to the capillary length [106, 91, 107, 108, 109], which is on the order of 10^{-9} m for most metals. For properly resolving the interface region, the grid spacing should be smaller than the interface thickness. On the other hand, the scale of the overall microstructural morphology for normal growth conditions is on the scale of microns, and diffusion length scale is on the order of millimeters. Because these span length scales over seven orders of magnitudes, there can be a very high computational cost.

When a thicker interface than the capillary length is used for dendritic growth calculation, the individual values of the dendrite tip radius and velocity considerably depend on the interface thickness and diffuse boundary layer thickness while the Péclet number related with the product of those values is in a good agreement with Ivantsov solution [91, 109]. Therefore, for a practically accessible computational time, the far-field undercooling on the order of L/C_P is required, in which range, a small dendrite tip radius can be obtained [110].

Moreover, the phase-field mobility (Eq. 4.8) is derived under the condition of a negligible curvature undercooling comparing to the kinetic undercooling. Therefore, it is not appropriate to use for the opposite case, i.e. the limit where the kinetic undercooling is negligibly small compared to the curvature undercooling [106].

4.2.2 The Thin-interface limit analysis

To overcome the severe limitations of the sharp-interface limit analysis, in 1996, Karma and Rappel [106, 111] did asymptotic analysis for pure materials which is called the thin-interface limit analysis. This analysis allows to quantitatively reliable phase-field simulations with a relatively thicker interface than the capillary length scale. Simultaneously, this analysis enables the low velocity growth simulation in the regime of the low undercooling less than L/C_P. This results in a vanishing kinetic effect. Whereas the sharp-interface limit analysis assumes that the interface thickness is vanishing so that the temperature field within the interface region is constant, the thin-interface limit analysis is based on the assumption that the interface thickness has finite value, i.e. non-zero, but still much thinner than diffusion boundary layer thickness, $\delta_T = 2\alpha/V$, and tip radius. In addition to the previous assumption, by assuming that the conductivities in the solid and liquid phases are equal, the temperature field over the interface region is derived, and the parameters in the phase-field model are represented with measurable physical quantities. This allows the interface thickness to be on the order of capillary length. By using this thicker interface, relatively low grid resolutions can be used, which is crucial to cut down the computational cost.

With this model, the limitation for the kinetic undercooling can be overcome, and the thick interface width can be used. However, since the equal thermal diffusivities in solid and liquid are used for this analysis, it cannot be applied to the case of unequal diffusivities. When unequal thermal diffusivities are applied to this thin-interface limit model for pure materials, there is a discontinuity of temperature field across the interface region, and an anomalous term in the Gibbs-Thomson equation [112] which is dependent on the interface temperature gradient.

4.2.2.1 The anti-trapping current

To compensate for the solute trapping effect which is a result of chemical potential jump over a thick interface of an alloy simulation by the thin-interface limit, Karma [113] introduced the anti-trapping current term into the solute diffusion equation. For accuracy and numerical

ease, this anti-trapping current term has been adopted in many simulations for dilute binary alloys [113, 114, 115, 116, 117, 118, 119, 120]. By using this anti-trapping current term, the anomalous solute diffusion effect can be effectively controlled regardless of the grid size [121].

However, the model is limited to dilute binary alloys [121], and this artificial current term sometimes makes thermodynamically unrealistic solute profiles in front of the interface. Then Kim [121] extended the anti-trapping current model for dilute binary alloys to multicomponent systems with arbitrary thermodynamic properties.

4.3 Calculation Method

The phase-field simulation is essentially solving the Allen-Cahn equation (Eq. 4.4) and Cahn-Hilliard equation (Eq. 4.5) numerically. All the parameters and functions in those equations, such as a free energy density function, phase-field and concentration field mobilities, and a gradient penalty coefficient must be defined using physical parameters, for physically reliable results. This section will describe the model formulations and the numerical method used for the current study for rapid alloy growth.

In the thin-interface limit model, temperature and/or concentration variations across the interface region are not ignored. That allows quantitative calculations even with rather unrealistically thick interface, whereas δ should be comparable to the capillary length for quantitatively valid simulations in the sharp-interface limit.

In the case of alloys, the difference of solutal diffusivities in the solid and liquid phases is several orders of magnitude. When a relatively thick interface is used, this big diffusivity difference between two adjacent phases causes several spurious interface diffusion kinetics and solute trapping. Karma[113] resolved this problem by introducing the anti-trapping current term in the phase-field evolution equation. This term gives a counterflux against unphysical solute trapping flux. Although this work is for the specific case of dilute, one-sided binary alloys, Tong et al. showed that the same forms of the governing equations can be effectively valid for non-dilute alloys. Their governing equations for isotropic growth are as following:[122]

$$\tau(T)\eta(\hat{n})^2\frac{\partial\phi}{\partial t} = \nabla\cdot\left[W(T)^2\eta(\hat{n})^2\nabla\phi\right]+\phi-\phi^3-\lambda(T)\left(1-\phi^2\right)^2 U+\nabla\cdot\left(|\nabla\phi|^2 W(T)^2\eta(\hat{n})\frac{\partial\eta(\hat{n})}{\partial(\nabla\phi)}\right) \tag{4.9}$$

$$\left(\frac{1+k(T)}{2}-\frac{1-k(T)}{2}\phi\right)\frac{\partial U}{\partial t} = \nabla\cdot\left(D(T)\frac{1-\phi}{2}\nabla U+\frac{1}{2\sqrt{2}}\left\{1+\left[1-k(T)\right]U\right\}\frac{\partial\phi}{\partial t}\frac{\nabla\phi}{|\nabla\phi|}\right) + \frac{1}{2}\left\{1+\left[1-k(T)\right]U\right\}\frac{\partial\phi}{\partial t} \tag{4.10}$$

where $\phi = +1$ in solid phase, $\phi = -1$ in liquid phase, τ is the time scale parameter related to the interface kinetic attachment, η is the anisotropy term, W is the interface thickness parameter which corresponds to $\delta/4$, λ is the coupling parameter between the phase-field and chemical diffusion dynamics, and U is the normalized supersaturation. According to the thin-interface limit analysis [115], the relationship between λ, τ, and W is

$$W = \frac{d_0\lambda}{a_1} \tag{4.11}$$

and

$$\tau = \frac{a_2\lambda}{D}W^2 \tag{4.12}$$

where the capillary length, $d_0 = \Gamma/\Delta T$, $\Gamma = \sigma T/L$, $\Delta T = T_L^e(c_S^e) - T$, $a_1 = 0.8839$, and $a_2 = 0.6267$ [113]. $U = \left(e^u - 1\right)/\left(1-k\right)$, and $u = \ln\left\{\left(2c/c_L^e\right)/\left(1+k-\left[1-k\right]\phi\right)\right\}$

Concerning the anisotropy of interfacial energy, the gradient energy penalty coefficient, ϵ, is a function of the orientation of the interface normal, θ, which is the angle between the direction of normal vector of interface and a reference coordination axis, i.e.

$$\epsilon = \bar{\epsilon}\eta(\theta) \tag{4.13}$$

where $\bar{\epsilon}$ is an average gradient energy penalty coefficient, and η is an interface orientation-dependent term. For an 4-fold symmetric anisotropy of cubic crystals in two-dimensional

system,

$$\eta = 1 + \epsilon_4 cos(4\theta) \tag{4.14}$$

. Considering more general three-dimensional anisotropies of interfacial stiffness, η can be a function of the components of the interface normal, i.e.

$$\eta(\hat{n}) = 1 + \epsilon_1 \left(\sum_{i=1}^{3} n_i^4 - \frac{3}{5} \right) + \epsilon_2 \left(3 \sum_{i=1}^{3} n_i^4 + 66 n_1^2 n_2^2 n_3^2 - \frac{17}{7} \right) \cdots \tag{4.15}$$

For an effective fast calculation, the governing equations are discretized with the fully explicit finite difference method in uniform meshes. The forward difference for the temporal derivatives and central difference for spatial derivatives are used. To make sure the solutions converge, FDM stability condition should be satisfied: $D(\Delta t)/(\Delta x)^2 < 1/2$.

CHAPTER 5. CALCULATION RESULT

5.1 Rapid Directional Growth Dynamics Of A Planar Front

5.1.1 Numerical method

To describe the dynamic response of a planar interface during the initial transient growth stage of binary alloys under highly driven growth conditions, directional solidification in a one-dimensional system is calculated with various pulling velocities, V_P. By being limited to a one-dimensional geometry, we can set aside the curvature effect on growth dynamics and focus on the relationship between solute redistribution and the interface kinetics. In this calculation, the thin-interface limit model with the anti-trapping current is utilized for more quantitatively valid description of the solute diffusion across the interface. Eq. 4.6 and Eq. 4.7 are used as governing equations. Since this is the one-dimensional calculation, the anisotropy term is unity. The parameters to solve these equations are shown in Eq. 4.8 and Eq. 4.9.

The latent heat release at the solid/liquid interface and the heat diffusion process are ignored in this calculation. The parameter λ is first set to $\lambda = 7$. The material parameters of Ni-Cu binary alloys used in this calculation are listed in Table 5.1. The constant chemical diffusivity in liquid phase, $D_L = 10^{-9}\, m^2/sec$, is used and the diffusion in the solid phase is neglected. The polynomials for c_L^e and c_S^e as functions of temperature are obtained by fitting to the equilibrium Ni-Cu binary alloys phase diagram and used for the phase-field calculation.

$$c_L^e = 5.34508\times10^{-11}T^4 + 1.55652\times10^{-9}T^3 - 5.36312\times10^{-6}T^2 - 0.00277367T + 290.9179 \quad (5.1)$$

Table 5.1 The material parameters used in the calculations

	Ni	Cu
Melting temperature (K)	1728	1358
Latent heat (J/m3)	2350×10^6	1728×10^6
Interface energy (J/m2)	0.37	0.29
Molar volume (cm3/mole)	7.42	7.42

$$c_S^e = -4.02814\times10^{-11}T^4+2.03968\times10^{-9}T^3+1.95303\times10^{-6}T^2-0.00277277T-227.622 \quad (5.2)$$

Since the latent heat generation is neglected, the temperature gradient, G, is assumed as a constant. The calculation domain is moving along with the interface. Zero-flux boundary conditions for both phase-field and chemical diffusion field are applied. This boundary condition is reasonable because the domain length is chosen to be large enough so that neither the phase-field nor the liquid solute field would reach domain boundaries. The temperature field is set as

$$T(z) = T^* + G\,(z - z^*) \quad (5.3)$$

where z* is an interface position, T* is the interface temperature, and Δx is a grid spacing. At t=0, the uniform initial liquid concentration equals c_0, and the solid concentration is given as $c_S^e(T(z))$. For all the current calculations, c_0 is set to 0.61, which corresponds to $T_L^e(c_0)$=1547.34 K, and $T_S^e(c_0)$=1497.21 K. The growth starts with $T^*(t=0)$=1546.3 K which is the temperature about 1 K less than $T_L^e(c_0)$, because it needs a small amount of interface undercooling to trigger the growth. Once the calculation starts, the fixed temperature field is pulled with V_P. The calculation continues until it shows the steady state growth behavior which is indicated by the constant $V^* = V_P$ and $c_S^* = c_0$ with time. G=10 K/mm and the range of V_P between 0.001 and 10 m/sec are used in this investigation. According to Eq. 4.8, the interface thickness, W, depends on the parameter λ and the temperature-dependent capillary length, $d_0(T^*)$. Although λ is fixed in this calculation, the interface thickness, W, varies in accordance with T^* during calculations. At each time step, $d_0(T^*) = \Gamma/(T_L^e(c_0) - T^*)$ is

calculated and applied to the governing equations. Since the Gibbs-Thompson coefficient, Γ, and $T_L^e(c_0)$ are constant, $d_0(T^*)$ decreases with T^*, and the interface thickness becomes thinner at the lower T^*. For adequate numerical resolution over the interface region, we continually adjust the Δx during calculations to maintain at least 10 grid points over the interface region.

The thin-interface limit (TIL) phase-field model used in this calculation reduces the possibility of numerical error that comes from an interface that is thicker than the physical solid/liquid interface. For a quantitatively exact description of interface kinetics, the interface thickness for the phase-field model is required to be on the order of the real physical interface thickness. The experimental data of the interface thickness, however, is not available for all the alloy systems and temperatures. Even if we know the physical interface thickness, the phase interface for metallic systems is usually on the order of Armstrongs, making Δx much smaller and the calculation time increases considerably. By using the TIL phase-field model, we expect that the calculation results may be quantitatively valid even if the interface thickness in the calculations is a little thicker than the real interface thickness. The anti-trapping current term has been used to eliminate the unphysical solute diffusion phenomena in the interface region that could be induced by the thick interface in the TIL phase-field model[113]. Such an effort to correctly describe the solute diffusion in the interface region is very important in simulating the rapid solidification dynamics where chemical solute trapping might occur, since the solute trapping phenomenon is closely related to the solute diffusion process across the interface and might have a strong influence on the interface dynamics. For the same reason, temperature-dependent W, which is physically realistic, is necessary since solute trapping phenomenon is very sensitive to the interface thickness.

Figure 5.1 shows ϕ, c, and T-fields at t=0.045 sec with V_P=0.1 m/sec. It is still under initial transient growth and does not reach the steady state. The ϕ-field shows the interface region where ϕ varies continuously from +1 to -1. The exact interface position, z*, is defined as the position where ϕ equals zero. In Figure 5.1, the measured z* is 14.9 μm. Since D_S was ignored, the c-field in the solid phase in Figure 5.1 (b) indicates the trace of c_S^* which gradually increases during this initial transient period. This c-field clearly shows the difference between

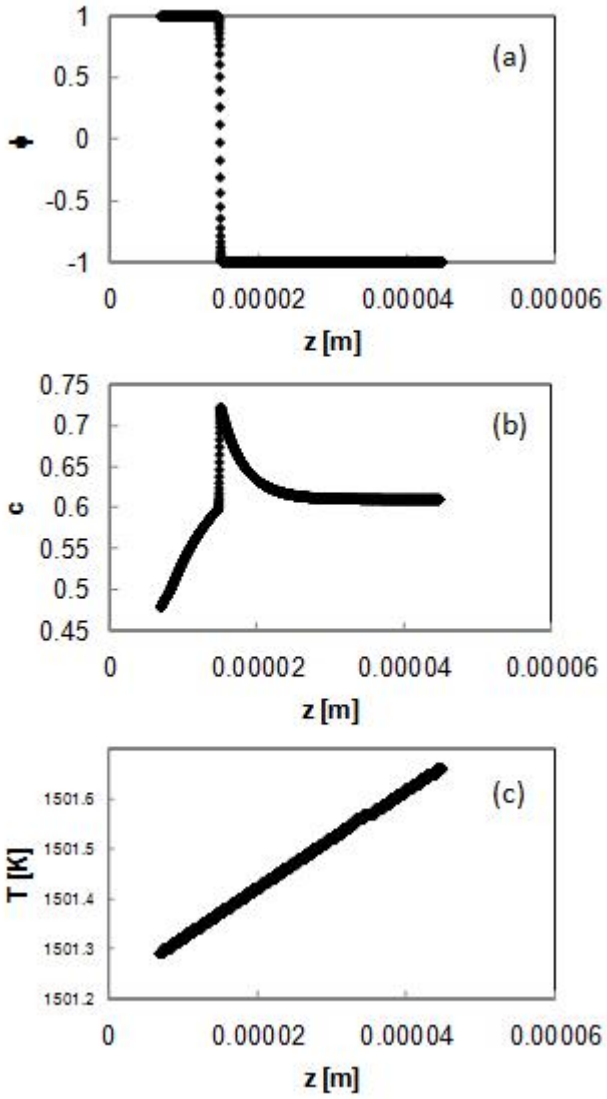

Figure 5.1 (a) The phase-, (b) concentration-, and (c) temperature-fields at t=0.045 sec, calculated with V_P=0.1 m/sec.

c_L^* and c_S^*, which is due to the chemical partitioning. c_S^* is defined as the concentration where it starts to increase near the solid-side interface. c_L^* is identified with the maximum value of the c-profile. We can see the solute diffusion layer in the liquid phase ahead of the interface. The gradient of T-field remains in G. T^* is identified with the temperature at the nearest grid point to $z^*(\phi = 0)$. Since Δx is sufficiently small, this value of T^* is almost same as the temperature at $\phi = 0$.

By tracking the changes of z*, c_S^*, c_L^*, and T^*, the variations of V^* and k_V in time can be obtained. Figure 5.2 is an example of the time-dependent traces of interface conditions, measured from the same calculation shown in Figure 5.1 with V_P=0.1 m/sec. In the Figure 5.2 (c), the solid curve and dashed curve indicate c_L^* and c_S^*, respectively.

5.1.2 Transient dynamics trajectories with various pulling velocities

The variations of T* and V* in time during the initial transient growth with various V_Ps are shown on a T-V space in Figure 5.3. All the calculations are started from the same temperature, T*=1546.3 K (t=0). Once the calculation starts, T* decreases since the temperature field cools at a constant rate and V* is much lower than V_P. After a monotonic decrease of T* with increasing V*, V* suddenly rises at a critical interface temperature, T^+. This abrupt increase of V* continues to a critical interface velocity, V^+. Both T^+ and V^+ seem invariable with V_P. At V^+, both V* and T* increase again if $V_P < V^+$, and if $V_P > V^+$, both V* and T* keep decreasing. Once V* reaches V_P, the steady state condition is generally achieved. In the current calculation, only the calculation with V_P=0.001 m/sec did not reach the steady state and exhibited a continuous oscillation of V* and T*.

5.1.3 Analytical liquidus and solidus curves

These initial transient growth trajectories in Figure 5.3 are compared with the steady state of planar front growth theory. The steady state interface temperature of a planar front as a

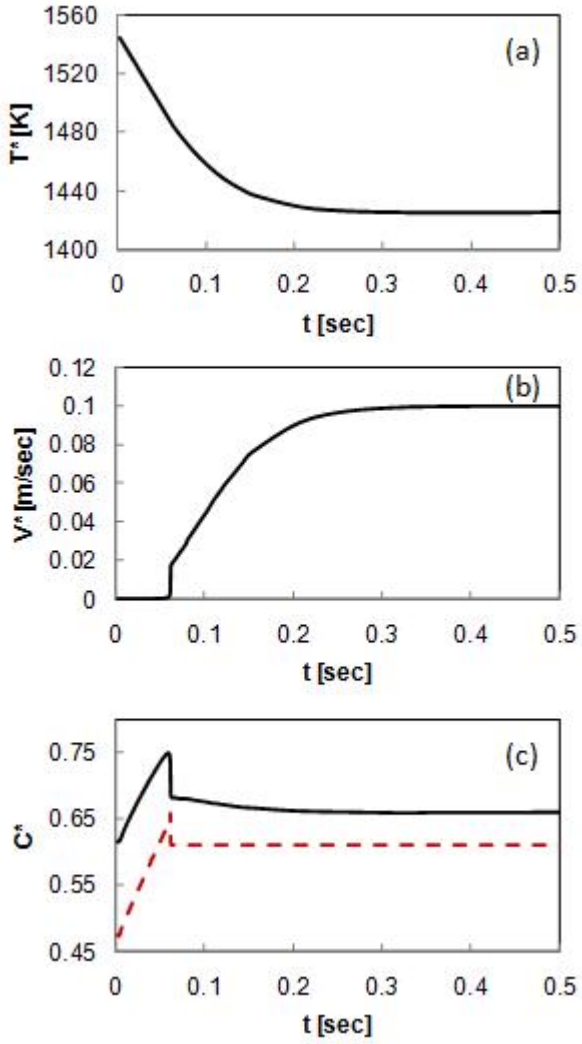

Figure 5.2 The calculated variations of T*, V*, and c* with time for V_P=0.1 m/sec

function of the interface velocity was calculated with the analytical model for dilute alloys[26]

$$T_S\left(c_0, V\right) = T_M^A + \frac{m_L^e c_0}{k_V}\left(\frac{1 - k_V + k_V \ln\left(\frac{k_V}{k_e}\right)}{1 - k_e}\right) - \beta V \tag{5.4}$$

where T_M^A is the melting temperature of the pure solvent material and m_L^e is the slope of equilibrium linear liquidus line. β is the attachment kinetic coefficient (=$1/\mu$). $k_e = c_S^e/c_L^e$ is the equilibrium partition coefficient at the interface for c_0. Since linear solidus and liquidus lines are assumed in this model, k_e is constant with temperature. The temperature calculated by this model is the same as the solidus temperature for c_0 in a kinetic phase diagram which depends on the interface velocity. Thus, the liquidus temperature for c_0 is

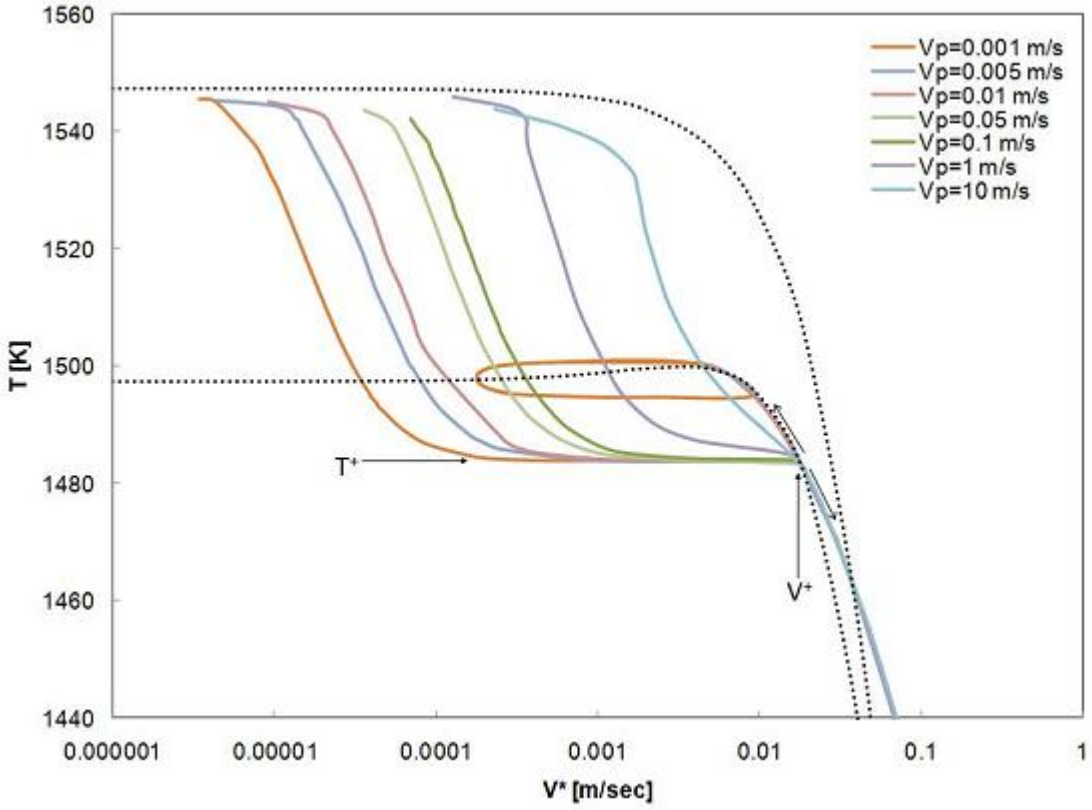

Figure 5.3 The calculated traces of T* and V* during the transient directional growth with various V_Ps. The dotted curves are theoretical prediction of the kinetic solidus and the liquidus temperatures for c_0=0.61.

$$T_L\left(c_0, V\right) = \left(1 - k_V\right)\left(T_M^A - T_S\left(c_0\right)\right) + T_S\left(c_0\right) \tag{5.5}$$

where the solidus temperature, $T_S(c_0)$, is calculated by the previous temperature. Solute drag effect is ignored in this model. For k_V, Aziz's solute trapping model is applied. By using the values of V_D=0.016 m/s and β=2000 K sec/m, we could obtain the solidus and liquidus temperature curves (dotted curves in Figure 5.3) which are roughly consistent with the steady state temperature calculated by the current simulation results. Since this analytical model is for dilute solutions and straight solidus and liquidus in the phase-diagram, the exact agreement with the current simulation results is not expected. Even so, the analytical theory is consistent enough with the current results to associate the steady state temperature with the initial transient solidification path.

From the comparison with the steady state T-V curve, T^+ is slightly lower than T_S^e and V^+ corresponds to the steady state temperature for planar front growth at T^+. Once V* reaches V^+, the transient interface dynamics might follow the steady state T-V curve regardless of V_P. The critical temperature T^+ could not be described by the steady state analytical theory.

5.1.4 Continuous oscillation dynamics

All the calculated initial transient growth paths after passing V^+ follow the steady state curve until V* reaches V_P, except for V_P=0.001 m/sec. The steady state is not achieved with V_P=0.001 m/sec. Figure 5.4(a) shows the calculated data for V_P=0.001 m/sec (solid diamonds) with the analytically predicted steady state for planar front (the dotted curve). The dynamics is consistent with the proposed banded structure mechanism without latent heat generation[73, 54, 80, 81]: the cycle, $4 \rightarrow 1 \rightarrow 2 \rightarrow 3 \rightarrow 4$, repeats. The only difference with the band formation model is that there is the steady state tip operating points for cellullar/dendritic or eutectic growth between the path $2 \rightarrow 3$ as shown in Figure 2.31. Since this calculation is only for the planar-front growth, the dynamics cannot be related to that of the dendritic growth, but the fundamental dynamics is consistent. According to Karma's numerical calculation, the processes of $4 \rightarrow 1$ and $2 \rightarrow 3$ occur almost instantaneously, and T* does not change[80, 81]. The current calculation could successfully show the velocity jump with a constant T*. As shown

in Figure 5.4 (b) of V*(t) for the same calculation, $4 \rightarrow 1$ and $2 \rightarrow 3$ occur instantaneously comparing with $3 \rightarrow 4$ or $1 \rightarrow 2$, and T* stays almost constant during these processes as shown in Figure 5.4 (a). This is the difference with Conti's phase-field calculation results. Conti has been calculated this continuous oscillation dynamics with the sharp-interface limit phase-field simulation with a fixed Δx. In the result, however, the instantaneous velocity jump occurs with a increasing T*. This is not consistent with the current results and Karma's calculation as well as Kurz's model. The difference seems to come from the fixed grid spacing Conti used. During the rapid acceleration at high V*, the phase-field across the interface region may be influenced, and the interface thickness may decrease. The grid spacing should be small enough to resolve the interface thickness for a proper description of interface dynamics. However, in Conti's calculations, the fixed grid spacing has been used throughout the whole calculation and the grid spacing is just small enough to resolve the equilibrium phase-field profile across the interface region. That might cause the numerical instability of the calculations at high V* regime.

5.1.5 Analytical model for initial transient dynamics

These T-V trajectories calculated by the phase-field simulations were compared with the analytical solution for initial transient dynamics of planar fronts. Interface response to the controlled growth environment was analytically calculated by Warren and Langer[13]. This model is based on the assumptions of the local equilibrium at the solid-liquid interface and equilibrium solute profile in front of the interface which is assumed to be an exponential profile.

Figure 5.5 shows transient planar interface dynamics calculated using Warren-Langer's analysis. T* and V* are obtained by T*= $T_L^e(c_0) - G(z_L^e - z^*)$ and V*=dz*/dt+V_P from Eq. 2.8 and Eq. 2.9. The T_L and T_S curves in Figure 5.3 are also included in this figure for comparison. The eight different V_Ps,10^{-7}, 5×10^{-7}, 10^{-6}, 2×10^{-6}, 6×10^{-6}, 10^{-3}, 5×10^{-3}, and 10^{-2} m/s, are used here. The same values of c_0, G, and D_L in the phase-field simulations are applied, and for $T_L^e(c_0)$ and k_e, 1547.34 K and 0.82544 are used, respectively. Unlike the original model, k_V obtained by Aziz's solute trapping model has been used instead of k_e. For

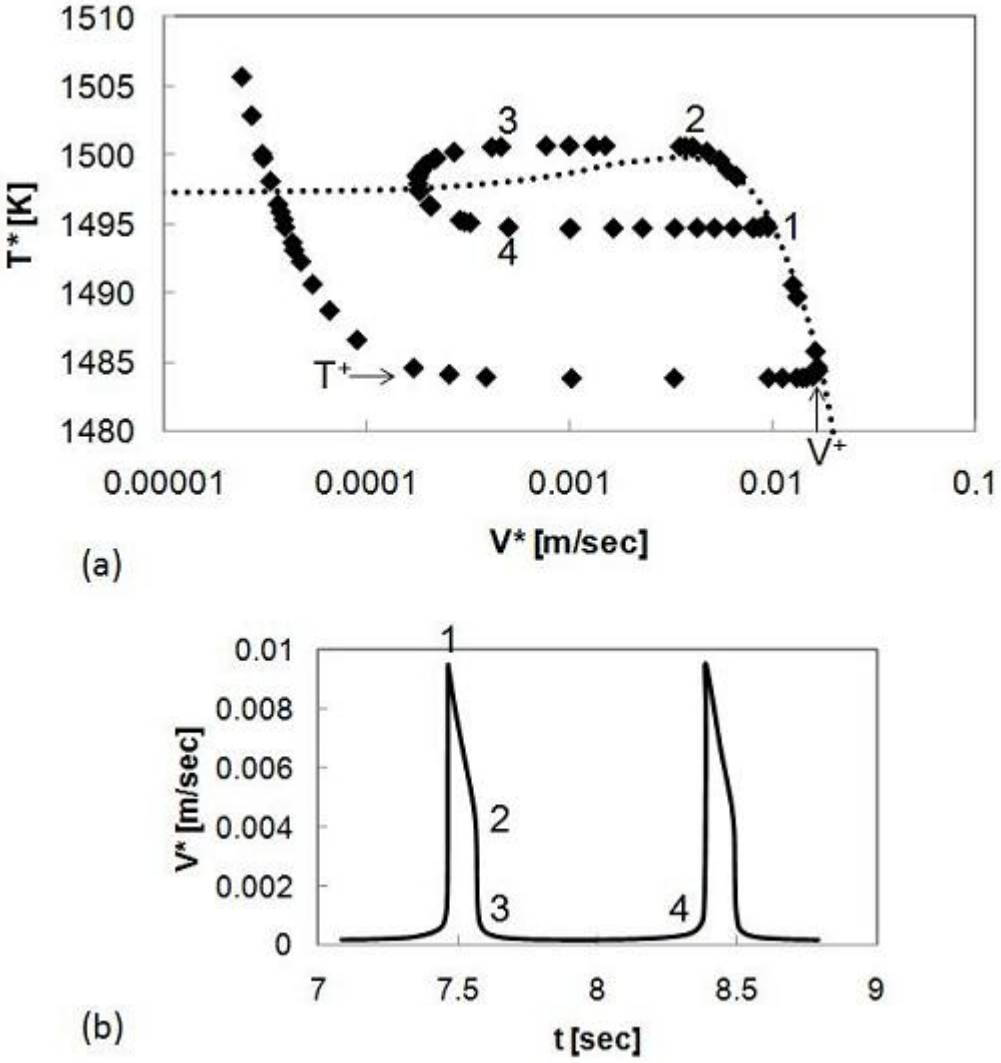

Figure 5.4 The calculated interface dynamics with $V_P = 0.001\, m/s$.

the calculation of k_V, V_D is set to 0.016 which is the value used for the estimated $T_S(V)$ curve. T* starts from near $T_L^e(c_0)$ at the beginning of growth and reaches the steady state temperature.

In Figure 5.5, with increasing V_P, T*-V* behavior changes from monotonic decrease (V_P^1) to oscillatory behavior (V_P^{2-5}). For sufficiently low pulling velocities (V_P^1), starting from T*=$T_L^e(c_0)$ and V*=0, T* and V* keep decreasing and increasing, respectively, until the steady state. For higher pulling velocities (V_P^{2-5}), the highly accelerated interface dynamics yields oscillatory response of T* and V* until the steady state. The amplitude of the oscillation increases with V_P. With a high enough V_P (V_P^{6-8}), the oscillation amplitude becomes so large that T* reaches a critical temperature T^+ during the oscillation, and the interface accelerates abruptly. When the abrupt acceleration occurs, δ_c and dz*/dt go to zero and infinity, respectively, in the Eq. 2.8 and Eq. 2.9. Thus, the calculation cannot proceed further with this analysis. Although this analysis uses some approximations, we believe that this zero-δ_c phenomenon is physically realistic and related to the solute trapping effect in the rapid solidification.

5.1.6 Comparison with an analytical model

As shown in Figure 5.5, there is a limit to V_P where the analytic model can predict the full trajectory of the initial transient dynamics. In contrast, the phase field simulation could be utilized for any V_P without such a limit. However, the phase-field simulation with a low V_P requires extremely large amount of calculation time because large δ_c and slow V* require a larger system size and longer solidification time. Thus, in the current work, the dynamics with V_P=0.001 m/sec and the higher V_Ps are calculated with the phase-field model. This range of V_P is above the limit that the Warren-Langer model can describe the full dynamics with for the growth condition used in the current study. Nevertheless, we could compare the phase-field simulation results with only the valid part of the dynamics from the analytical calculation results.

The V_Ps used in these calculations are 0.001, 0.005, 0.01, 0.1, 1, and 10 m/s. The solid

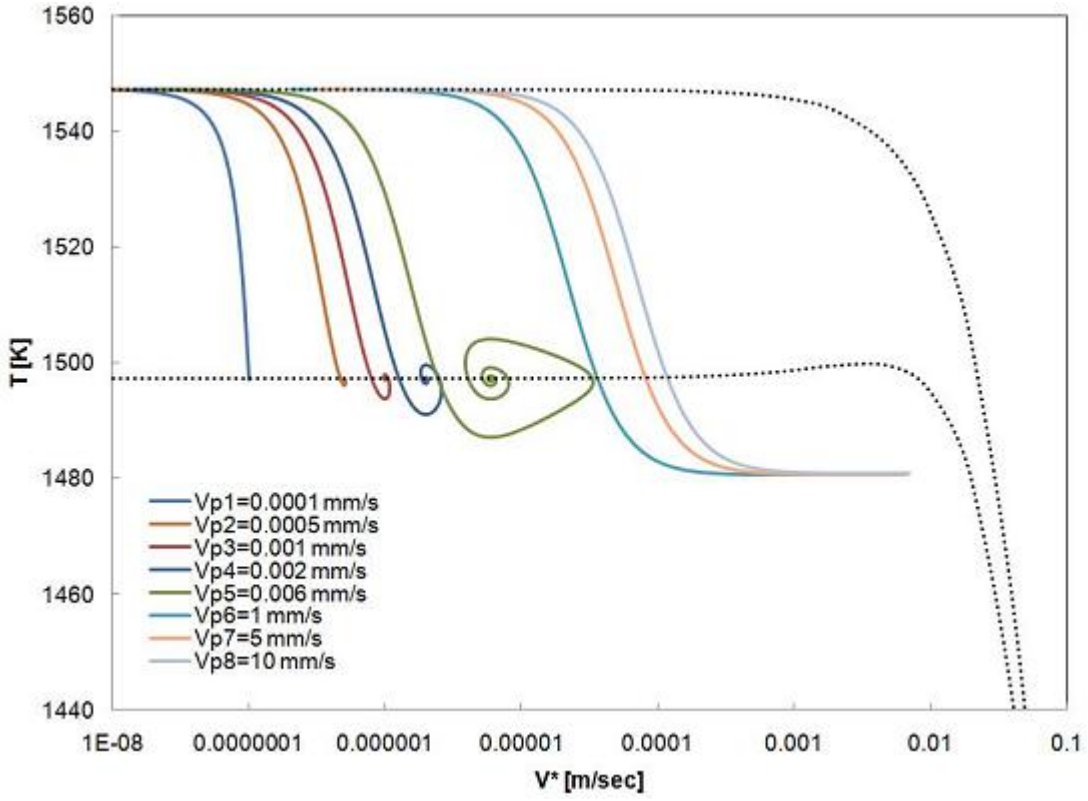

Figure 5.5 Initial transient interface dynamics calculated with Warren-Langer's model with various V_Ps. The dotted curves are the kinetic solidus and liquidus temperature predicted in Figure 5.3. For $V_P \geq 1$ mm/s, the full transient dynamics could not be described.

curves in Figure 5.6 are from the analytical calculations and symbols are from the phase-field simulations. This comparison shows that the phase-field calculation results are reasonably consistent with the valid part of the analytical calculation. The slight difference might result from the temperature-independent k_e assumption used in Aziz's model. While Warren-Langer's model fail to describe the dynamics after the steep rise of V*, the phase-field simulation is capable to show that the growth mode changes at a specific velocity, V^+, and the oscillation dynamics.

5.1.7 Chemical partitioning path for continuous oscillation

These planar front dynamics with high rates might be strongly related with the solute partitioning effect at the solid-liquid interface. During the initial transient process, the variation of k_V is measured at the interface. Figure 5.7 (a) shows the trajectory of measured ΔT^* and V* from the phase-field simulation with V_P=0.001 m/sec. This is the pulling velocity that yields the continuous oscillation. In Figure 5.7 (b), the dotted curve indicates measured k_V and V* during the same solidification process. This k_V is defined as $k_V = c_S^*/c_L^*$. The red dashed curve indicates the $k_e(T)$ that corresponds to the ΔT^* shown in Figure 5.7 (a). Since the growth process starts with ΔT^*=0 K and V*=0 m/sec, both ΔT^* and V* slowly increase, but V* is much smaller than V_P until ΔT^* reaches ΔT^+. In this regime, as seen in Figure 5.7 (b), the measured k_V (blue dotted line) is the same as the k_e. Then k_V is found to deviate from the value of k_e when ΔT^* becomes close to ΔT^+. This is the point which exactly coincides with the beginning of the steep rise of V*. As V* approaches V^+ the increase of k_V with V* stops and then k_V decreases again until the increase of V* stops at V^+. Since for this V_P=0.001 m/sec V^+ is higher than V_P, V* decreases again. As shown before, the interface dynamics at this time follows the steady state operating points for the planar front. During the continuous oscillation cycle, k_V is oscillating with V*. At the lowest V* in the cycle k_V is found to be close to k_e. This indicates that the lowest end of V* in the cycle is determined by the k_V.

Figure 5.8 shows the trajectories of ΔT^* and k_V as a function of V* for V_P=0.1 m/sec. Similar to the Figure 5.7 (b), the red dashed curve represents the k_e which corresponds to the ΔT^* at the moment shown in Figure 5.8 (b). Until V* reaches V^+, the k_V behaves alike the case of V_P=0.001 m/sec. Then as V* keeps increasing until the steady state, the k_V also gradually increases.

5.1.8 The role of the solute trapping phenomena

In this measurement, until ΔT^* approaches ΔT^+, the local equilibrium is maintained. According to the continuous growth model by Aziz, this means that V* is low enough that

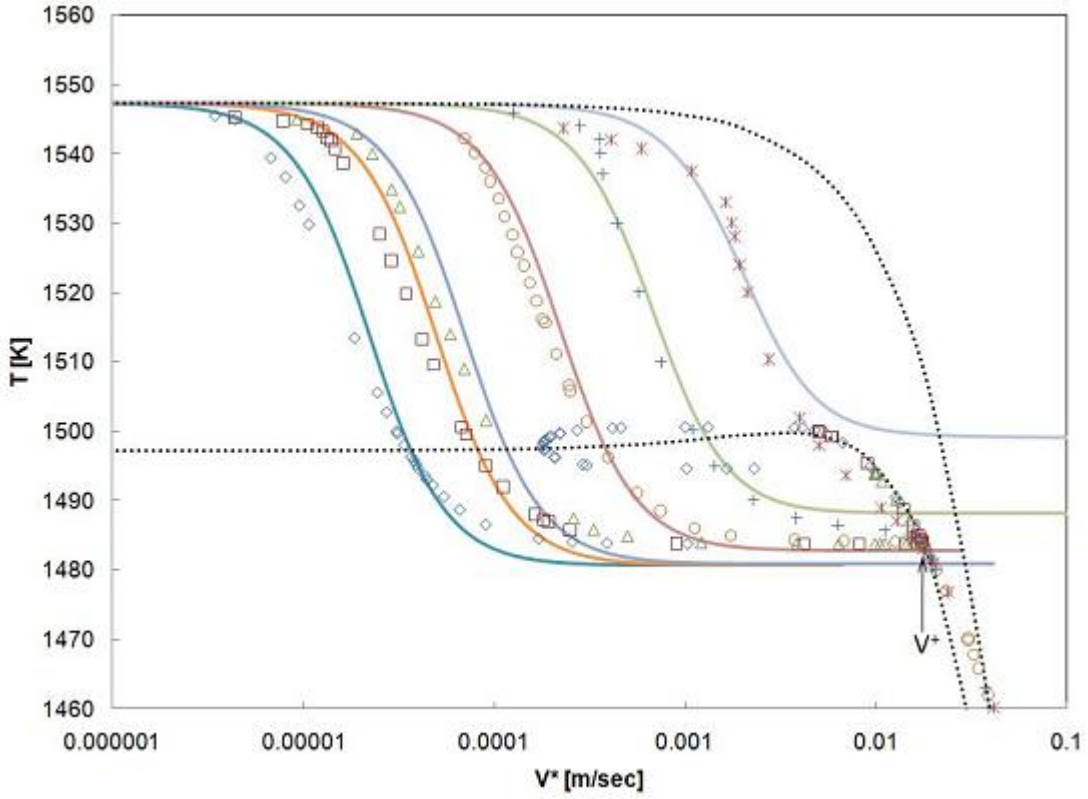

Figure 5.6 The comparison of the phase-field results with the analytical model predictions.

it allows sufficient time for the solute element to fully diffuse across the interface region and that the local equilibrium can be maintained. During the steep rise of V* at ΔT^{+}, ΔT^{*} remains almost constant. This means that the total driving energy for solidification is also not varying while both k_V and V* increase. This can be interpreted that the driving energy to drastically increase the V* originated from only solute trapping at the interface. The extremely high V* might not be able to be achieved with k_e at the interface. At this point, it should be mentioned that we are trying to consider the solute trapping phenomena as a process for saving sufficient driving energy to move the interface. The Gibbs free energy difference between solid and liquid phases can be dissipated by driving the interface motion, changing the interface curvature, or diffusing solute across the interface. The current calculation is limited to one-dimensional systems, and the effect of curvature is not being considered. A system containing an undercooled melt transforms toward the direction of lowering the energy of the whole

system by spending the Gibbs free energy of solidification on both increasing velocity and solute diffusion across the interface (i.e. chemical partitioning at the interface). Therefore, it could be said that the driving energy for the steep rising of V* with an almost constant ΔT^* is achieved by increasing k_V. That means the solute partition can be suppressed to decrease the need for solute diffusion across the interface and to use this saved energy for inducing faster interface velocity. To a certain extent, this is opposed to the interpretation of solute trapping phenomena by Aziz. It is similar to the solute drag, but the solute drag phenomena during solidification is not well analyzed or established yet[53, 58, 92, 123, 124, 125, 36, 126, 127, 128, 63, 129].

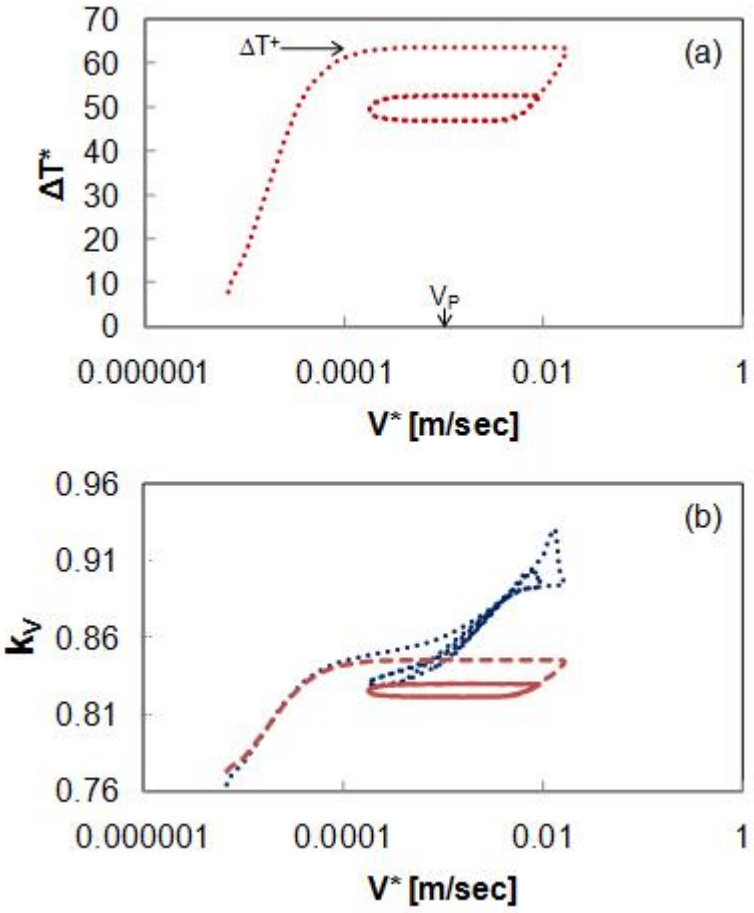

Figure 5.7 (a) Interface undercooling versus interface velocity during transient dynamics with V_P=0.001 m/s. (b) The k_V variation during growth dynamics for V_P=0.001 m/s (the dotted curve). $k_e(T^*)$ trajectories is also shown for comparison (the dashed curve).

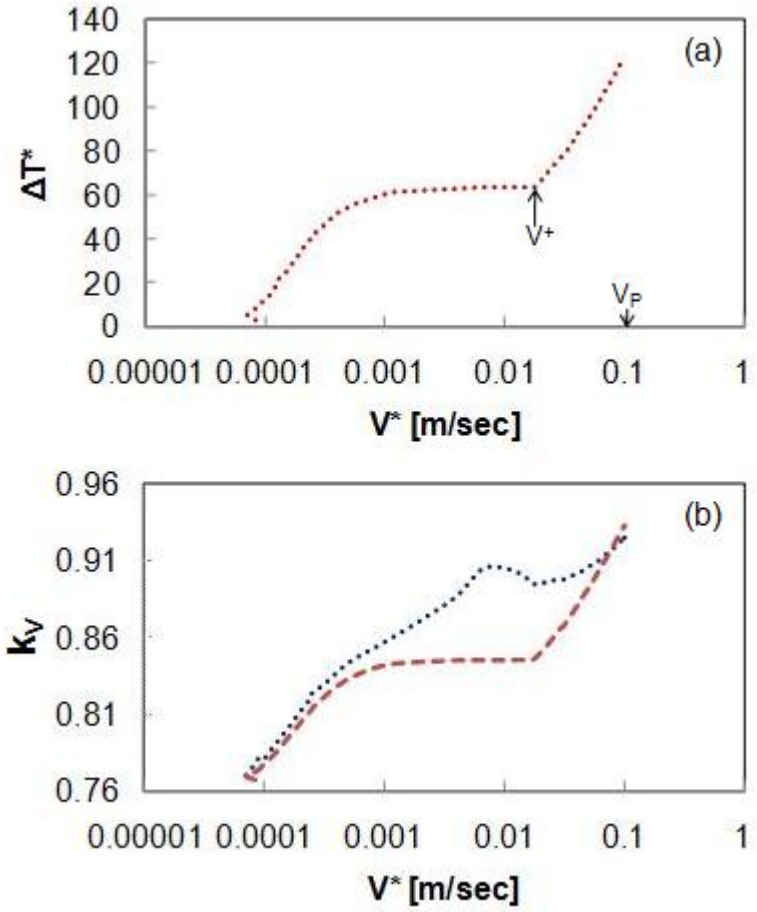

Figure 5.8 (a) Interface undercooling versus interface velocity during transient dynamics with V_P=0.1 m/s. (b) The k_V change during growth dynamics for V_P=0.1 m/s (the dotted curve). $k_e(T^*)$ trajectories is also shown for comparison (the dashed curve).

5.1.9 Effect of the interface thickness on the interface dynamics

According to the Eq. 4.8, the ratio of W to $d_0(T^*)$ is λ/a_1. Since a_1 is a constant, λ is the parameter directly related in determining the interface thickness, W. If we use very small value of λ˜0.2 that makes $W/d_0(T^*)$˜1 from the beginning of the calculation, the quantitatively valid results might be guaranteed. However, the small W requires much smaller Δx and Δt. This makes computations challenging. Especially at the beginning of the initial transient growth, V* is relatively much slower than V_P and δ_c is much longer than that at the steady state. This

causes that the computation with λ=0.2 is impractical. For a reasonable calculation time, a bigger λ value might be required as long as it still allows quantitatively valid results.

In all the calculations shown before, λ=7 is used. For V_P=0.1 m/s, the initial transient dynamics with λ=3 and 2 have been computed and the results are shown in Figure 5.9 (solid curves). The most noticeable difference on the dynamic paths is V^+ which is the velocity that the abrupt V* increase at T^+ stops. As in the case of λ=7, the approximated steady state planar front operating points (dotted curves) calculated by the analytical model are roughly fitted to the computed initial transient dynamics. The parameters used for this approximation are listed in Table 5.9. The interface dynamics from the phase-field simulations are in reasonable agreement with the analytically calculated steady state curves. The steady state T* from the phase-field simulations are changed with λ. For λ=3, the minute oscillation dynamics were found without the steady state. According to the comparison with the analytical steady state curves, this variation of the final T* and different dynamics come from the change of V_D and β by λ.

According to the comparison above, smaller λ in the phase-field calculations results in larger V_D and smaller β. The smaller interface thickness determined by smaller λ allows easier transport of solute atoms across the interface, and thus the solute trapping occurs at the higher velocity range. Since V_D measures the velocity range the solute trapping occurs, it is reasonable that V_D increases with λ. In the phase-field model[115], the interface kinetic coefficient, β, depends on the solute distribution in the diffused interface and the maximum value of β would be $\beta_0 = a_1\tau/(\lambda W)$. By choosing $\tau = a_2\lambda W^2/D$ as in the current study, the maximum kinetic coefficient, β_0, would be $\beta_0 = a_1 a_2 W/D = a_2 d_0 \lambda/D$. The current calculation results are well representing the influence of λ on β.

Table 5.2 Kinetic parameters used for estimating the velocity-dependent solidus temperatures

	V_D [m/s]	β [sec K/m]
$\lambda = 7$	0.016	2000
$\lambda = 3$	0.082	540
$\lambda = 2$	0.19	290

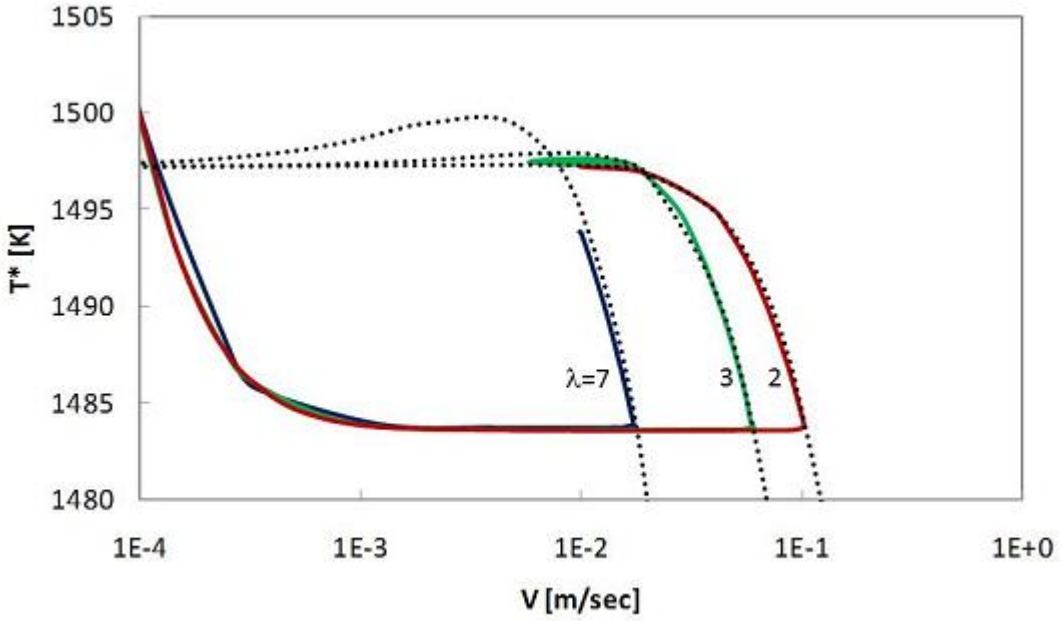

Figure 5.9 A part of the transient interface dynamics calculated with the phase-field simulation for V_P=0.1 m/s with different value of λ.For each phase-field simulation result, T_S curve in Eq. 4.13 was calculated by fitting.

5.1.10 Influence of latent heat

In the current calculations, we have ignored the latent heat release at the solid/liquid interface, and thermal diffusion calculations are not included. When we ignore the latent heat generation, the numerical calculation result shows a qualitatively consistent shape of the interface dynamics with the model proposed by Kurz *et al.*. But, especially for very high growth velocities, it has been shown that the latent heat has great influence on growth dynamics[80, 81]. If we consider latent heat generation and its diffusion process during growth, the orbit of the dynamics can be changed significantly. Since for higher V the latent heat generation affects the interface temperature more significantly, the heat diffusion process should be considered for the complete analysis of highly driven growth process. It is necessary to incorporate the thermal diffusion calculations into the current study for a more comprehensive analysis.

5.1.11 Summary

- Planar interface response to highly driven growth conditions was investigated which is difficult to measure experimentally. The phase-field model in the thin-interface limit with the antitrapping current was utilized. We have shown the initial transient growth dynamics of binary alloys with different high V_Ps under a fixed G. Using phase-field simulations, the interface response to the system's free energy could be analyzed.

- There was a critical temperature, T^+, where the interface velocity abruptly increases during the initial transient growth with a high V_P. During this abrupt increase of V*, the interface temperature stays almost constant at T^+ and severe solute trapping occurs. This T^+ is lower than the equilibrium solidus temperature and not influenced by V_P and the interface thickness. Even Warren-Langer's model can predict this T^+. If V_P is low enough that the interface temperature could not reach T^+ during the initial transient, the interface dynamics exhibits monotonic behavior or damping oscillating dynamics until it reaches the steady state.

- The interface dynamics calculated by the phase-field simulation shows good consistency with Warren-Langer's analytical model which is incorporated with Aziz's solute trapping model. Unlike the analytical model, the phase-field simulation can compute the interface dynamics after the abrupt increase of the interface velocity at T^+.

- The interface dynamics after the abrupt increase of V* at T^+ exhibits a good agreement with the analytical model of the steady state for the planar front. The steady state interface temperature was determined by the steady state operating point corresponding to the V_P.

- The continuously oscillating interfacial behavior which occurs with a specific range of V_P is more consistent with that of banded structure dynamics proposed by Kurz *et al.*[73] and numerically calculated by Karma, than Conti's phase-field simulation.

- The parameter λ which determines the interface thickness in the phase-field model

changes the highly driven interface dynamics and the steady state. This is because λ influences physical solute trapping phenomena as well as the numerical interface mobility. With a smaller λ, higher interface mobility can be achieved and solute trapping occurs at a higher velocity range. This directly affects the initial transient dynamic and steady state temperature.

- From the observation of solute trapping during the rapid increase of V* at T^+, the solute trapping phenomena seems to induce the rapid increase of V* at a constant temperate. Under the condition where a limited free energy is available, solute diffusion across the interface has to be suppressed to increase the interface velocity.

- For a more complete description of the rapid growth dynamics of realistic systems, thermal diffusion calculation should be included, since in the rapid growth the latent heat release could affect the interfacial dynamics more significantly.

5.2 Morphology And Velocity Selection In The Undercooled Melt

5.2.1 Numerical method

The previous one-dimensional calculations of the planar growth allowed us to ignore the curvature effect (i.e. morphology evolution). In this work, we simulate the two-dimensional equiaxed growth of binary alloys in an undercooled melt with the phase-field model, taking into account of the morphology effect. The Eq. 4.6 and Eq. 4.7 are used as governing equations. The latent heat release at the solid/liquid interface during the growth process is ignored in this calculation so that we do not calculate heat diffusion process and the melt temperature is fixed at a uniform temperature. W and τ are determined by Eq. 4.8 and Eq. 4.9. The 4-fold symmetric anisotropy is applied, i.e. $\eta(\theta) = 1+\epsilon_4\cos(4\theta) = (1-3\epsilon_4)[1+4\epsilon_4/(1-3\epsilon_4)(n_x^4+n_y^4)] = \eta(n)$. At all the boundaries of the calculation domain, zero-flux boundary conditions are applied for both ϕ and c-fields. To avoid the influence of the domain boundaries, the calculation domain size is increased during the calculation before the tail of solute boundary layer reaches the domain boundary.

The materials parameters of Ni-Cu binary alloy are in Table 5.1 for these calculations. The solute diffusivity in the liquid phase is set to $10^{-9}\ m^2/sec$. The solute diffusion in the solid phase is neglected. To calculate the supersaturation, U, as a function of the temperature and the undercooling, ΔT, as a function of the concentration, polynomial expressions of $c_L^e(T)$, $c_S^e(T)$, and $T_L^e(c)$ are obtained by the best fit to the equilibrium phase-diagram of Ni-Cu binary alloys (Eq. 4.10 and Eq. 4.11).

The isothermal temperature is set to T=1574 K. At this temperature, the values of c_L^e and c_S^e are 0.459595 and 0.394839, respectively, and the equilibrium partition coefficient is k_e ≈0.86. Initial concentrations, c_0, used for this work are 0.310657, 0.388364, 0.40601, 0.412504, 0.418999, 0.425494, 0.433693, and 0.440168. Those concentrations correspond to the initial supersaturations, $\Omega_0 = (c_L^e - c_0)/(c_L^e - c_S^e)$, 2.3, 1.1, 0.83, 0.73, 0.63, 0.53, 0.4, and 0.3, respectively. Except the cases of c_0=0.433693 and 0.440168, λ=0.2 is used to ensure $W \approx d_0$. This interface thickness could be regarded as a real interface thickness scale. With this scale of the interface, it is expected that there is no numerical artifice induced by the diffused interface. For the calculations of c_0=0.433693 and 0.440168, λ=0.5 and 0.8 are used respectively to expedite the calculations with low growth velocities. The four-fold anisotropy of the interfacial energy (ϵ_4) is chosen as 0.04. This value of the anisotropy is much larger than that for the typical interface anisotropy of metal alloys which is less than 0.01. However, this large anisotropy reduces the calculation time needed to obtain the steady state morphologies since a larger anisotropy increases the dendrite tip velocity and decreases the tip radius. The generic grid spacing is Δx=0.4W, which means that the equilibrium diffused interface includes ten grid points. To accelerate the calculation, the grid spacings for far-field of liquid phase are set as twice that of the generic grid spacings in the solid phase and the diffused interface region. In this coarse-grid region, the phase-field is constant as ϕ=-1 because it is the liquid-only region. The fine grid region expands continuously in size along with the varying dendrite tip position during the calculation so that the interface and solid phase region are always included within the fine grid region. At t=0, a small triangular solid seed with c_0 is placed at the lower left corner. The tip velocity is identified by the rate of varying interface position with time,

along the coordinate axes. The tip radius is calculated by parabolic fitting.

5.2.2 Morphological transition

Figure 5.10 shows calculations of the steady state morphologies at an isothermal condition; different morphologies are predicted with c_0. The initial concentrations for these calculations are c_0=0.40601, 0.388364 and 0.310657. Those initial concentrations correspond to the initial supersaturations, Ω_0=0.83, 1.1 and 2.3, respectively. Higher supersaturation means higher melt undercooling which is the difference between the equilibrium melting temperature for the c_0 and the melt temperature. As Ω_0 increases, the morphologies are altered from a 4-fold symmetric dendrite to circular crystal with no anisotropy. With Ω_0=0.83 (Figure 5.10 (A)), four primary dendrite trunks grow along with the coordinate axes. Since we did not apply any induced noise at the interface, we do not see any side branch even until the steady state is achieved at the dendrite tip. The concentration field exhibits the solute pile-up in the liquid phase in front of the interface and the typical segregation pattern in the solid dendrite trunk (the lowest concentration along the center line of the trunk). The shape of the interface and the iso-concentration lines near the dendrite tip are close to a parabolic shape. For a larger initial supersaturation (Figure 5.10 (B) and (C)), the dendritic morphology is not observed. For Ω_0=1.1 (Figure 5.10 (B)), a few shallow cells appear along the crystallographic axes. For a higher Ω_0=2.3, it becomes close to a circular shape. In this non-dendritic structure, it is hard to see the concentration difference between both phases and any solute segregation in the solid phase (Figure 5.10 (C)). Only the small solute accumulation at the interface indicates the location of the interface. The calculations are done only in a quarter of the domain shown in Figure 5.10 and those are reflected about x- and y- axes. The domain sizes shown in the figures are 3.17 μm × 3.17 μm, 7.81 μm × 7.81 μm, and 2.11 μm × 2.11 μm, respectively, and those snapshots are taken at t=33.5 μsec, 22.0 μsec, and 0.737 μsec, respectively.

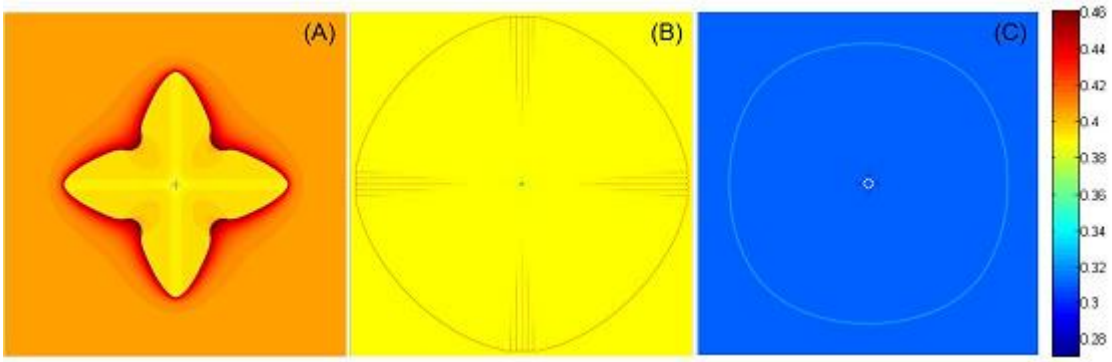

Figure 5.10 Calculated growing crystal morphologies of an ideal binary alloy with different initial supersaturations; color map indicates the concentration field. (A) c_0=0.40601. (B) c_0=0.388364. (C) c_0=0.310657.

5.2.3 Non-equilibrium chemical partitioning at the interface

Figure 5.11 plots the steady-state solute profiles near the interface along the coordinate axis, which is the crystallographic axis and also the center line of the dendrite, calculated with different initial concentrations. The calculated diffusion boundary layer thickness, δ_c, decreases with Ω_0 (i.e. increase with c_0). For very high Ω_0 (c_0=0.310657), δ_c becomes as small as the interface thickness, W.

Figure 5.12 shows the interface concentration measured from simulation results as a function of Ω_0. c_S^* (triangles) and c_L^* (squares) are identified by extrapolating the concentration fields in the bulk solid and liquid, respectively, to the position corresponding to ϕ=0. c_L^e and c_S^e are also indicated with dotted lines and circles, respectively, in Figure 5.12. All the values in Figure 5.12 are normalized by c_0, and thus the dashed line represents c_0. For lower Ω_0 (< 0.9), the c_S^* and c_L^* are close to the equilibrium values. This means the interface retains the local equilibrium condition. As Ω_0 increases, the interface concentrations gradually deviate from the equilibrium values, and c_S^* approaches c_0 due to the decrease of solute rejection. This behavior is analogous to that predicted using experimental data by Eckler *et al.*[40]. Figure 5.13 shows the measured k_V as a function of the steady state interface velocity. It is clearly seen that the k_V gradually increases with V* from the equilibrium value, k_e. This continuously increasing

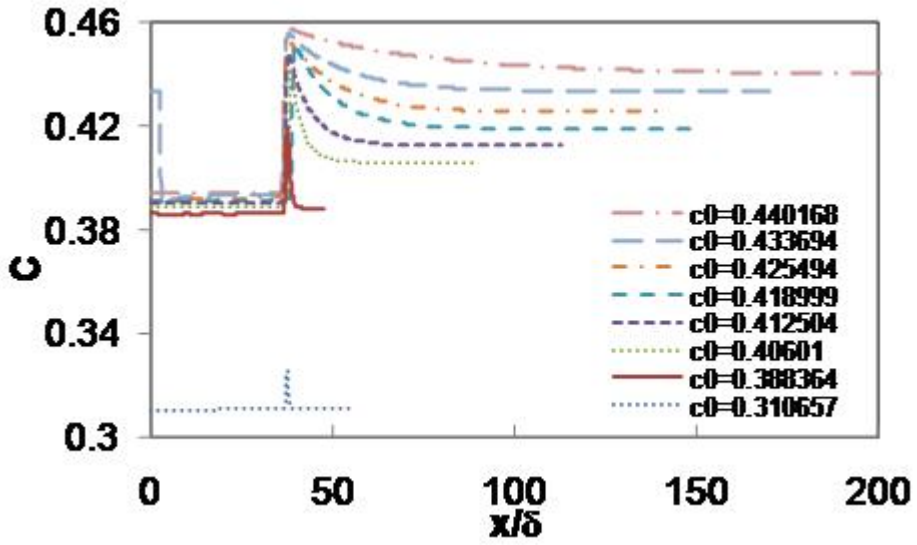

Figure 5.11 Interface concentrations field near the interface with different far-field concentrations, measured from current phase-field simulations.

k_V with V* is consistent with the Aziz's analysis (the dashed line) with V_D=0.5 m/s.

5.2.4 Selection of the interface velocity and curvature

Figure 5.14 shows the measured interface velocities, V*, and interface radius, R*, as a function of the initial supersaturation, Ω_0. Since the dendrite tip grows along the coordinate axis, as shown in Figure 5.10 (A) in most calculated morphologies, the interface velocities are calculated by tracking the position of ϕ=0 on the coordinate axis as a function of time during the simulation. In the case of cellular growth (Figure 5.10 (B)), the cell tip is not exactly on the coordinate axis, and we obtained the positions of the cell tip which is the closest one to the coordinate axis, at two different times. The cell tip velocity is considered the position difference divided by the time duration. R* is measured from the calculated crystal morphology by the parabolic fitting. As mentioned by Ramirez *et al.*, most analytical theories of dendritic growth are based on the parabolic assumption of the dendrite tip shape. Thus, it is reasonable to fit the simulated crystal morphology into the parabolic equation and to obtain the radius of curvature from the parabolically fitted equation. The method of fitting follows that of Ramirez

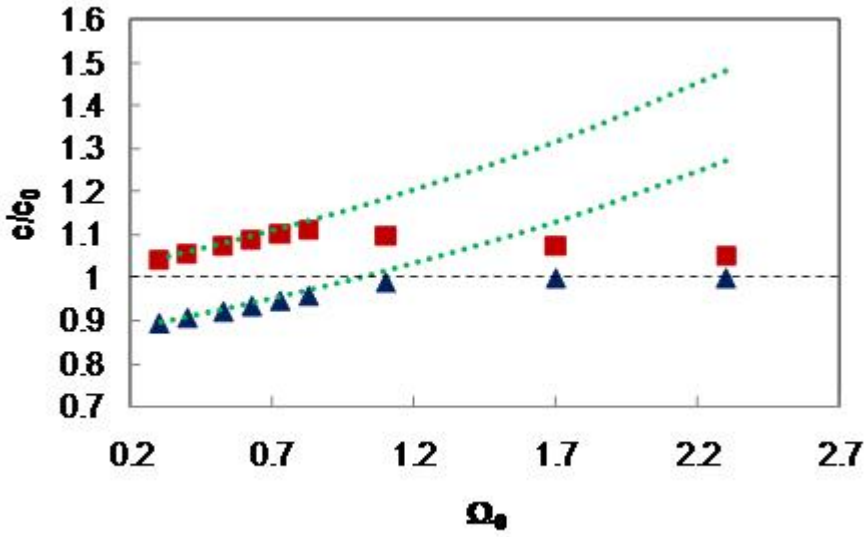

Figure 5.12 Normalized interface concentrations, c_L^* and c_S^* (squares and triangles, respectively) as a function of the initial supersaturations. The equilibrium concentrations for both phases are also shown as dotted lines.

et al.. After obtaining the interface position coordinates on the x-y plane, which corresponds to $\phi = 0$, those interface position coordinates are plotted on the $x^2 - y$ plane. The slope for a linear part of the $x^2 - y$ plot corresponds to the interface curvature, R^*. For $\Omega_0 > 1.5$, the growth morphology is almost circular (Figure 5.10 (c)). Thus, unlike steady state dendrites or cells, R* is continuously increasing and does not have a steady state value, while V* is constant. Thus, the tip radius for Ω_0=1.7 in Figure 5.14 (b) is the value at t=1.4 μsec and the R* would keep increasing after then.

In the Figure 5.14 (a), V* increases with Ω_0 in power law at $\Omega_0 < 0.9$, but at $\Omega_0 > 1$ V* shows linear dependency on Ω_0. R* also decreases with Ω_0 at $\Omega_0 < 0.9$, but increases at $\Omega_0 > 1$. This transition of growth behavior appears under the solidification condition where the non-equilibrium chemical partitioning starts to occur (Figure 5.12). With increasing V* with Ω_0, the non-equilibrium solute partitioning becomes significant with $0.9 < \Omega_0 < 1$, and the solute pile-up ahead of the solid-liquid interface lessens. This should lead to the transition from solute diffusion-controlled growth dynamics into kinetic-limited growth. This growth mode

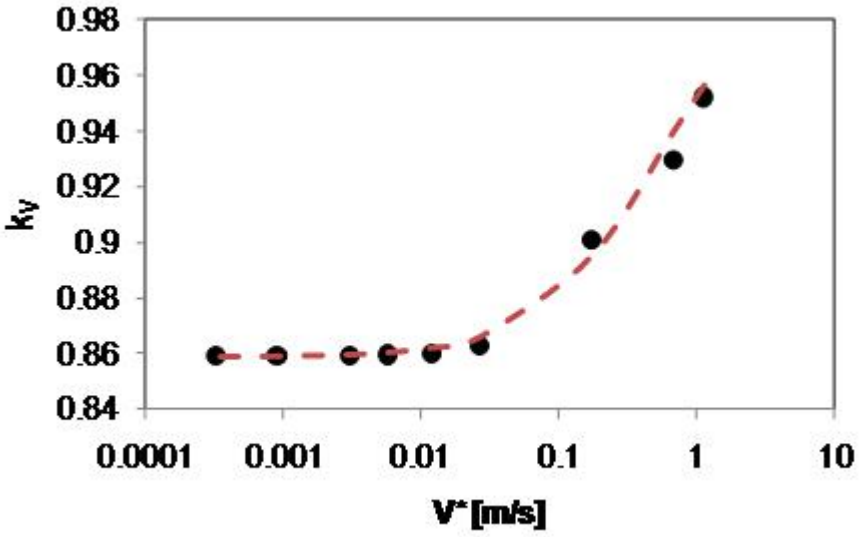

Figure 5.13 Measured interface partition coefficients as a function of the measured steady state tip velocities (dots). Aziz's solute trapping model (Eq. 2.14) with the atomic diffusive velocity, V_D, equal to 0.5 m/sec is consistent with the measured k_V.

change is consistent with experimental observations[40]. For more quantitative comparison with experimental results, calculations should incorporate heat transfer. With low growth rate, the thermal diffusive speed may be much faster than the growth rate and the thermal diffusion take little effect on the growth. But a higher growth rate may decrease the thermal boundary layer in front of the solid-liquid interface and this leads to the growth dynamics dominated by thermal diffusion.

The selection behavior of the dendrite tip velocity and the tip radius is in agreement with the Ivantsov function (Eq. 2.28). The Peclet numbers are obtained from the measured tip velocity and the tip radius ($P_C = R^*V^*/2D_L$). The measured tip supersaturation, $\Omega^*(= (c_L^* - c_0)/(c_L^* - c_S^*))$, is calculated with the interface concentrations at the steady state growth. For lower c_0, effective interface supersaturation, Ω^*, approaches unity because both c_L^* and c_S^* converge on c_0 due to the solute trapping phenomenon. The relationship of P_c and Ω^* shows a reasonably good agreement with the Ivantsov function (Figure 5.15).

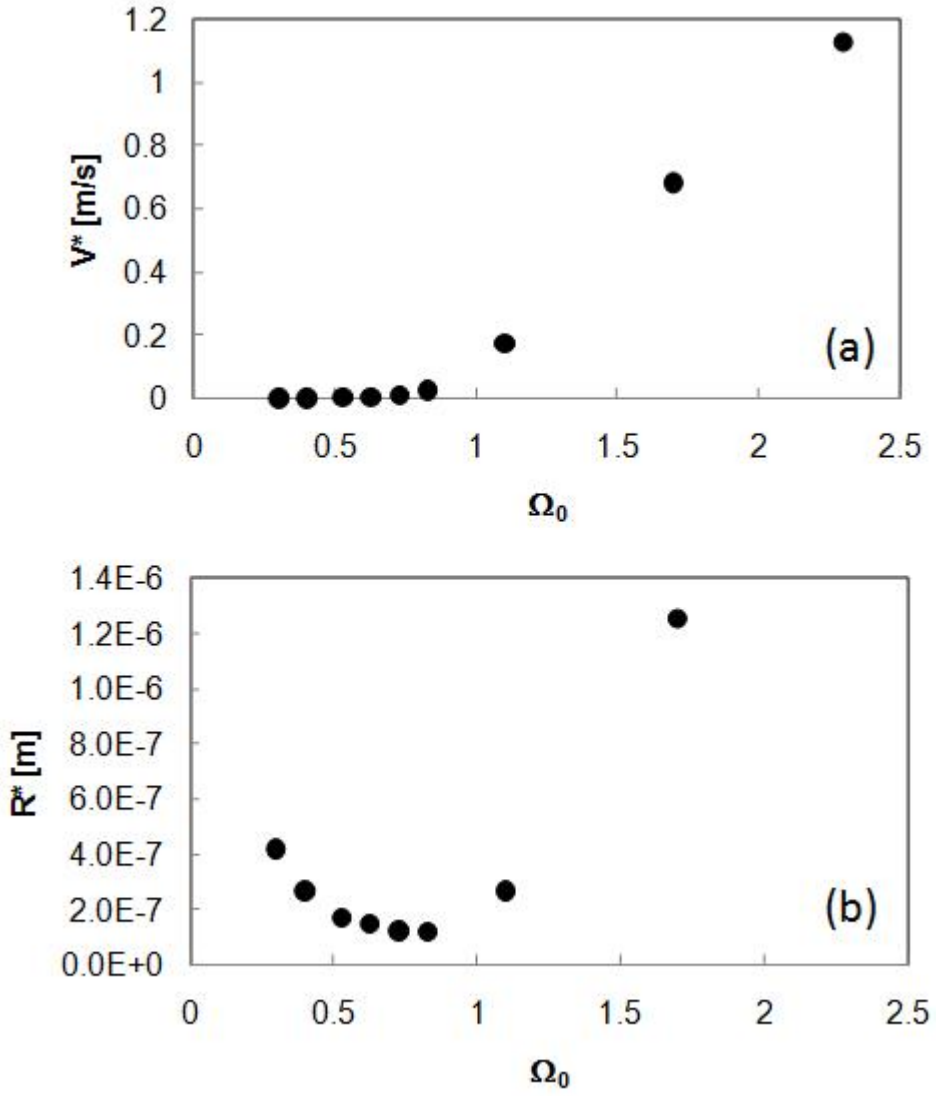

Figure 5.14 Measured interface velocities and tip radii with different initial supersaturations

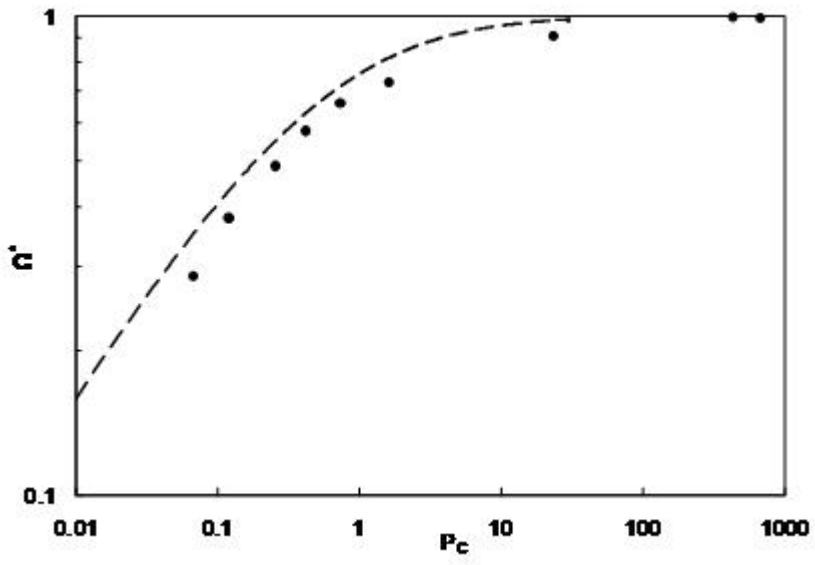

Figure 5.15 Comparison of the measured Peclet numbers (circles) and Ivantsov function (dashed curve).

5.2.5 Summary

- The isothermal morphology evolution in the growth of a binary alloy in an undercooled melt was computed by the phase-field model. The growth velocity and morphology selection in response of the highly driven growth condition and the non-equilibrium chemical partitioning have been shown. It has been shown that this calculation is capable of simulating appropriate interface kinetics and morphology evolution, regardless of the velocity regime or growth mode.

- The morphology transition has been shown with different melt undercoolings. The dendrite morphology changes into cells and circular shapes (planar growth) in turn with increasing initial supersaturations. This transition is consistent with the previous analytical models and phase-field calculations[88, 130].

- It could be observed that the solute partitioning at the solid-liquid interface strongly decrease as the growth velocity increases. The non-equilibrium solute partitioning behavior measured from calculation results is in good agreement with Aziz's solute trapping

model.

- It was possible to simulate the selection of morphologies, growth rates, and interface concentrations under both typical and highly driven growth conditions. With lower initial supersaturations, the calculated tip operating points are consistent with the classical solidification theories and the local equilibrium condition is retained. With higher supersaturations, the calculation successfully shows the characteristic transition into the kinetically driven growth regime. It could show that this phase-field simulation can properly capture the transition from equilibrium to non-equilibrium growth kinetics over wide range of undercoolings, involving the drastic change of the length and time scales of dynamic growth conditions

CHAPTER 6. GENERAL CONCLUSION

We have seen that the phase-field simulation is able to describe easily the interface dynamics in response to various solidification conditions, and it can be utilized to investigate the rapid growth dynamics for which experimental studies are difficult. In the current work, we demonstrated the dynamic response of the solid-liquid interface of alloys experiencing a rapid growth condition. The non-equilibrium chemical partitioning and the corresponding selection of interface dynamics was calculated by virtue of the diffused interface characteristics of the phase-field model.

In this work, transient planar interface dynamics in rapid directional solidification condition were addressed. We have shown that Warren-Langer's model cannot be applied to the rapid growth condition where the non-equilibrium chemical partitioning and the effect of atomic attachment kinetics become significant. *Through the phase-field simulation, we described the full transient interface dynamics associated with the non-equilibrium growth process.* The calculated steady state condition is in good agreement with the analytical description of the planar interface condition. The steady state interface temperature was found to depend on the pulling velocity.

During the transient growth dynamics, the instantaneous jump of interface velocity was shown. This phenomenon has been suggested in the previous interface stability analysis[77, 78] and phenomenological model[54], and confirmed in a numerical approach[80, 81]. It has been presumed that it might be triggered by the time-dependent oscillatory instability of the planar interface in a specific range of growth condition. Conti has successfully presented the periodic variations of the growth rate, but the results deviated with the previous theory and analysis. *By utilizing the thin-interface limit phase-field model with anti-trapping current and continually*

adjusting grid spacing in accordance with the effective interface thickness during growth process, the current simulation successfully presented the full transient oscillation dynamics which is in good agreement with the previous analysis.

The variation of interface concentrations during the fast transient growth dynamics were also shown, whereas the experimental measurement of these values is very challenging. *In the beginning of the transient dynamics, the interface retains the local equilibrium condition; but, at a critical interface undercooling, the chemical partitioning at the interface gradually deviates from the local equilibrium value.* The interface velocities respond dynamically to the variation of the interface chemical partitioning.

In addition to the transient planar front dynamics, steady state morphology selection associated with the non-equilibrium interface dynamics also has been demonstrated through the phase-field calculation. These calculation results correctly described the transition from equilibrium to non-equilibrium growth selection as a function of the initial supersaturation of the melt. By increasing the initial supersaturation of the isothermal system, the morphology was changed from dendrites/cells to planar fronts. Under a growth condition, the transition in the velocity-undercooling behavior was shown. During these transitions of morphologies and the velocity-undercooling behavior, the measured interface concentrations showed that the non-equilibrium chemical partitioning begins. By comparing the results with the Ivantsov's analytical growth theory, the measured operating points of the growing crystals were verified.

Our simulation showed the time-dependent interface dynamics which are selected by the comprehensive correlation between the non-equilibrium chemical partitioning, the selections of the interface velocity and morphology, and the effect of the atomic attachment kinetics. We should note that the phase-field calculation allows the prediction of rapid growth dynamics without any prescribed solidification theories. In the calculation, the dynamics were selected only by the competitions between length scales and times scales of various physical properties during the dissipation process of the solidification driving force. This process is very close in nature to the fundamental mechanism of alloy solidification.

The current work concerned the transient planar growth dynamics in directional solidifi-

cation and the steady state morphology in undercooled melts. Realistically, in most of the growth conditions where the local equilibrium retains during the transient dynamics, the planar interface is not stable and it tends to evolve complex morphologies. And in the rapid growth condition, the diffusive length of the heat can be compatible with the length scale of the growing crystal. In that case, the thermal boundary layer ahead of the solid-liquid interface may significantly affect the growth dynamics and cannot be ignored. For more rigorous study of the rapid growth dynamics of alloys, therefore, the phase-field investigation of transient interface growth dynamics of alloys in two-dimensional directional solidification system would be suggested including the competition between the chemical and heat diffusion process.

APPENDIX A. THE CODES

Here are the codes used to compute the main results of the current thesis work.

One-dimensional directional growth calculation

```
////////////////////////////////////////////////////////////////////////
////        Phase-field simulation                                  ////
////        1D planar growth of regular binary alloys               ////
////        constant temperature gradient condition                 ////
////        moving frame                                            ////
////        no solid diffusion                                      ////
////--------------------------------------------------------------------////
////        Thin-interface limit model                              ////
////        Anti-trapping current                                   ////
////        Noise on the phase-field                                ////
////        based on Tong, Greenwood, Haataja, and Provatas (2008,PRB)  ////
////        Last updated : 2/3/2010 by Jeong Yun Choi               ////
////////////////////////////////////////////////////////////////////////

#include <iostream>
#include <time.h>
#include <iomanip>
#include <stdlib.h>
#include <fstream>
#include <cmath>

using namespace std;

const double R=8.3144; //the gas constant

unsigned long ii,iip; //current and previous grid point at the interface
double *x,*T,*c,*cp,*phi,*php,*U,*Up;

FILE *phase1,*phase2,*phase3,*phase4,*phase5,*conc1,*conc2,*conc3,*conc4,*conc5,
    *parameters,*df,*T1,*T2,*T3,*T4,*T5,*V,*phase,*conc,*TT,*Xaxis,*Xaxis1,*Xaxis2,
```

```
    *Xaxis3,*Xaxis4,*Xaxis5;

double clE(double T0);
double csE(double T0);
void diff(unsigned long nts,unsigned long L,double dt,double dx,double Dl,double vm,
    double c0,double LA,double LB,double TmA,double TmB,double lambda,double Gamma,
    double a1,double a2);
void moving(unsigned long L,unsigned long nts,double dt,double G,double dx,double c0,
    double TmA);
void start(unsigned long L,double c0,double T0,double dx,double G,double TmA);
    double timestep(double Dl,double S,double dx,double tau,double W,double k);
    double Tl(double c),Ts(double c);
void ugrid(unsigned long L,double dx);
void temp(unsigned long L,double Tdot,double dt,double TmA,double nts);

////////////////////////////////////////////////////////////////////////////
////            main function                                           ////
////////////////////////////////////////////////////////////////////////////
int main()
{
    unsigned long seconds,L,i;
    unsigned int hours=0,minutes=0,mins_left=0,secs_left=0;
    time_t time1,time2; // start-calculation time, end-calculation time
    time(&time1);

    double dx,dt,t_growth; // grid spacing (input value) (m), timestep, total time of the growth
    double Dl; // solute diffusivity in liquid (input value) (m2/s)
    double c0,cmax; // initial composition in liquid (input value) (atomic fraction), maximum
                    concentration
    double T0; // initial temperature at the first grid point (input value) (K)
    double TmA,TmB; // melting temperature of solvent and solute (input value) (K)
    double vm; // molar volume of alloy (input value) (m3/mol)
    double sigA,sigB; // interface energy of solvent and solute (input value) (J/m2)
    double S; // FDM stability parameter
    double LA,LB; // latent heat (J/m3)
    unsigned long iout; // output interval
    unsigned long ntsl,nts,nts0; // total number of time steps (input value)
    double *te;
    double tau,a2,lambda,W,d0,a1,Gamma,DT,k,csEQ,clEQ,G,Tdot,xii;

    phase1=fopen("phase1.dat","w");
    phase2=fopen("phase2.dat","w");
    phase3=fopen("phase3.dat","w");
    phase4=fopen("phase4.dat","w");
    phase5=fopen("phase5.dat","w");
    conc1=fopen("conc1.dat","w");
```

```
conc2=fopen("conc2.dat","w");
conc3=fopen("conc3.dat","w");
conc4=fopen("conc4.dat","w");
conc5=fopen("conc5.dat","w");
phase=fopen("phase.dat","w");
T1=fopen("T1.dat","w");
T2=fopen("T2.dat","w");
T3=fopen("T3.dat","w");
T4=fopen("T4.dat","w");
T5=fopen("T5.dat","w");
TT=fopen("TT.dat","w");
conc=fopen("conc.dat","w");
parameters=fopen("parameters.dat","w");
df=fopen("datainput.dat","r");
V=fopen("V.dat","w");
Xaxis=fopen("Xaxis.dat","w");
Xaxis1=fopen("Xaxis1.dat","w");
Xaxis2=fopen("Xaxis2.dat","w");
Xaxis3=fopen("Xaxis3.dat","w");
Xaxis4=fopen("Xaxis4.dat","w");
Xaxis5=fopen("Xaxis5.dat","w");

if(df==NULL){
    cout<<"\nError opening datainput.dat!"<<endl;
    return 0;
};

fscanf(df,"%lu %lf %lf %lf %lf %lf %lf %lf %lf %lu %lu %lf %lf %lf %lf %lu %lf %lf %lf %lf
    %lf %lf %lf",&L,&TmA,&TmB,&LA,&LB,&sigA,&sigB,&vm,&Dl,&nts0 ,&ntsl,&T0,
    &c0,&S,&iout,&a1,&a2,&lambda,&G,&Tdot,&dx,&t_growth);
cout<<"\nL:"<<L<<"\nTmA:"<<TmA<<"\nTmB:"<<TmB<<"\nLA:"<<LA<<"\
    nLB:"<<LB<<"\nsigA:"<<sigA<<"\nsigB:"<<sigB<<"\nvm:"<<vm<<"\nDl:"
    <<Dl<<"\nnts0:"<<nts0<<"\nntsl:"<<ntsl<<"\nc0:"<<c0<<"\nT0:"<<T0<<"
    \nS:"<<S<<"\niout: "<<iout<<"\na1:"<<a1 <<"\na2:"<<a2<<"\nlambda:"<<
    lambda<<"\nG:"<<G<<"\nTdot:"<<Tdot<<"\ndx:"<<dx<<"\nt_growth:"<<
    t_growth<<endl;

fprintf(parameters,"////////////////////////////////////////////////////////////
    ///\n");
fprintf(parameters,"////          Phase-field simulation                        /
    ///\n");
fprintf(parameters,"////          1D planar growth of binary alloys             /
    ///\n");
fprintf(parameters,"////          constant temperature gradient condition       /
    ///\n");
fprintf(parameters,"////          moving frame                                  /
```

```
    ///\n");
fprintf(parameters,"////          no solid diffusion                                    /
    ///\n");
fprintf(parameters,"////----------------------------------------------------------------/
    ///\n");
fprintf(parameters,"////          Thin-interface limit model                            /
    ///\n");
fprintf(parameters,"////          Anti-trapping current                                 /
    ///\n");
fprintf(parameters,"////          Noise on the phase-field                              /
    ///\n");
fprintf(parameters,"////          based on Tong,Greenwood,and Provatas (2008,PRB)       /
    ///\n");
fprintf(parameters,"////          1DDS_2_3_10.cpp                                       /
    ///\n");
fprintf(parameters,"////          Last updated : 2/3/2010 by Jeong Yun Choi             /
    ///\n");
fprintf(parameters,"////////////////////////////////////////////////////////
    ///////\n\n\n\n");
fprintf(parameters,"////INPUT PARAMETERS\n\n");
fprintf(parameters,"Total number of grid points (L):\t%lu\n",L);
fprintf(parameters,"Melting temperature of the solvent element (TmA) [K]:\t%G\n",TmA)
    ;
fprintf(parameters,"Melting temperature of the solute element (TmB) [K]:\t%G\n",TmB);
fprintf(parameters,"Latent heat of the solvent element (LA) [J/m3]:\t%G\n",LA);
fprintf(parameters,"Latent heat of the solute element (LB) [J/m3]:\t%G\n",LB);
fprintf(parameters,"Solid/liquid interfacial energy of the solvent element (sigA) [J/m2]:
    %G\n",sigA);
fprintf(parameters,"Solid/liquid interfacial energy of the solute element (sigB) [J/m2]:
    %G\n",sigB);
fprintf(parameters,"Average molar volume (vm) [m3/mol]:\t%G\n",vm);
fprintf(parameters,"Diffusion coefficient of the liquid phase (Dl) [m2/sec]:\t%G\n",Dl);
fprintf(parameters,"Initial temperature at the interface (T0) [K]:\t%G\n",T0);
fprintf(parameters,"Initial composition (c0) [atomic fraction]:\t%G\n",c0);
fprintf(parameters,"FDM stability parameter (S):\t%G\n",S);
fprintf(parameters,"Initial time steps to calculate (nts0):\t%lu\n",nts0);
fprintf(parameters,"Input final time steps to calculate (ntsl):\t%lu\n",ntsl);
fprintf(parameters,"a1 :\t%G\n",a1);
fprintf(parameters,"a2 :\t%G\n",a2);
fprintf(parameters,"lambda :\t%G\n",lambda);
fprintf(parameters,"Frozen Temperature Gradient (G):\t%G\n",G);
fprintf(parameters,"Constant Cooling Rate (Tdot):\t%G\n",Tdot);
fprintf(parameters,"Initial time:\t%G\n",t_growth);

x=(double *)malloc((L+1)*sizeof(double));
if(x==NULL){
```

```
    cout<<"Out of Memory"<<endl;
    exit(0);
};

T=(double *)malloc((L+1)*sizeof(double));
if(T==NULL){
    cout<<"Out of Memory"<<endl;
    exit(0);
};

c=(double *)malloc((L+2)*sizeof(double));
if(c==NULL){
    cout<<"Out of Memory"<<endl;
    exit(0);
};

cp=(double *)malloc((L+2)*sizeof(double));
if(cp==NULL){
    cout<<"Out of Memory"<<endl;
    exit(0);
};

phi=(double *)malloc((L+2)*sizeof(double));
if(phi==NULL){
    cout<<"Out of Memory"<<endl;
    exit(0);
};

phip=(double *)malloc((L+2)*sizeof(double));
if(phip==NULL){
    cout<<"Out of Memory"<<endl;
    exit(0);
};

U=(double *)malloc((L+2)*sizeof(double));
if(U==NULL){
    cout<<"Out of Memory"<<endl;
    exit(0);
};

Up=(double *)malloc((L+2)*sizeof(double));
if(Up==NULL){
    cout<<"Out of Memory"<<endl;
    exit(0);
};
```

```
Gamma=sigA*TmA/LA;
csEQ=csE(T0);
clEQ=clE(T0);
k=csEQ/clEQ;
if(T0>TmA || clEQ<=0. || csEQ<=0. || csEQ>clEQ || k>1.-1.e-12) k=1.-1.e-12;

DT=Tl(c0)-T0;
d0=Gamma/DT;
W=lambda*d0/a1;
tau=a2*lambda/Dl*pow(W,2.);

fprintf(parameters,"Gibbs-Thomson coefficient (Gamma)[Km]:\t%G\n",Gamma);
fprintf(parameters,"Equilibrium solidus concentration (csEQ)[at.%]:\t%G\n",csEQ);
fprintf(parameters,"Equilibrium liquidus concentration (clEQ)[at.%]:\t%G\n",clEQ);
fprintf(parameters,"Equilibrium partition coefficient (k):\t%G\n",k);
fprintf(parameters,"Solidification temperature range (DT)[K]:\t%G\n",DT);
fprintf(parameters,"solutal capillary length (d0)[m]:\t%G\n",d0);
fprintf(parameters,"Interface width (W)[m]:\t%G\n",W);
fprintf(parameters,"Interface kinetic attachment time (tau)[sec]:\t%G\n",tau);
fprintf(parameters,"Grid spacing (dx) [m]:\t%G\n",dx);

start(L,c0,T0,dx,G,TmA); // set the initial condition
dt=timestep(Dl,S,dx,tau,W,k); // calculate dt

for(nts=nts0;nts<=ntsl;nts++){
    temp(L,Tdot,dt,TmA,nts);
    diff(nts,L,dt,dx,Dl,vm,c0,LA,LB,TmA,TmB,lambda,Gamma,a1,a2);
    if(ii!=iip){
        xii=((0.-phi[ii])*dx+(phi[ii]-phi[ii-1])*x[ii])/(phi[ii]-phi[ii-1]);
        cmax=0.;
        for(i=1;i<L;i++) cmax=max(cmax,max(c[i],c[i+1]));
        fprintf(V,"%E\t%E\t%lf\t%lf\t%lf\n",t_growth+dt*(nts-(nts0-1)),xii,T[ii]-G*(x[ii]-
            xii),c[1],cmax);
        if(ii!=iip && nts!=ntsl) moving(L,nts,dt,G,dx,c0,TmA);
    };
    if(!(nts%iout)){
        if((L%2)==1) cout<<nts<<"/"<<ntsl<<"\tt="<<t_growth+dt*(nts-(nts0-1))
            <<"\n\tii="<<ii<<"\tphi[1]="<<phi[1]<<"\n\tc[L]="<<c[L] <<"\tphi[L]=
            "<<phi[L]<<"\n\tT["<<ii<<"]="<<T[ii]<<"\tx["<<ii<<"]="<<x[ii]<<"\t
                c[1]="<<c[1]<<endl;
        else cout<<nts<<"/"<<ntsl<<"\tt="<<t_growth+dt*(nts-(nts0-1))<<"\n\tii="
            <<ii<<"\tphi[1]="<<phi[1]<<"\n\tc[L-1]="<<c[L-1]<<"\tphi[L-1]="<<
            phi[L-1]<<"\n\tT["<<ii<<"]="<<T[ii]<<"\tx["<<ii<<"]="<<x[ii]<<"\
            tc[1]="<<c[1]<<endl;
    };
```

```
if(ii>=L-1){
    cout<<"ii="<<ii<<endl;
    nts++;
    te=phip,phip=phi,phi=te;
    te=cp,cp=c,c=te;
    break;
}
else if(x[ii]<0.){
    cout<<"x[ii]="<<x[ii]<<endl;nts++;te=phip,phip=phi,phi=te;te=cp,cp=c,c=te;
    break;
}
else if(c[L]>c0+5.e-7){
    cout<<"c[L]="<<c[L]<<endl;nts++;te=phip,phip=phi,phi=te;te=cp,cp=c,c=te;
    break;
};

if(nts<=ntsl/5 && nts+1>ntsl/5){
    for(i=1;i<=L;i++){
        fprintf(T1,"%lf\n",T[i]);
        fprintf(Xaxis1,"%E\n",x[i]);
        fprintf(phase1,"%lf\n",phi[i]);
        fprintf(conc1,"%lf\n",c[i]);
    };
    fclose(phase1);fclose(conc1);fclose(T1);fclose(Xaxis1);
}
else if(nts>ntsl/5){
    if(nts<=ntsl*2/5 && nts+1>ntsl*2/5){
        for(i=1;i<=L;i++){
            fprintf(T2,"%lf\n",T[i]);
            fprintf(Xaxis2,"%E\n",x[i]);
            fprintf(phase2,"%lf\n",phi[i]);
            fprintf(conc2,"%lf\n",c[i]);
        };
        fclose(phase2);fclose(conc2);fclose(T2);fclose(Xaxis2);
    }
    else if(nts>ntsl*2/5){
        if(nts<=ntsl*3/5 && nts+1>ntsl*3/5){
            for(i=1;i<=L;i++){
                fprintf(T3,"%lf\n",T[i]);
                fprintf(Xaxis3,"%E\n",x[i]);
                fprintf(phase3,"%lf\n",phi[i]);
                fprintf(conc3,"%lf\n",c[i]);
            };
            fclose(phase3);fclose(conc3);fclose(T3);fclose(Xaxis3);
        }
        else if(nts>ntsl*3/5){
```

```
                if(nts<=ntsl*4/5 && nts+1>ntsl*4/5){
                    for(i=1;i<=L;i++){
                        fprintf(T4,"%lf\n",T[i]);
                        fprintf(Xaxis4,"%E\n",x[i]);
                        fprintf(phase4,"%lf\n",phi[i]);
                        fprintf(conc4,"%lf\n",c[i]);
                    };
                    fclose(phase4);fclose(conc4);fclose(T4);fclose(Xaxis4);
                };
            };
        };
    };
    iip=ii;ii=0;
    te=phip,phip=phi,phi=te;
    te=cp,cp=c,c=te;
    te=Up,Up=U,U=te;
};

cout<<"total number of time step="<<nts-1<<"\n";
fprintf(parameters,"total number of time step=%lu\n",nts-1);
fprintf(parameters,"total time of growth =%E\n",t_growth+dt*(nts-(nts0-1)-1));

for(i=1;i<=L;i++){
    fprintf(phase5,"%lf\n",phip[i]);
    fprintf(conc5,"%lf\n",cp[i]);
    fprintf(Xaxis5,"%E\n",x[i]);
    fprintf(T5,"%lf\n",T[i]);
};

time(&time2);
seconds=(unsigned long)difftime(time2,time1);
minutes=seconds/60;
secs_left=seconds%60;
hours=minutes/60;
mins_left=minutes%60;
cout<<"total CPU time="<<hours<<" h "<<mins_left<<" m "<<secs_left<<" s\n";
fprintf(parameters,"total CPU time=%u h %u m %u s\n",hours,mins_left,secs_left);

fclose(phase);fclose(phase5);
fclose(conc);fclose(conc5);fclose(T5);fclose(TT);
fclose(parameters);fclose(df);fclose(V);fclose(Xaxis);fclose(Xaxis5);

free(x);free(T);free(phi);free(phip);free(c);free(cp);free(U);free(Up);

return 0;
}
```

```
double clE(double T0)
{
    //******** best fit of phase diagram of Ni-Cu binary alloy********//
    double clE=0.008085*pow((T0-1545.)/110.9,4.)+0.002123*pow((T0-1545.)/110.9,3.)
       -0.06596*pow((T0-1545.)/110.9,2.)-0.3076*(T0-1545.)/110.9+0.6184;
    if(clE>1.) return(1.);
    else return(clE);
}

double csE(double T0)
{
    //******** best fit of phase diagram of Ni-Cu binary alloy ********//
    double csE=-0.006093*pow((T0-1545.)/110.9,4.)+0.002782*pow((T0-1545.)/110.9,3.)
       +0.02402*pow((T0-1545.)/110.9,2.)-0.3075*(T0-1545.)/110.9+0.4739;
    if(csE>1.) return(1.);
    else return(csE);
}

void diff(unsigned long nts,unsigned long L,double dt,double dx,double Dl,double vm,double
    c0,double LA,double LB,double TmA,double TmB,double lambda,double Gamma,double
    a1,double a2)
{
    unsigned long i;
    double GE,GW;
    double phipP,phipE,phipW,phiP,phiE,phiW,UpP,UpE,UpW;
    double tau,W,DT,d0;
    double k,clEQ,csEQ;
    for(i=1;i<=L;i++){
       if(i<=iip+100){
          phipP=phip[i];
          phipE=phip[i+1];
          phipW=phip[i-1];
          UpP=Up[i];

          if(i==1)phipW=phipE;
          else if(i==L)phipE=phipW;

          DT=Tl(c0)-T[iip];
          d0=Gamma/DT;
          W=lambda*d0/a1;
          tau=a2*lambda/Dl*pow(W,2.);

          phi[i]=phipP+dt/tau*(phipP-pow(phipP,3.)-lambda*pow(1.-pow(phipP,2.),2.)*UpP
             +pow(W/dx,2.)*(phipE-2.*phipP+phipW));
          if(phi[i]>1.)phi[i]=1.;
          else if(phi[i]<-1.)phi[i]=-1.;
```

```
        if(i>ii && phi[i]<=0. && phi[i-1]>=0.) ii=i;
    }
    else phi[i]=-1.;
};

for(i=1;i<=L;i++){
    UpP=Up[i];
    UpE=Up[i+1];
    UpW=Up[i-1];
    phipP=phip[i];
    phipE=phip[i+1];
    phipW=phip[i-1];
    phiP=phi[i];
    phiE=phi[i+1];
    phiW=phi[i-1];

    if(i==1){
        UpW=UpP-UpE+UpP;
        phipW=phipE;
        phiW=phiE;
    }
    else if(i==L){
        UpE=UpP+UpP-UpW;
        phipE=phipW;
        phiE=phiW;
    };

    if(abs(phipE-phipP)<1.e-10) GE=0.;
    else if((phipE-phipP)>0.) GE=1.;
    else GE=-1.;

    if(abs(phipW-phipP)<1.e-10) GW=0.;
    else if((phipP-phipW)>0.) GW=1.;
    else GW=-1.;

    csEQ=csE(T[i]);
    clEQ=clE(T[i]);
    if(csEQ>1.) csEQ=1.;
    if(clEQ>1.) clEQ=1.;
    k=csEQ/clEQ;
    if(T[i]>TmA || clEQ<=0. || csEQ<=0. || csEQ>clEQ || k>1.-1.e-12) k=1.-1.e-12;

    DT=Tl(c0)-T[iip];
    d0=Gamma/DT;
    W=lambda*d0/a1;
```

```
        U[i]=UpP+(1.+(1.-k)*UpP)/(1.+k-(1.-k)*phipP)*(phiP-phipP)
            +1./(2.*dx*(1.+k-(1.-k)*phipP))*(Dl*dt/dx*((2.-phipE-phipP)*(UpE-UpP)
            -(2.-phipP-phipW)*(UpP-UpW))+W/sqrt(2.)*(((1.+(1.-k)*UpE)*(phiE-phipE)
            +(1.+(1.-k)*UpP)*(phiP-phipP))*GE-((1.+(1.-k)*UpP)*(phiP-phipP)
            +(1.+(1.-k)*UpW)*(phiW-phipW))*GW));
        c[i]=clEQ/2.*(U[i]*(1.-k)+1.)*(1.+k-(1.-k)*phiP);
        if(T[i]>TmA || clEQ<=0. || csEQ<=0. || k>=1.-1.e-12) {
            c[i]=cp[i];U[i]=(2.*c[i]/clEQ/(1.+k-(1.-k)*phi[i])-1.)/(1.-k);};
    };
}

void moving(unsigned long L,unsigned long nts,double dt,double G,double dx,double c0,double
    TmA)
{
    unsigned long i;
    short s;
    double clEQ,csEQ,k;

    s=short(ii)-short(iip);
    if(s>0){
        for(i=1;i<=L-s;i++){
            x[i]=x[i+s];
            T[i]=T[i+s];
            phi[i]=phi[i+s];
            U[i]=U[i+s];
            c[i]=c[i+s];
        };
        for(i=L-s+1;i<=L;i++){
            x[i]=x[i-1]+dx;
            T[i]=T[i-1]+G*dx;
            csEQ=csE(T[i]);
            clEQ=clE(T[i]);
            k=csEQ/clEQ;
            if(T[i]>TmA || clEQ<=0. || csEQ<=0. || csEQ>clEQ || k>1.-1.e-12) k=1.-1.e-12;
            phi[i]=-1.;
            U[i]=(2.*c0/clEQ/(1.+k-(1.-k)*(-1.))-1.)/(1.-k);
            c[i]=c0;
        };
        ii-=s;
        iip-=s;
    }
    else {
        for(i=L;i>=(unsigned long)(1-s);i- -){
            x[i]=x[i+s];
            T[i]=T[i+s];
            phi[i]=phi[i+s];
```

```
            U[i]=U[i+s];
            c[i]=c[i+s];
        };
        for(i=-s;i>=1;i- -){
            x[i]=x[i+1]-dx;
            T[i]=T[i+1]-G*dx;
            c[i]=c[i+1];
            csEQ=csE(T[i]);
            clEQ=clE(T[i]);
            k=csEQ/clEQ;
            if(T[i]>TmA || clEQ<=0. || csEQ<=0. || csEQ>clEQ || k>1.-1.e-12) k=1.-1.e-12;
            phi[i]=1.;
            U[i]=(2.*c[i]/clEQ/(1.+k-(1.-k)*(-1.))-1.)/(1.-k);
        };
        ii-=s;
        iip-=s;
    };
}

void start(unsigned long L,double c0,double T0,double dx,double G,double TmA)
{
    //initial condition setting//
    unsigned long i;

    for(i=1;i<=L;i++){
        T[i]=T0-G*350.*dx+G*(i-1)*dx;
        cp[i]=c0;
        if(i<350){
            phip[i]=1.;
            cp[i]=(csE(T[i])<c0)?csE(T[i]):c0;
        }
        else phip[i]=-1.;

        iip=350;
    };

    ugrid(L,dx); // set the positions of grid points

/****** To continue the calculation after a stop of the previous calculation ******/
/*
    ifstream phiin,cin,Tin,Xin;

    phiin.open("phase_ini.dat");
    cin.open("c_ini.dat");
    Tin.open("T_ini.dat");
    Xin.open("X_ini.dat");
```

```
    for(i=1;i<=L;i++){
//    if(i>120600){
//        T[i]=T[i-1]+G*dx;
//        x[i]=x[i-1]+dx;
//        phip[i]=-1.;
//        cp[i]=c0;
//    }
//    else{
            if(i==1) Tin>>T[i];
            else T[i]=T[i-1]+G*dx;
            Xin>>x[i];
            phiin>>phip[i];
            cin>>cp[i];
//    };
    };
    iip=115800;
*/

/****** Translating the interface position ******/
/* for(i=1;i<=L;i++){
        if(i<=119000){
            T[i]=T[i+1000];
            x[i]=x[i+1000];
            phip[i]=phip[i+1000];
            cp[i]=cp[i+1000];
        }
        else {
            T[i]=T[i-1]+G*dx;
            x[i]=x[i-1]+dx;
            phip[i]=-1.;
            cp[i]=cp[i-1];
        };
    };
*/

/****** Dividing meshes ******/
/* for(i=1;i<=L;i+=2){
        if(i>6000){
            T[i]=T[i-2]+G*dx*2.;
            x[i]=x[i-2]+dx*2.;
            phip[i]=-1.;
            cp[i]=c0;
        }
        else{
            Tin>>T[i];
            Xin>>x[i];
```

```
            phiin>>phip[i];
            cin>>cp[i];
        };
    };
    for(i=2;i<=L;i+=2){
        if(i==L){
            T[i]=T[i-1];
            x[i]=x[i-1];
            phip[i]=phip[i-1];
            cp[i]=cp[i-1];
        }
        else{
            T[i]=(T[i+1]+T[i-1])/2.;
            x[i]=(x[i+1]+x[i-1])/2.;
            phip[i]=(phip[i+1]+phip[i-1])/2.;
            cp[i]=(cp[i+1]+cp[i-1])/2.;
        };
    };
    iip=600;
*/
/*
    phiin.close();
    cin.close();
    Tin.close();
    Xin.close();
*/

// ugrid(L,dx); // set the positions of grid points
}

void temp(unsigned long L,double Tdot,double dt,double TmA,double nts)
{
    unsigned long i;
    double csEQ,clEQ,k;

    for(i=1;i<=L;i++){
        T[i]-=Tdot*dt;
        csEQ=csE(T[i]);
        clEQ=clE(T[i]);
        k=csEQ/clEQ;
        if(T[i]>TmA || clEQ<=0. || csEQ<=0. || csEQ>clEQ || k>1.-1.e-12) k=1.-1.e-12;
        else Up[i]=(2.*cp[i]/clEQ/(1.+k-(1.-k)*phip[i])-1.)/(1.-k);
    };
}

double timestep(double Dl,double S,double dx,double tau,double W,double k)
```

```
{
    double dt=(Dl>pow(W,2.)/tau)?S*dx*dx/Dl:S*dx*dx/(pow(W,2.)/tau);

    fprintf(parameters,"time step=%E\n",dt);
    cout<<"time step="<<dt<<"\n";

    return(dt);
}

double Tl(double c)
{
    //******** best fit of phase diagram of Ni-Cu binary alloy ********//
    return(-210.7*pow(c,3.)+146.3*pow(c,2.)-307.*c+1728.);
}

double Ts(double c)
{
    //********** best fit of phase diagram of Ni-Cu binary alloy **********//
    return(-261.*pow(c,4.)+471.8*pow(c,3.)-222.4*pow(c,2.)-359.*c+1728.);
}

void ugrid(unsigned long L,double dx)
{
    //generating uniform grids

    unsigned long i;

    x[1]=0.;

    for(i=2;i<=L;i++)
        x[i]=x[i-1]+dx;

    fprintf(parameters,"dx=%E\n",dx);

}
```

Two-dimensional calculation for equiaxed growth into an undercooled melt

```
////////////////////////////////////////////////////////////////
////          Phase-field simulation                        ////
////          2D dendritic growth of regular binary alloys   ////
////          under an isothermal condition                 ////
////          epsilon_4                                     ////
////          no solid diffusion                            ////
////          simple adaptive grid                           ////
```

```
////-------------------------------------------------------------////
////          Thin-interface limit model                         ////
////          Anti-trapping current                              ////
////          based on Tong, Greenwood, and Provatas (2008,PRB)  ////
////          TIL_ATC.cpp                                        ////
////          Last updated : 10/8/2009 by Jeong Yun Choi         ////
//////////////////////////////////////////////////////////////////

#include <iostream>
#include <time.h>
#include <iomanip>
#include <stdlib.h>
#include <fstream>
#include <cmath>

using namespace std;

const double R=8.3144;

unsigned long ii,iip,jj,jjp,gb,gbp;
double *x,*y,**c,**cp,**phi,**phip,**U,**Up;

FILE *phase1,*phase2,*phase3,*phase4,*phase5,*conc1,*conc2,*conc3,*conc4,*conc5,
    *parameters,*V,*df,*rho,*phase,*conc,*Yaxis,*Xaxis;

double clE(double T0);
double csE(double T0);
void diff(unsigned long nts,unsigned long L,unsigned long M,double dt,double dx,double Dl,
    double vm,double c0,double T0,double fluc ,double LA,double LB,double TmA,double
TmB,
    double eps4,double tau,double lambda,double k,double W,double clEQ);
void moving(unsigned long L,unsigned long nts,double dt,double G,double dx,double c0,double
    *x,double *c,double *cp,double *T,double *phi, double *phip,unsigned long ii);
void start(unsigned long L,unsigned long M,double c0,double dx,double clEQ,double k);
void radius(double dx,double dt,unsigned long nts);
double timestep(double Dl,double S,double dx,double tau,double W,double k);
double Tl(double c);
void ugrid(unsigned long L,unsigned long M,double dx);

//////////////////////////////////////////////////////////////////////////
////          main function                                          ////
//////////////////////////////////////////////////////////////////////////
int main()
{
    unsigned long seconds,L,M,i,j;
    unsigned int hours=0,minutes=0,mins_left=0,secs_left=0;
```

```
time_t time1,time2;
time(&time1); //starting time

double dx,dt; // grid spacing (input value) (m)
double Dl; // solute diffusivity in liquid (input value) (m2/s)
double c0; // initial composition in liquid (input value) (atomic fraction)
double T0; // initial temperature at the first grid point (input value) (K)
double TmA,TmB; // melting temperature of solvent and solute (input value) (K)
double vm; // molar volume of alloy (input value) (m3/mol)
double sigA,sigB; // interface energy of solvent and solute (input value) (J/m2)
double S; // FDM stability parameter
double LA,LB; // latent heat (J/m3)
double eps4,fluc;
unsigned long iout; // output interval
unsigned long ntsl,nts,nts0; // total number of time steps (input value)
double **te;
double tau,a2,lambda,W,d0,a1,Gamma,DT,k,csEQ,clEQ;

phase1=fopen("phase1.dat","w");
phase2=fopen("phase2.dat","w");
phase3=fopen("phase3.dat","w");
phase4=fopen("phase4.dat","w");
phase5=fopen("phase5.dat","w");
conc1=fopen("conc1.dat","w");
conc2=fopen("conc2.dat","w");
conc3=fopen("conc3.dat","w");
conc4=fopen("conc4.dat","w");
conc5=fopen("conc5.dat","w");
phase=fopen("phase.dat","w");
conc=fopen("conc.dat","w");
parameters=fopen("parameters.dat","w");
V=fopen("V.dat","w");
df=fopen("datainput.dat","r");
rho=fopen("rho.dat","w");
Xaxis=fopen("Xaxis.dat","w");
Yaxis=fopen("Yaxis.dat","w");

if(df==NULL){
    cout<<"\nError opening datainput.dat!"<<endl;
    return 0;
};

fscanf(df,"%lu %lu %lf %lf %lf %lf %lf %lf %lf %lf %lu %lu %lf %lf %lf %lf %lf %lu %lf
    %lf %lf",&L,&M,&TmA,&TmB,&LA,&LB,&sigA,&sigB,&vm,&Dl,&nts0,&ntsl,&T0,
    &c0,&eps4,&fluc,&S,&iout,&a1,&a2,&lambda);
cout<<"\nL:"<<L<<"\nM:"<<M<<"\nTmA:"<<TmA<<"\nTmB:"<<TmB<<
```

```
    "\nLA:"<<LA<<"\nLB:"<<LB<<"\nsigA:"<<sigA<<"\nsigB:"<<sigB<<"\n
    vm:"<<vm<<"\nDl:"<<Dl<<"\nnts0:"<<nts0<<"\nntsl:"<<ntsl<<"\nc0:"<<
    c0<<"\nT0:"<<T0<<"\neps4:"<<eps4<<"\nS:"<<S<<"\niout: "<<iout<<"\na1
    :"<<a1<<"\na2:"<<a2<<"\nlambda:"<<lambda<<endl;

fprintf(parameters,"////////////////////////////////////////////////////////
      ///\n");
fprintf(parameters,"////          Phase-field simulation                    /
   ///\n");
fprintf(parameters,"////          2D dendritic growth of binary alloys      /
   ///\n");
fprintf(parameters,"////          under an isothermal condition             /
   ///\n");
fprintf(parameters,"////          tip radius calculation                    /
   ///\n");
fprintf(parameters,"////          epsilon_4                                 /
hspace5 mm///\n");
fprintf(parameters,"////          no solid diffusion                        /
   ///\n");
fprintf(parameters,"////          simple adaptive grid                      /
   ///\n");
fprintf(parameters,"////------------------------------------------------------/
   ///\n");
fprintf(parameters,"////          Thin-interface limit model                /
   ///\n");
fprintf(parameters,"////          Anti-trapping current                     /
   ///\n");
fprintf(parameters,"////          based on Tong,Greenwood,and Provatas (2008,PRB)  /
   ///\n");
fprintf(parameters,"////          TIL_ATC.cpp                               /
   ///\n");
fprintf(parameters,"////          Last updated : 10/8/2009 by Jeong Yun Choi /
   ///\n");
fprintf(parameters,"////////////////////////////////////////////////////////
   ///////\n\n\n\n");
fprintf(parameters,"////INPUT PARAMETERS\n\n");
fprintf(parameters,"Total number of grid points (L):\t%lu\n",L);
fprintf(parameters,"Melting temperature of the solvent element (TmA) [K]:\t%g\n",TmA);
fprintf(parameters,"Melting temperature of the solute element (TmB) [K]:\t%g\n",TmB);
fprintf(parameters,"Latent heat of the solvent element (LA) [J/m3]:\t%g\n",LA);
fprintf(parameters,"Latent heat of the solute element (LB) [J/m3]:\t%g\n",LB);
fprintf(parameters,"Solid/liquid interfacial energy of the solvent element (sigA) [J/m2]:
   %g\n",sigA);
fprintf(parameters,"Solid/liquid interfacial energy of the solute element (sigB) [J/m2]:
   %g\n",sigB);
fprintf(parameters,"Average molar volume (vm) [m3/mol]:\t%g\n",vm);
```

```
fprintf(parameters,"Diffusion coefficient of the liquid phase (Dl) [m2/sec]:\t%g\n",Dl);
fprintf(parameters,"Initial temperature at the first grid point (T0) [K]:\t%g\n",T0);
fprintf(parameters,"Initial composition (c0) [atomic fraction]:\t%g\n",c0);
fprintf(parameters,"FDM stability parameter (S):\t%g\n",S);
fprintf(parameters,"Initial time steps to calculate (nts0):\t%lu\n",nts0);
fprintf(parameters,"Input final time steps to calculate (ntsl):\t%lu\n",ntsl);
fprintf(parameters,"Four-fold anisotropy (eps4):\t%g\n",eps4);
fprintf(parameters,"degree of noise (fluc):\t%g\n",fluc);
fprintf(parameters,"a1 :\t%g\n",a1);
fprintf(parameters,"a2 :\t%g\n",a2);
fprintf(parameters,"lambda :\t%g\n",lambda);

x=(double *)malloc((L+1)*sizeof(double));
if(x==NULL){
    cout<<"Out of Memory"<<endl;
    exit(0);
};

y=(double *)malloc((M+1)*sizeof(double));
if(y==NULL){
    cout<<"Out of Memory"<<endl;
    exit(0);
};

c=(double **)malloc((L+2)*sizeof(double));
for(i=0;i<L+2;i++){
    c[i]=(double *)malloc((M+2)*sizeof(double));
    if(c[i]==NULL){
        cout<<"Out of Memory"<<endl;
        exit(0);
    };
};
if(c==NULL){
    cout<<"Out of Memory"<<endl;
    exit(0);
};

cp=(double **)malloc((L+2)*sizeof(double));
for(i=0;i<L+2;i++){
    cp[i]=(double *)malloc((M+2)*sizeof(double));
    if(cp[i]==NULL)
        cout<<"Out of Memory"<<endl;
        exit(0);
    };
};
if(cp==NULL){
```

```
    cout<<"Out of Memory"<<endl;
    exit(0);
};

phi=(double **)malloc((L+2)*sizeof(double));
for(i=0;i<L+2;i++){
    phi[i]=(double *)malloc((M+2)*sizeof(double));
    if(phi[i]==NULL){
        cout<<"Out of Memory"<<endl;
        exit(0);
    };
};
if(phi==NULL){
    cout<<"Out of Memory"<<endl;
    exit(0);
};

phip=(double **)malloc((L+2)*sizeof(double));
for(i=0;i<L+2;i++){
    phip[i]=(double *)malloc((M+2)*sizeof(double));
    if(phip[i]==NULL){
        cout<<"Out of Memory"<<endl;
        exit(0);
    };
};
if(phip==NULL){
    cout<<"Out of Memory"<<endl;
    exit(0);
};

U=(double **)malloc((L+2)*sizeof(double));
for(i=0;i<L+2;i++){
    U[i]=(double *)malloc((M+2)*sizeof(double));
    if(U[i]==NULL){
        cout<<"Out of Memory"<<endl;
        exit(0);
    };
};
if(U==NULL){
    cout<<"Out of Memory"<<endl;
    exit(0);
};

Up=(double **)malloc((L+2)*sizeof(double));
for(i=0;i<L+2;i++){
    Up[i]=(double *)malloc((M+2)*sizeof(double));
```

```
    if(Up[i]==NULL){
        cout<<"Out of Memory"<<endl;
        exit(0);
    };
};
if(Up==NULL){
    cout<<"Out of Memory"<<endl;
    exit(0);
};

Gamma=sigA*TmA/LA;
csEQ=csE(T0);
clEQ=clE(T0);
k=csEQ/clEQ;
DT=Tl(csEQ)-T0;
d0=Gamma/DT;
W=lambda*d0/a1;
tau=a2*lambda/Dl*pow(W,2.);
dx=0.4*W;

fprintf(parameters,"Gibbs-Thomson coefficient (Gamma)[Km]:\t%g\n",Gamma);
fprintf(parameters,"Equilibrium solidus concentration (csEQ)[at.%]:\t%g\n",csEQ);
fprintf(parameters,"Equilibrium liquidus concentration (clEQ)[at.%]:\t%g\n",clEQ);
fprintf(parameters,"Equilibrium partition coefficient (k):\t%g\n",k);
fprintf(parameters,"Solidification temperature range (DT)[K]:\t%g\n",DT);
fprintf(parameters,"Solutal capillary length (d0)[m]:\t%g\n",d0);
fprintf(parameters,"Interface width (W)[m]:\t%g\n",W);
fprintf(parameters,"Interface kinetic attachment time (tau)[sec]:\t%g\n",tau);
fprintf(parameters,"Grid spacing (dx) [m]:\t%g\n",dx);

start(L,M,c0,dx,clEQ,k); // set the initial condition
dt=timestep(Dl,S,dx,tau,W,k); // calculate dt

for(nts=nts0;nts<=ntsl;nts++){
    gbp=gb;
    if(nts!=nts0) gb=((iip>jjp)?iip:jjp)+15;
    diff(nts,L,M,dt,dx,Dl,vm,c0,T0,fluc,LA,LB,TmA,TmB,eps4,tau,lambda,k,W,clEQ);
    if(!(nts%iout)){
        if((L%2)==1)
            cout<<nts<<"/"<<ntsl<<"\tt="<<dt*nts<<"\n\tii="<<ii<<"\tphi[1][1]=
                "<<phi[1][1]<<"\n\tc[L][1]="<<c[L][1] <<"\tphi[L][1]="<<phi[L][1]<<"gb
                ="<<gb<<endl;
            else cout<<nts<<"/"<<ntsl<<"\tt="<<dt*nts<<"\n\tii="<<ii<<"\tphi[1]
                [1]="<<phi[1][1]<<"\n\tc[L-1][1]="<<c[L-1][1]<<"\tphi[L-1][1]="<<phi[L
                -1][1]<<"\tgb="<<gb<<endl;
        };
```

```
if(ii>=L-1 || jj>=M-1) {nts++;break;};
if(nts<=ntsl/5 && nts+1>ntsl/5){
    for(i=1;i<=L;i++){
        for(j=1;j<=M;j++){
            fprintf(phase1,"%g\n",phi[i][j]);
            if((i>gb || j>gb) && (i%2)*(j%2)==0){
                if(i%2==0){
                    if(j%2==0){
                        if(i!=L && j!=L)
                            fprintf(conc1,"%g\n",(c[i-1][j-1]+c[i-1][j+1]+c[i+1][j-1]+c[i+1][
                                j+1])/4.);
                        else if(i==L && j==L)
                            fprintf(conc1,"%g\n",c[i-1][j-1]);
                        else if(i==L)
                            fprintf(conc1,"%g\n",(c[i-1][j-1]+c[i-1][j+1])/2.);
                        else fprintf(conc1,"%g\n",(c[i-1][j-1]+c[i+1][j-1])/2.);
                    }
                    else {
                        if(i==L)
                            fprintf(conc1,"%g\n",c[i-1][j]);
                        else
                            fprintf(conc1,"%g\n",(c[i-1][j]+c[i+1][j])/2.);
                    };
                }
                else {
                    if(j==M)
                        fprintf(conc1,"%g\n",c[i][j-1]);
                    else
                        fprintf(conc1,"%g\n",(c[i][j-1]+c[i][j+1])/2.);
                };
            }
            else fprintf(conc1,"%g\n",c[i][j]);
        };
        fprintf(phase1,"\n");
        fprintf(conc1,"\n");
    };
    fclose(phase1);fclose(conc1);
}
else if(nts>ntsl/5){
    if(nts<=ntsl*2/5 && nts+1>ntsl*2/5){
        for(i=1;i<=L;i++){
            for(j=1;j<=M;j++){
                fprintf(phase2,"%g\n",phi[i][j]);
                if((i>gb || j>gb) && (i%2)*(j%2)==0){
                    if(i%2==0){
                        if(j%2==0){
```

```
                    if(i!=L && j!=L)
                        fprintf(conc2,"%g\n",(c[i-1][j-1]+c[i-1][j+1]+c[i+1][j-1]+c[i
                            +1][j+1])/4.);
                    else if(i==L && j==L)
                        fprintf(conc2,"%g\n",c[i-1][j-1]);
                    else if(i==L)
                        fprintf(conc2,"%g\n",(c[i-1][j-1]+c[i-1][j+1])/2.);
                    else fprintf(conc2,"%g\n",(c[i-1][j-1]+c[i+1][j-1])/2.);
                }
                else {
                    if(i==L)
                        fprintf(conc2,"%g\n",c[i-1][j]);
                    else
                        fprintf(conc2,"%g\n",(c[i-1][j]+c[i+1][j])/2.);
                };
            }
            else {
                if(j==M)
                    fprintf(conc2,"%g\n",c[i][j-1]);
                else
                    fprintf(conc2,"%g\n",(c[i][j-1]+c[i][j+1])/2.);
            };
        }
        else fprintf(conc2,"%g\n",c[i][j]);
    };
    fprintf(phase2,"\n");
    fprintf(conc2,"\n");
};
fclose(phase2);fclose(conc2);
}
else if(nts>ntsl*2/5){
    if(nts<=ntsl*3/5 && nts+1>ntsl*3/5){
        for(i=1;i<=L;i++){
            for(j=1;j<=M;j++){
                fprintf(phase3,"%g\n",phi[i][j]);
                if((i>gb || j>gb) && (i%2)*(j%2)==0){
                    if(i%2==0){
                        if(j%2==0){
                            if(i!=L && j!=L)
                                fprintf(conc3,"%g\n",(c[i-1][j-1]+c[i-1][j+1]+c[i+1][j-1]+
                                    c[i+1][j+1])/4.);
                            else if(i==L && j==L)
                                fprintf(conc3,"%g\n",c[i-1][j-1]);
                            else if(i==L)
                                fprintf(conc3,"%g\n",(c[i-1][j-1]+c[i-1][j+1])/2.);
                            else fprintf(conc3,"%g\n",(c[i-1][j-1]+c[i+1][j-1])/2.);
```

```
                    }
                    else {
                        if(i==L)
                            fprintf(conc3,"%g\n",c[i-1][j]);
                        else
                            fprintf(conc3,"%g\n",(c[i-1][j]+c[i+1][j])/2.);
                    };
                }
                else {
                    if(j==M)
                        fprintf(conc3,"%g\n",c[i][j-1]);
                    else
                        fprintf(conc3,"%g\n",(c[i][j-1]+c[i][j+1])/2.);
                };
            }
            else fprintf(conc3,"%g\n",c[i][j]);
        };
        fprintf(phase3,"\n");
        fprintf(conc3,"\n");
    };
    fclose(phase3);fclose(conc3);
}
else if(nts>ntsl*3/5){
    if(nts<=ntsl*4/5 && nts+1>ntsl*4/5){
        for(i=1;i<=L;i++){
            for(j=1;j<=M;j++){
                fprintf(phase4,"%g\n",phi[i][j]);
                if((i>gb || j>gb) && (i%2)*(j%2)==0){
                    if(i%2==0){
                        if(j%2==0){
                            if(i!=L && j!=L)
                                fprintf(conc4,"%g\n",(c[i-1][j-1]+c[i-1][j+1]+c[i+1][j-1]
                                    +c[i+1][j+1])/4.);
                            else if(i==L && j==L)
                                fprintf(conc4,"%g\n",c[i-1][j-1]);
                            else if(i==L)
                                fprintf(conc4,"%g\n",(c[i-1][j-1]+c[i-1][j+1])/2.);
                            else
                                fprintf(conc4,"%g\n",(c[i-1][j-1]+c[i+1][j-1])/2.);
                        }
                        else {
                            if(i==L)
                                fprintf(conc4,"%g\n",c[i-1][j]);
                            else
                                fprintf(conc4,"%g\n",(c[i-1][j]+c[i+1][j])/2.);
                        };
```

```
                        }
                        else {
                            if(j==M)
                                fprintf(conc4,"%g\n",c[i][j-1]);
                            else
                                fprintf(conc4,"%g\n",(c[i][j-1]+c[i][j+1])/2.);
                        };
                    }
                    else fprintf(conc4,"%g\n",c[i][j]);
                };
                fprintf(phase4,"\n");
                fprintf(conc4,"\n");
            };
            fclose(phase4);fclose(conc4);
        };
    };
};
if(ii!=iip){
    radius(dx,dt,nts);
};
iip=ii;ii=0;
jjp=jj;jj=0;
te=phip,phip=phi,phi=te;
te=cp,cp=c,c=te;
te=Up,Up=U,U=te;
}

cout<<"total number of time step="<<nts-1<<"\n";
fprintf(parameters,"total number of time step=%lu\n",nts-1);
fprintf(parameters,"total time of growth =%g\n",(nts-1)*dt);

for(i=1;i<=L;i++){
    fprintf(Xaxis,"%g\t",x[i]);
    for(j=1;j<=M;j++){
        fprintf(phase5,"%g\n",phip[i][j]);
        if((i>gb || j>gb) && (i%2)*(j%2)==0){
            if(i%2==0){
                if(j%2==0){
                    if(i!=L && j!=L)
                        fprintf(conc5,"%g\n",(cp[i-1][j-1]+cp[i-1][j+1]+cp[i+1][j-1]+cp[i+1][j
                            +1])/4.);
                    else if(i==L && j==L)
                        fprintf(conc5,"%g\n",cp[i-1][j-1]);
                    else if(i==L)
                        fprintf(conc5,"%g\n",(cp[i-1][j-1]+cp[i-1][j+1])/2.);
```

```
                else
                    fprintf(conc5,"%g\n",(cp[i-1][j-1]+cp[i+1][j-1])/2.);
            }
            else {
                if(i==L)
                    fprintf(conc5,"%g\n",cp[i-1][j]);
                else
                    fprintf(conc5,"%g\n",(cp[i-1][j]+cp[i+1][j])/2.);
            };
        }
        else {
            if(j==M)
                fprintf(conc5,"%g\n",cp[i][j-1]);
            else
                fprintf(conc5,"%g\n",(cp[i][j-1]+cp[i][j+1])/2.);
        };
    }
    else fprintf(conc5,"%g\n",cp[i][j]);
    if(i==L) fprintf(Yaxis,"%g\t",y[j]);
};
fprintf(phase5,"\n");
fprintf(conc5,"\n");
};
cout<<"gb="<<gb<<endl;
time(&time2);
seconds=(unsigned long)difftime(time2,time1);
minutes=seconds/60;
secs_left=seconds%60;
hours=minutes/60;
mins_left=minutes%60;
cout<<"total CPU time="<<hours<<" h "<<mins_left<<" m "<<secs_left<<" s\n";
fprintf(parameters,"total CPU time=%u h %u m %u s\n",hours,mins_left,secs_left);

fclose(phase);fclose(phase5);
fclose(conc);fclose(conc5);
fclose(V);fclose(parameters);fclose(df);fclose(rho);fclose(Yaxis);fclose(Xaxis);
for(i=0;i<L+2;i++){
    free(c[i]);
    free(cp[i]);
    free(phi[i]);
    free(phip[i]);
    free(U[i]);
    free(Up[i]);
};

free(x);free(y);free(phi);free(phip);free(c);free(cp);free(U);free(Up);
```

```
        return 0;
}

double clE(double T0)
{
    //******** fitted phase diagram of Ni-Cu alloy calculated by phase-field simulation using
        ideal solution model (1382K<=T<=1592K)********//
    return(-1.242e-6*pow(T0,2.)+0.00113*T0+1.758);
}

double csE(double T0)
{
    //******** fitted phase diagram of Ni-Cu alloy calculated by phase-field simulation using
        ideal solution model (1382K<=T<=1592K)********//
    return(7.388e-7*pow(T0,2.)-0.00498*T0+6.403);
}

void diff(unsigned long nts,unsigned long L,unsigned long M,double dt,double dx,double Dl,
    double vm,double c0,double T0,double fluc,double LA,double LB,double TmA,double
    TmB,double eps4,double tau,double lambda,double k,double W,double clEQ)
{
    unsigned long i,j;
    double A0,GE,GW,GN,GS;
    double phipP,phipE,phipW,phipN,phipS,phipWN,phipEN,phipWS,phipES,phiP,phiE,
        phiW,phiN,phiS,UpP,UpE,UpW,UpN,UpS;

    for(i=1;i<=L;i++){
        for(j=1;j<=M;j++){
            if(i<=gb && j<=gb){
                phipP=phip[i][j];
                phipE=phip[i+1][j];
                phipW=phip[i-1][j];
                phipN=phip[i][j+1];
                phipS=phip[i][j-1];
                phipEN=phip[i+1][j+1];
                phipWN=phip[i-1][j+1];
                phipES=phip[i+1][j-1];
                phipWS=phip[i-1][j-1];

                if((i>gbp || j>gbp) && (i%2)*(j%2)==0){
                    if(i%2==0){
                        if(j%2==0){
                            if(i!=L && j!=L)
                                Up[i][j]=(Up[i-1][j-1]+Up[i-1][j+1]+Up[i+1][j-1]+Up[i+1][j+1])/4.;
                            else if(i==L && j==L)
                                Up[i][j]=Up[i-1][j-1];
```

```
            else if(i==L)
                Up[i][j]=(Up[i-1][j-1]+Up[i-1][j+1])/2.;
            else Up[i][j]=(Up[i-1][j-1]+Up[i+1][j-1])/2.;
        }
        else {
            if(i==L) Up[i][j]=Up[i-1][j];
            else Up[i][j]=(Up[i-1][j]+Up[i+1][j])/2.;
        };
    }
    else {
        if(j==M)
            Up[i][j]=Up[i][j-1];
        else
            Up[i][j]=(Up[i][j-1]+Up[i][j+1])/2.;
    };
};
UpP=Up[i][j];
if(i==1 && j==1){
    phipW=phipE;
    phipS=phipN;
    phipWN=phipEN;
    phipES=phipEN;
    phipWS=phipEN;
}
else if(i==1 && j!=M){
    phipW=phipE;
    phipWN=phipEN;
    phipWS=phipES;
}
else if(i==1){
    phipW=phipE;
    phipN=phipS;
    phipWN=phipES;
    phipEN=phipES;
    phipWS=phipES;
}
else if(i!=L && j==1){
    phipS=phipN;
    phipES=phipEN;
    phipWS=phipWN;
}
else if(i!=L && j==M){
    phipN=phipS;
    phipWN=phipWS;
    phipEN=phipES;
}
```

```
            else if(i==L && j==1){
                phipE=phipW;
                phipS=phipN;
                phipEN=phipWN;
                phipES=phipWN;
                phipWS=phipWN;
            }
            else if(i==L && j!=M){
                phipE=phipW;
                phipEN=phipWN;
                phipES=phipWS;
            }
            else if(i==L){
                phipE=phipW;
                phipN=phipS;
                phipEN=phipWS;
                phipES=phipWS;
                phipWN=phipWS;
            };

            if(phipE==phipW && phipN==phipS){
                phi[i][j]=phipP+dt/tau*((phipP-pow(phipP,3.)-lambda*pow(1.-pow(phipP,2.)
                    ,2.)*UpP)+pow(W/dx,2.)*(2./3.*(phipE+phipW+phipN+phipS+1./4.*(
                    phipEN+phipWN+phipES+phipWS)-5.*phipP)));
            }
            else {
                A0=1.+4.*eps4/(1.-3.*eps4)*(pow(phipE-phipW,4.)+pow(phipN-phipS,4.))/
                    pow(pow(phipE-phipW,2.)+pow(phipN-phipS,2.),2.);
                phi[i][j]=phipP+dt/tau*((phipP-pow(phipP,3.)-lambda*pow(1.-pow(phipP,2.)
                    ,2.)*UpP)/pow((1.-3.*eps4)*A0,2.)+pow(W/dx,2.)*(2./3.*(phipE+phipW
                    +phipN+phipS+1./4.*(phipEN+phipWN+phipES+phipWS)-5.*phipP)+
                    16.*eps4/((1.-3.*eps4)*A0*(pow(phipE-phipW,2.)+pow(phipN-phipS,2.)))
                    *((phipE-2.*phipP+phipW)*(pow(phipE-phipW,2.)-(pow(phipE-phipW,4.
                    )+pow(phipN-phipS,4.))/(pow(phipE-phipW,2.)+pow(phipN-phipS,2.)))+
                    (phipN-2.*phipP+phipS)*(pow(phipN-phipS,2.)-(pow(phipE-phipW,4.)+
                    pow(phipN-phipS,4.))/(pow(phipE-phipW,2.)+pow(phipN-phipS,2.))))));
            };

            if(i>ii && phi[i][j]<=0. && phi[i-1][j]>=0.) ii=i;
            if(j>jj && phi[i][j]<=0. && phi[i][j-1]>=0.) jj=j;
        }
        else phi[i][j]=-1.;
    };
};
for(i=1;i<=L;i++){
    for(j=1;j<=M;j++){
```

```
if(i<=gb && j<=gb){
    UpP=Up[i][j];
    if(((i+1)>gbp || j>gbp) && ((i+1)%2)*(j%2)==0){
        if((i+1)%2==0){
            if(j%2==0){
                if((i+1)!=L && j!=L)
                    UpE=(Up[i][j-1]+Up[i][j+1]+Up[i+2][j-1]+Up[i+2][j+1])/4.;
                else if((i+1)==L && j==L)
                    UpE=Up[i][j-1];
                else if((i+1)==L)
                    UpE=(Up[i][j-1]+Up[i][j+1])/2.;
                else
                    UpE=(Up[i][j-1]+Up[i+2][j-1])/2.;
            }
            else {
                if((i+1)==L)
                    UpE=Up[i][j];
                else
                    UpE=(Up[i][j]+Up[i+2][j])/2.;
            };
        }
        else {
            if(j==M)
                UpE=Up[i+1][j-1];
            else
                UpE=(Up[i+1][j-1]+Up[i+1][j+1])/2.;
        };
    }
    else UpE=Up[i+1][j];
    UpW=Up[i-1][j];
    if((i>gbp || (j+1)>gbp) && (i%2)*((j+1)%2)==0){
        if(i%2==0){
            if((j+1)%2==0){
                if(i!=L && (j+1)!=L)
                    UpN=(Up[i-1][j]+Up[i-1][j+2]+Up[i+1][j]+Up[i+1][j+2])/4.;
                else if(i==L && (j+1)==L)
                    UpN=Up[i-1][j];
                else if(i==L)
                    UpN=(Up[i-1][j]+Up[i-1][j+2])/2.;
                else
                    UpN=(Up[i-1][j]+Up[i+1][j])/2.;
            }
            else {
                if(i==L)
                    UpN=Up[i-1][j+1];
                else
```

```
                UpN=(Up[i-1][j+1]+Up[i+1][j+1])/2.;
        };
    }
    else {
        if((j+1)==M)
            UpN=Up[i][j];
        else
            UpN=(Up[i][j]+Up[i][j+2])/2.;
    };
}
else UpN=Up[i][j+1];
UpS=Up[i][j-1];
phipP=phip[i][j];
phipE=phip[i+1][j];
phipW=phip[i-1][j];
phipN=phip[i][j+1];
phipS=phip[i][j-1];
phipEN=phip[i+1][j+1];
phipWN=phip[i-1][j+1];
phipES=phip[i+1][j-1];
phipWS=phip[i-1][j-1];
phiP=phi[i][j];
phiE=phi[i+1][j];
phiW=phi[i-1][j];
phiN=phi[i][j+1];
phiS=phi[i][j-1];

if(i==1 && j==1){
    UpW=UpE;
    UpS=UpN;
    phipW=phipE;
    phipS=phipN;
    phipWN=phipEN;
    phipES=phipEN;
    phipWS=phipEN;
    phiW=phiE;
    phiS=phiN;
}
else if(i==1 && j!=M){
    UpW=UpE;
    phipW=phipE;
    phipWN=phipEN;
    phipWS=phipES;
    phiW=phiE;
}
else if(i==1){
```

```
    UpW=UpE;
    UpN=UpS;
    phipW=phipE;
    phipN=phipS;
    phipEN=phipES;
    phipWN=phipES;
    phipWS=phipES;
    phiW=phiE;
    phiN=phiS;
}
else if(i!=L && j==1){
    UpS=UpN;
    phipS=phipN;
    phipES=phipEN;
    phipWS=phipWN;
    phiS=phiN;
}
else if(i!=L && j==M){
    UpN=UpS;
    phipN=phipS;
    phipEN=phipES;
    phipWN=phipWS;
    phiN=phiS;
}
else if(i==L && j==1){
    UpE=UpW;
    UpS=UpN;
    phipE=phipW;
    phipS=phipN;
    phipEN=phipWN;
    phipES=phipWN;
    phipWS=phipWN;
    phiE=phiW;
    phiS=phiN;
}
else if(i==L && j!=M){
    UpE=UpW;
    phipE=phipW;
    phipEN=phipWN;
    phipES=phipWS;
    phiE=phiW;
}
else if(i==L){
    UpE=UpW;
    UpN=UpS;
    phipE=phipW;
```

```
        phipN=phipS;
        phipEN=phipWS;
        phipWN=phipWS;
        phipES=phipWS;
        phiE=phiW;
        phiN=phiS;
    };

    if(phipE==phipP && phipEN+phipN-(phipES+phipS)<1.e-15) GE=0.;
    else GE=(4.*phipE-4.*phipP)/sqrt(16.*pow(phipE-phipP,2.)+pow(phipEN-
        phipES+phipN-phipS,2.));
    if(phipW==phipP && phipWN+phipN-(phipWS+phipS)<1.e-15) GW=0.;
    else GW=(4.*phipP-4.*phipW)/sqrt(16.*pow(phipP-phipW,2.)+pow(phipWN-
        phipWS+phipN-phipS,2.));
    if(phipN==phipP && phipEN+phipE-(phipWN+phipW)<1.e-15) GN=0.;
    else GN=(4.*phipN-4.*phipP)/sqrt(16.*pow(phipN-phipP,2.)+pow(phipE-
        phipW+phipEN-phipWN,2.));
    if(phipS==phipP && phipES+phipE-(phipWS+phipW)<1.e-15) GS=0.;
    else GS=(4.*phipP-4.*phipS)/sqrt(16.*pow(phipP-phipS,2.)+pow(phipE-phipW
        +phipES-phipWS,2.));

    U[i][j]=UpP+(1.+(1.-k)*UpP)/(1.+k-(1.-k)*phipP)*(phiP-phipP)+1./(2.*dx*(1.
        +k-(1.-k)*phipP))*(Dl*dt/dx*((2.-phipE-phipP)*(UpE-UpP)-(2.-phipP-
        phipW)*(UpP-UpW)+(2.-phipN-phipP)*(UpN-UpP)-(2.-phipP-phipS)*(UpP
        -UpS))+W/sqrt(2.)*(((1.+(1.-k)*UpE)*(phiE-phipE)+(1.+(1.-k)*UpP)*(
        phiP-phipP))*GE-((1.+(1.-k)*UpP)*(phiP-phipP)+(1.+(1.-k)*UpW)*(phiW-
        phipW))*GW+((1.+(1.-k)*UpN)*(phiN-phipN)+(1.+(1.-k)*UpP)*(phiP-
        phipP))*GN-((1.+(1.-k)*UpP)*(phiP-phipP)+(1.+(1.-k)*UpS)*(phiS-phipS))
        *GS));
}
else if((i%2)*(j%2)==1){
    UpP=Up[i][j];
    phipP=phip[i][j];
    phiP=phi[i][j];
    if(i+2<=L){
        UpE=Up[i+2][j];
        phipE=phip[i+2][j];
        phiE=phi[i+2][j];
    }
    else{
        UpE=Up[i][j];
        phipE=phip[i][j];
        phiE=phi[i][j];
    };
    if(i>=3){
        UpW=Up[i-2][j];
```

```
    phipW=phip[i-2][j];
    phiW=phi[i-2][j];
}
else{
    UpW=Up[i][j];
    phipW=phip[i][j];
    phiW=phi[i][j];
};
if(j+2<=L){
    UpN=Up[i][j+2];
    phipN=phip[i][j+2];
    phiN=phi[i][j+2];
}
else {
    UpN=Up[i][j];
    phipN=phip[i][j];
    phiN=phi[i][j];
};
if(j>=3){
    UpS=Up[i][j-2];
    phipS=phip[i][j-2];
    phiS=phi[i][j-2];
}
else {
    UpS=Up[i][j];
    phipS=phip[i][j];
    phiS=phi[i][j];
};
if(i==1 && j==1){
    UpW=UpE;
    UpS=UpN;
    phipW=phipE;
    phipS=phipN;
    phiW=phiE;
    phiS=phiN;
}
else if(i==1 && j!=M){
    UpW=UpE;
    phipW=phipE;
    phiW=phiE;
}
else if(i==1){
    UpW=UpE;
    UpN=UpS;
    phipW=phipE;
    phipN=phipS;
```

```
                phiW=phiE;
                phiN=phiS;
            }
            else if(i!=L && j==1){
                UpS=UpN;
                phipS=phipN;
                phiS=phiN;
            }
            else if(i!=L && j==M){
                UpN=UpS;
                phipN=phipS;
                phiN=phiS;
            }
            else if(i==L && j==1){
                UpE=UpW;
                UpS=UpN;
                phipE=phipW;
                phipS=phipN;
                phiE=phiW;
                phiS=phiN;
            }
            else if(i==L && j!=M){
                UpE=UpW;
                phipE=phipW;
                phiE=phiW;
            }
            else if(i==L){
                UpE=UpW;
                UpN=UpS;
                phipE=phipW;
                phipN=phipS;
                phiE=phiW;
                phiN=phiS;
            };

            U[i][j]=UpP+1./(4.*dx*(1.+k-(1.-k)*phipP))*(Dl*dt/(2.*dx)*((2.-phipE-phipP)
                *(UpE-UpP)-(2.-phipP-phipW)*(UpP-UpW)+(2.-phipN-phipP)*(UpN-UpP)-
                (2.-phipP-phipS)*(UpP-UpS)));
        };
        c[i][j]=clEQ/2.*(U[i][j]*(1.-k)+1.)*(1.+k-(1.-k)*phipP);
    };
};
}

void radius(double dx,double dt,unsigned long nts)
{
```

```
    double xi,phiii_1,tipradi;

    xi=((0.-phi[ii][1])*dx+(phi[ii][1]-phi[ii-1][1])*x[ii])/(phi[ii][1]-phi[ii-1][1]);
    phiii_1=(phi[ii][2]-phi[ii-1][2])*xi/dx+phi[ii][2]-(phi[ii][2]-phi[ii-1][2])*x[ii]/dx;
    tipradi=(phi[ii][1]-phi[ii-1][1])*dx/(2.*phiii_1);

    fprintf(rho,"%g\t%g\t%g\n",dt*nts,xi,tipradi);
    if(nts%100==0) printf("rho=%g\n",tipradi);
}

void start(unsigned long L,unsigned long M,double c0,double dx,double clEQ,double k)
{
    unsigned long i,j;
/*
    for(i=1;i<=L;i++)
        for(j=1;j<=M;j++){
            cp[i][j]=c0;
            if(i+j<=30) phip[i][j]=1.; //triangle
//          if(i<=15 && j<=15) phip[i][j]=1.; //square
//          if(sqrt(double(i*i+j*j))<=15) phip[i][j]=1.; //circle
//          if(sqrt(double((i-L/2)*(i-L/2)+(j-M/2)*(j-M/2)))<=15) phip[i][j]=1.; //center
            else phip[i][j]=-1.;
            Up[i][j]=(2.*cp[i][j]/clEQ/(1.+k-(1.-k)*phip[i][j])-1.)/(1.-k);
            gb=45;
        };
    ugrid(L,M,dx); // set the positions of grid points
*/

    ifstream phiin,cin;

    phiin.open("phase_ini.dat");
    cin.open("c_ini.dat");

    for(i=1;i<=L;i++)
        for(j=1;j<=M;j++){
            if(i>3650 || j>3650){
                phip[i][j]=-1.;
                cp[i][j]=c0;
            }
            else{
                phiin>>phip[i][j];
                cin>>cp[i][j];
            };
            Up[i][j]=(2.*cp[i][j]/clEQ/(1.+k-(1.-k)*phip[i][j])-1.)/(1.-k);
            gb=724;iip=709;jjp=709;
        };
```

```
    phiin.close();
    cin.close();

    ugrid(L,M,dx); // set the positions of grid points
}

double timestep(double Dl,double S,double dx,double tau,double W,double k)
{
    double dt=(Dl/k>pow(W,2.)/tau)?S*dx*dx/(Dl/k):S*dx*dx/(pow(W,2.)/tau);

    fprintf(parameters,"time step=%g\n",dt);
    cout<<"time step="<<dt<<"\n";

    return(dt);
}

double Tl(double c)
{
    //******** fitted phase diagram of Ni-Cu alloy calculated by phase-field simulation using
        ideal solution model (1382K<=T<=1592K)********//
    return(-74.1*pow(c,2.)-289.*c+1723.);
}

void ugrid(unsigned long L,unsigned long M,double dx)
{
    //generating uniform grids
    unsigned long i,j;

    x[1]=0.;
    y[1]=0.;

    for(i=2;i<=L;i++)
        x[i]=x[i-1]+dx;
    for(j=2;j<=M;j++)

    y[j]=y[j-1]+dx;

    fprintf(parameters,"dx=%g\n",dx);
    cout<<"dx="<<dx<<endl;

}
```

APPENDIX B. THE DERIVATION OF PHASE-FIELD MODELS

The phase-field simulation is essentially to solve the Allen-Cahn equation (Eq. 4.4) and Cahn-Hilliard equation (Eq. 4.5) numerically. All the parameters and functions in those equations, such as a free energy density function, phase-field and concentration field mobilities, and a gradient penalty coefficient must be defined using physical parameters, for physically reliable results.

The sharp-interface limit model formulation

The following formulations are based on the model developed by Warren and Boettinger [108] which is the sharp-interface limit model introduced in chapter 4.2.1. It is simple and straightforward to derive. The phase-field variable, ϕ is set to zero in the solid phase and unity in the liquid phase. It has $0 < \phi < 1$ value for interface between solid and liquid phases.

Pure materials

To solve the governing equations (Eq. 4.4 and 4.5), the chemical free energy density, f, needs to be defined as a function of physical parameters of the system. f has a constant value in the bulk phases where $\phi = 0$ and 1. The values correspond to the bulk free energy densities, and the difference between adjacent bulk phases depends on the system temperature. Between the bulk phases ($0 < \phi < 1$), it is regarded that a free energy barrier exists. Desired shapes of f as a function of ϕ is described schematically in Figure B.1. When the system temperature equals to the melting temperature, T_M, there is no free energy density difference between the solid and liquid bulk phases. If the temperature is lower than T_M, the free energy density for solid is lower than that for liquid, and otherwise, it is higher than f for liquid phase.

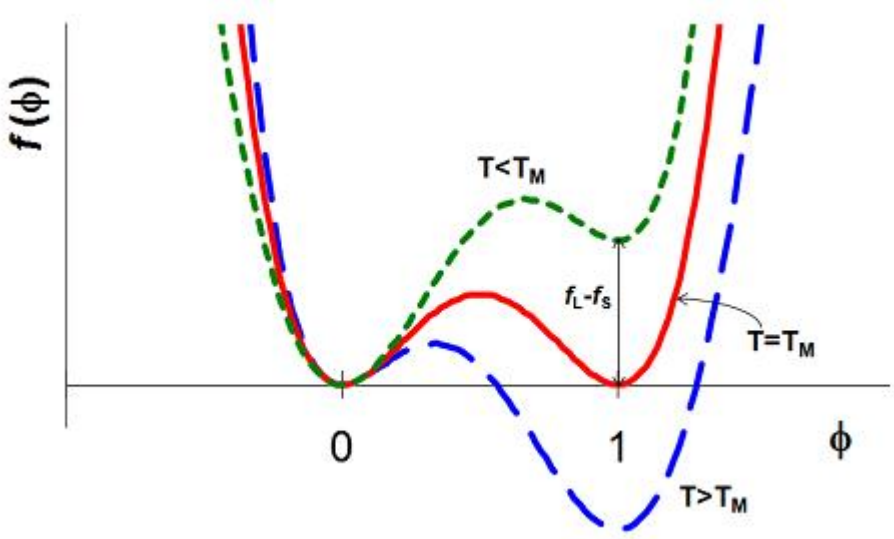

Figure B.1 Free energy density versus the phase-field variable, depending on temperature. It has local minima at $\phi = 0$ (solid) and $\phi = 1$ (liquid), and between those, there exists an energy barrier.

Including all these characteristics, The free energy density function can be described as

$$f(\phi) = Wg(\phi) + h(\phi)(f_L - f_S) + f_S \tag{B.1}$$

using auxiliary functions $g(\phi)$ and $h(\phi)$ where W is a parameter related to the free energy density barrier height, and f_L and f_S are the bulk free energy densities of the liquid and solid phases, respectively, i.e. $f_L = f(1)$ and $f_S = f(0)$. $g(\phi)$ is a function with a double well shape, and $g(0) = g(1) = 0$ as shown in Figure B.2 (a). This form of function can be made purely mathematically as following,

$$g(\phi) = \phi^2 (1 - \phi)^2 \tag{B.2}$$

The function, $h(\phi)$, has the smoothly increasing form, where $h(0) = 0$, and $h(1) = 1$ as shown in Figure B.2 (b). This function should be chosen to satisfy the condition that f has two

minima at $\phi = 0$ and $\phi = 1$, i.e.

$$\left.\frac{\partial f}{\partial \phi}\right|_{\phi=0,1} = 0$$
$$\left.\frac{\partial^2 f}{\partial \phi^2}\right|_{\phi=0,1} > 0 \tag{B.3}$$

When we apply the function $g(\phi)$ (equation B.2) to f (equation B.1), the simplest polynomial function $h(\phi)$that satisfies the condition (B.3), h(0)=0, and h(1) = 1 is

$$h(\phi) = \phi^3(10 - 15\phi + 6\phi^2) \tag{B.4}$$

The free energy density function with two auxiliary functions, (B.2) and (B.4), is

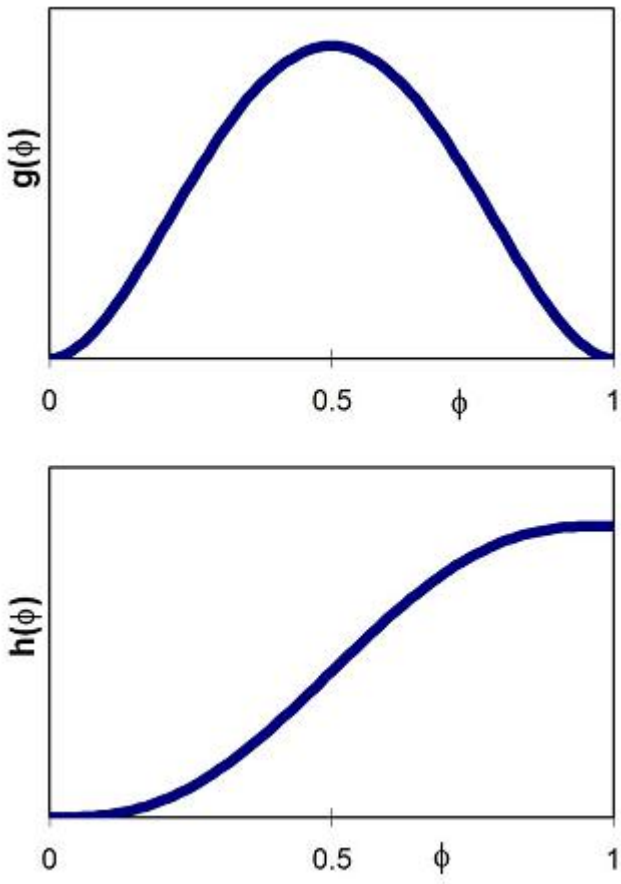

Figure B.2 Auxiliary functions, $g(\phi)$ and $h(\phi)$, used in phase-field model.

$$f(\phi) = W\phi^2(1-\phi)^2 + \phi^3(10 - 15\phi + 6\phi^2)(f_L - f_S) + f_S \tag{B.5}$$

and, its first and second derivatives are

$$\frac{\partial f}{\partial \phi} = 2W\phi(2\phi - 1)(\phi - 1) + 30(1-\phi)^2(f_L - f_S) \tag{B.6}$$

and

$$\frac{\partial^2 f}{\partial \phi^2} = 2W\left[6\phi(\phi - 1) + 1\right] + 60\phi(\phi - 1)(2\phi - 1)(f_L - f_S) \tag{B.7}$$

At $\phi = 0$ and $\phi = 1$, i.e. bulk phases, equation (B.6) goes to zero, and from the equation (B.7), the second derivative has the value of $2W$ which is positive since the energy barrier height is always positive. It shows that the condition (B.3) is satisfying with the auxiliary functions (B.2) and (B.4). The simplest form of the temperature-dependent bulk free energy density difference, $f_L - f_S$, in equation (B.1), can be given by

$$f_L - f_S = \frac{L}{T_M}(T_M - T) \tag{B.8}$$

Using these expression (B.1), (B.2), (B.4), and (B.8), the phase evolution equation (Eq. 4.4) becomes,

$$\begin{aligned} \frac{\partial \phi}{\partial t} &= -M_\phi \left[\frac{\partial f}{\partial \phi} - \epsilon^2 \nabla^2 \phi\right] \\ &= M_\phi \left[\epsilon^2 \nabla^2 \phi - W\frac{\partial g}{\partial \phi} - \frac{\partial h}{\partial \phi}(f_L - f_S)\right] \\ &= M_\phi \left[\epsilon^2 \nabla^2 \phi - W\frac{\partial g}{\partial \phi} - \frac{\partial h}{\partial \phi}\frac{L}{T_M}(T_M - T)\right] \end{aligned} \tag{B.9}$$

Since the solidification of pure materials is generally controlled by thermal diffusion process, in the phase-field simulation of pure materials, the phase evolution equation (B.9) is solved in conjunction with the following thermal diffusion equation:

$$\frac{\partial H}{\partial t} = \nabla \alpha \nabla H = \nabla k^T \nabla T \tag{B.10}$$

where the heat capacity, α is constant for both phases. To make this enthalpy generation

equation into the time-dependent temperature distribution equation, the enthalpy densities in the solid and liquid phases at temperature, T, can be given by

$$H_S(T) = H_S(T_M) + C_P(T - T_M)$$
$$H_L(T) = H_L(T_M) + C_P(T - T_M) \tag{B.11}$$

where the specific heats in solid and liquid phases are same and independent on temperatures. If we assume that the enthalpy density across the phase interface has a phase fraction-weited value, the enthalpy density for an interface could be,

$$H = h(\phi)H_L + (1 - h(\phi))H_S \tag{B.12}$$

Applying this enthalpy density into the thermal diffusion equation (B.10) yields

$$\frac{\partial T}{\partial t} = \frac{k_T}{C_P}\nabla^2 T - \frac{\partial h}{\partial \phi}\frac{\Delta H_f}{C_P}\frac{\partial \phi}{\partial t} \tag{B.13}$$

since

$$H_L(T) - H_S(T) = H_L(T_M) - H_S(T_M) = \Delta H_f \tag{B.14}$$

$$\frac{\partial H_L(T)}{\partial t} = \frac{\partial H_S(T)}{\partial t} = C_P\frac{\partial T}{\partial t} \tag{B.15}$$

from the bulk enthalpy densities (equation B.12).

Binary alloys

The bulk free energy density of binary alloys is usually described as a function of the phase-field, the temperature, and the solute concentration, and given as,

$$f_{S,L} = (1 - c)\tilde{\mu}^A_{S,L} + c\tilde{\mu}^B_{S,L} \tag{B.16}$$

where $\tilde{\mu}^A_{S,L}$ and $\tilde{\mu}^B_{S,L}$ are the chemical potentials of alloying component A and B, respectively, and c is the atomic concentration of solute component, B. According to the regular solution model, the chemical potentials for binary alloys are,

$$\tilde{\mu}^A_{S,L} = f^A_{S,L}(\phi, T) + \Omega_{S,L}(\phi)c^2 + \frac{RT}{v_m}\ln(1-c) \tag{B.17}$$

$$\tilde{\mu}^B_{S,L} = f^B_{S,L}(\phi, T) + \Omega_{S,L}(\phi)(1-c)^2 + \frac{RT}{v_m}\ln c \tag{B.18}$$

where $f^A_{S,L}$ and $f^B_{S,L}$ are free energy densities of pure metals, $\Omega_{S,L}$, is an enthalpy density of mixing which is a function of ϕ, v_m is a molar volume, and R is the gas constant. Then, the bulk free energy density of binary alloys in equation (B.16) is

$$\begin{aligned} f_{S,L} = (1-c)&\left\{ f^A_{S,L}(\phi, T) + \Omega_{S,L}(\phi)c^2 + \frac{RT}{v_m}\ln(1-c) \right\} \\ &+ c\left\{ f^B_{S,L}(\phi, T) + \Omega_{S,L}(\phi)(1-c)^2 + \frac{RT}{v_m}\ln c \right\} \end{aligned} \tag{B.19}$$

Applying these bulk free energy densities into the free energy density in equation (B.1) results in

$$\begin{aligned} f &= Wg(\phi) + h(\phi)\left(f_L - f_S\right) + f_S \\ &= Wg(\phi) + h(\phi)\left\{(1-c)\frac{L^A}{T^A_M}(T^A_M - T) + c\frac{L^B}{T^B_M}(T^B_M - T) + (\Omega_L - \Omega_S)c^2\right\} + f_S \end{aligned} \tag{B.20}$$

where $W = (1-c)W^A + cW^B$. Using this f, the phase-field evolution equation (Eq. 4.4) for alloys is

$$\frac{\partial \phi}{\partial t} = -M_\phi \begin{bmatrix} W\frac{\partial g}{\partial \phi} + \frac{\partial h}{\partial \phi}\left\{(1-c)\frac{L^A}{T^A_M}(T^A_M - T) + c\frac{L^B}{T^B_M}(T^B_M - T) + c(1-c)(\Omega_L - \Omega_S)\right\} \\ -\epsilon^2\nabla^2\phi \end{bmatrix} \tag{B.21}$$

This can be simplified in the case of ideal binary alloys ($\Omega_L = \Omega_S = 0$) as

$$\frac{\partial \phi}{\partial t} = M_\phi \left[\epsilon^2 \nabla^2 \phi - W \frac{\partial g}{\partial \phi} - \frac{\partial h}{\partial \phi} \left\{ (1-c) \frac{L^A}{T_M^A} (T_M^A - T) + c \frac{L^B}{T_M^B} (T_M^B - T) \right\} \right] \tag{B.22}$$

According to Kim *et al.* [131], the enthalpy, H, and temperature, T, in the thermal diffusion equation for pure materials can be mapped to the solute concentration, c, and chemical potential, $\tilde{\mu} = \partial f / \partial c$, respectively, for a solute diffusion equation. Therefore, mapping of the thermal diffusion equation (B.10) yields the solutal diffusion equation,

$$\frac{\partial c}{\partial t} = \nabla \frac{D}{\partial^2 f / \partial c^2} \nabla \frac{\partial f}{\partial c} \tag{B.23}$$

since $k^T = \alpha C_P = \alpha (\partial H / \partial T)$ is correspond to $D \partial c / (\partial f / \partial c) = D / (\partial^2 f / \partial c^2)$. D is a solute diffusion coefficient which can be represented as a phase fraction weighted value, i.e. $D(\phi) = D_S + h(\phi)(D_L - D_S)$. By the comparison of the equation (B.23) with the equation (4.5), the solute mobility parameter, M_c is equal to $D / (\partial^2 f / \partial c^2)$. Then, the equation (4.5) using the free energy density, f, in equation (B.1) becomes

$$\begin{aligned} \frac{\partial c}{\partial t} &= \nabla \cdot \left(M_c \nabla \frac{\partial f}{\partial c} \right) = \nabla \cdot \left(\frac{D}{f_{cc}} \nabla \frac{\partial f}{\partial c} \right) = \nabla \cdot \left(\frac{D}{f_{cc}} \left(\frac{\partial f_c}{\partial c} \nabla c + \frac{\partial f_c}{\partial \phi} \nabla \phi \right) \right) \\ &= \nabla \cdot \left(D \left(\nabla c + \frac{f_{c\phi}}{f_{cc}} \nabla \phi \right) \right) \end{aligned} \tag{B.24}$$

The derivative of the free energy density equation (B.1) with concentration is

$$\frac{\partial f}{\partial c} = \frac{\partial W}{\partial c} g + h \left(\frac{\partial f_L}{\partial c} - \frac{\partial f_S}{\partial c} \right) + \frac{\partial f_S}{\partial c} \tag{B.25}$$

and,

$$\frac{\partial^2 f}{\partial c \partial \phi} = \frac{\partial W}{\partial c} \frac{\partial g}{\partial \phi} + \frac{\partial h}{\partial \phi} \left(\frac{\partial f_L}{\partial c} - \frac{\partial f_S}{\partial c} \right) \tag{B.26a}$$

$$\frac{\partial^2 f}{\partial c^2} = h \left(\frac{\partial^2 f_L}{\partial c^2} - \frac{\partial^2 f_S}{\partial c^2} \right) + \frac{\partial^2 f_S}{\partial c^2} \tag{B.26b}$$

if W is not a function of a phase variable. Then, the equation (B.24) can be rewrite as

$$\frac{\partial c}{\partial t} = \nabla \cdot \left(D \left(\nabla c + \frac{\frac{\partial W}{\partial c}\frac{\partial g}{\partial \phi} + \frac{\partial h}{\partial \phi}\frac{\partial}{\partial c}(f_L - f_S)}{h\frac{\partial^2}{\partial c^2}(f_L - f_S) + \frac{\partial^2 f_S}{\partial c^2}} \nabla \phi \right) \right) \tag{B.27}$$

By using the free energy density function (B.20), solute diffusion equation (B.27) will be

$$\frac{\partial c}{\partial t} = \nabla \cdot D\left(\phi\right) \left(\begin{array}{l} \nabla c + \\ \quad \frac{\frac{\partial g}{\partial \phi}(W^B - W^A) + \frac{\partial h}{\partial \phi}\left\{ \frac{L^B}{T_M^B}(T_M^B - T) - \frac{L^A}{T_M^A}(T_M^A - T) + (1-2c)(\Omega_L - \Omega_S) \right\}}{\frac{RT}{v_m}\frac{1}{c(1-c)} - 2\Omega_S - 2h(\Omega_L - \Omega_S)} \nabla \phi \end{array} \right) \tag{B.28}$$

for regular binary alloys, and

$$\frac{\partial c}{\partial t} = \nabla \cdot D(\phi) \left(\begin{array}{l} \nabla c + \\ \quad \frac{v_m}{RT} c(1-c) \left[\frac{\partial g}{\partial \phi}(W^B - W^A) + \frac{\partial h}{\partial \phi} \left\{ \frac{L^B}{T_M^B}(T_M^B - T) - \frac{L^A}{T_M^A}(T_M^A - T) \right\} \right] \nabla \phi \end{array} \right) \tag{B.29}$$

for ideal binary alloys.

Model parameters

For the phase-field simulation of solidification using the phase-evolution equation (B.9, B.28, or B.29) and the diffusion equation (B.13 and/or B.27, B.28, or B.29), we need to define model parameters such as the chemical free energy barrier height, W, the gradient energy penalty coefficient, ϵ, and the phase-field mobility, M_ϕ, as functions of measurable physical parameters. Those measurable parameters could be the diffused interface thickness, δ, and solid/liquid interface energy, σ.

First, δ can be defined from the equilibrium phase-field profile. When we consider the equilibrium state, f_S equals to f_L, and no phase evolution occurs. In this case the phase evolution equation (Eq. 4.4) becomes

$$\frac{\partial \phi}{\partial t} = M_\phi \left[\epsilon^2 \nabla^2 \phi - W \frac{\partial g}{\partial \phi} \right] = 0 \tag{B.30}$$

i.e.

$$W\frac{\partial g}{\partial \phi} = \epsilon^2 \nabla^2 \phi \tag{B.31}$$

Considering one-dimensional coordination, the multiplication of $d\phi/dx$ on both sides of equation (B.31) and integration by x give

$$\int_0^\infty W\frac{dg}{d\phi}\frac{d\phi}{dx}dx = \int_0^\infty \epsilon^2 \frac{d^2\phi}{dx^2}\frac{d\phi}{dx}dx \tag{B.32}$$

After canceling the terms in the left hand side and integral by part of right hand side, above equation can be rewritten as following:

$$\int_0^\infty W dg = \frac{\epsilon^2}{2}\left(\frac{d\phi}{dx}\right)^2 \tag{B.33}$$

Therefore, the solution of equation (B.31) for g is

$$g = \frac{\epsilon^2}{2W}\left(\frac{d\phi}{dx}\right)^2 \tag{B.34}$$

If we use the equation (B.2) for g, rewriting the equation (B.34) for x gives

$$x = \frac{\epsilon}{\sqrt{2W}}\int \frac{d\phi}{\sqrt{g}} = \frac{\epsilon}{\sqrt{2W}}\int \frac{d\phi}{\phi(1-\phi)} = \frac{\epsilon}{\sqrt{2W}}\ln\frac{\phi}{1-\phi} \tag{B.35}$$

and the figure B.3 shows this relationship between x and ϕ.

Interface region can be arbitrarily defined. If the interface region is defined as the region for $\phi = 0.5 \pm \Delta$, then, using equation (B.35), δ is given by

$$\delta = x_{\phi=0.5+\Delta} - x_{\phi=0.5-\Delta} \approx \frac{a_0\epsilon}{\sqrt{2W}} \tag{B.36}$$

where the value of a_0 is determined by Δ (Figure B.3). In the case of $\Delta = 0.4$, $a_0 = 4(\ln 3)$.

The interface energy, σ, for the equilibrium state is given by Allen and Cahn [101] and

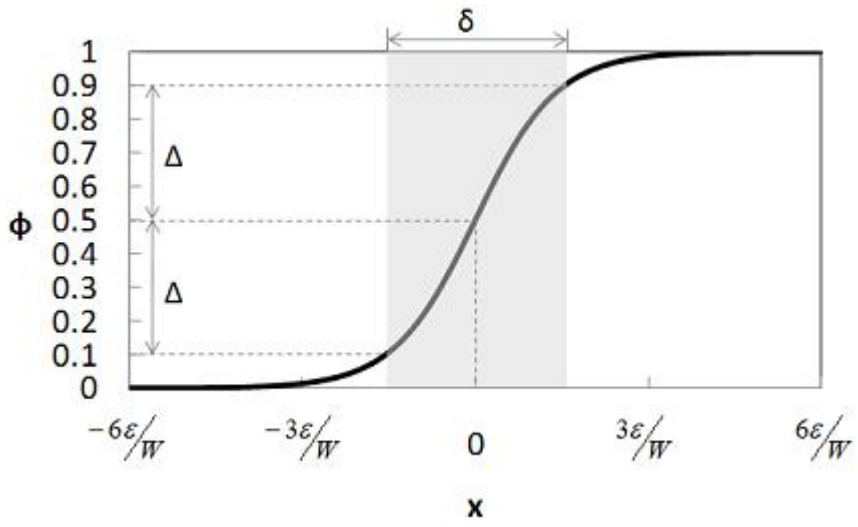

Figure B.3 Phase-field variable distribution as a function of the distance from the interface position where $\phi = 0.5$, calculated with equation B.36. δ represents the interface thickness when $\Delta = 0.4$.

others as

$$\sigma = \epsilon^2 \int_{-\infty}^{+\infty} (\nabla\phi)^2 dx = \epsilon\sqrt{2} \int_0^1 \sqrt{f} d\phi = \frac{\epsilon\sqrt{W}}{3\sqrt{2}} \tag{B.37}$$

where g has a form of equation (B.2).

According to the equation (B.36) and (B.37), both δ and σ are functions of ϵ and W. Therefore, we can express ϵ and W in terms of δ and σ as following:

$$W = \frac{3a_0\sigma}{\delta} \tag{B.38}$$

and

$$\epsilon^2 = \frac{6\sigma\delta}{a_0} \tag{B.39}$$

where σ is a material parameter and δ is a model parameter that we can choose. As mentioned in chapter 4.2, in the sharp-interface limit model, δ should be comparable to the capillary length, for physically reliable simulation results .

The only undecided parameter is the phase-field mobility, M_ϕ. This parameter is deter-

mined by mapping the steady-state one-dimensional phase field equation to the Gibbs-Thomson condition. At the steady state where the interface moves with a constant velocity, V, we can consider a moving boundary system in which the velocity of moving frame is V. The velocity, V, is $(-dz/dt)$ where z represents the coordination of the moving frame. Then, the one-dimensional steady state version of the phase-field equation (B.9) is

$$-V\frac{\partial\phi}{\partial z} = M_\phi\left[\epsilon^2(\frac{d^2\phi}{dz^2}) - W\frac{\partial g}{\partial\phi} - \frac{\partial h}{\partial\phi}\frac{L}{T_M}(T_M - T)\right] \tag{B.40}$$

Since the equilibrium state is assumed, the equation (B.31) gives,

$$V\frac{\partial\phi}{\partial z} = M_\phi\frac{\partial h}{\partial\phi}\frac{L}{T_M}\Delta T \tag{B.41}$$

where $\Delta T = T_M - T$. Multiplying by $d\phi/dz$, and integrating with z give

$$\begin{aligned}\int_{-\infty}^{+\infty} V\left(\frac{\partial\phi}{\partial z}\right)^2 dz &= \int_{-\infty}^{+\infty}\left[M_\phi\frac{\partial h}{\partial\phi}\frac{\partial\phi}{\partial z}\frac{L}{T_M}\Delta T\right]dz = \int_0^1\left[M_\phi\frac{L}{T_M}\Delta T\right]dh \\ &= M_\phi\frac{L}{T_M}\Delta T\int_0^1 dh = M_\phi\frac{L}{T_M}\Delta T\left[h(\phi)\right]_0^1 = M_\phi\frac{L}{T_M}\Delta T\end{aligned} \tag{B.42}$$

Here, we take advantage of simplicity of the sharp-interface limit model: the temperature across the interface region is uniform, i.e. ΔT =constant. Using equation (B.37), equation (B.41) yields

$$\frac{V\sigma}{\epsilon^2} = \frac{M_\phi L}{T_M}\Delta T \tag{B.43}$$

i.e.

$$V = \frac{\epsilon^2 M_\phi L}{T_M\sigma}\Delta T \tag{B.44}$$

Because the interface velocity is generally considered as $V = \mu\Delta T$ where μ is an interface mobility, the phase-field mobility for pure materials, M_ϕ, becomes

$$M_\phi = \frac{\mu\sigma T_M}{L\epsilon^2} = \frac{a_0\mu T_M}{6L\delta} \tag{B.45}$$

Note that the phase-field mobility can be expressed only with the material parameters and

input value of μ.

In case of binary alloys, M_ϕ and ϵ^2 in equation (B.21) and (B.22) can be expressed as concentration-weighted values, as following:

$$\begin{aligned} M_\phi &= (1-c)M_\phi^A + cM_\phi^B \\ \epsilon^2 &= (1-c)\epsilon^{A2} + c\epsilon^{B2} \end{aligned} \tag{B.46}$$

M_ϕ^A and M_ϕ^B are the phase field mobilities of pure A and B, and ϵ^{A2} and ϵ^{B2} are gradient penalty coefficients of pure A and B, respectively, which are expressed by equations (B.39) and (B.45), i.e.

$$\begin{aligned} M_\phi^A &= \frac{a_0 \mu^A T_M^A}{6L^A\delta} \\ M_\phi^B &= \frac{a_0 \mu^B T_M^B}{6L^B\delta} \\ \epsilon^{A2} &= \frac{6\sigma^A\delta}{a_0} \\ \epsilon^{B2} &= \frac{6\sigma^B\delta}{a_0} \end{aligned} \tag{B.47}$$

The thin-interface limit model formulation

Pure materials

In the thin-interface limit model, temperature and/or concentration variations across the interface region are considered. That allows quantitative calculations even with rather unrealistically thick interface while δ should be comparable with the capillary length for quantitatively valid simulations in the sharp-interface limit.

To obtain the phase-field mobility, M_ϕ, in the thin-interface limit, the steady state diffusion equation in a moving frame is considered:

$$-V\nabla T = \alpha\nabla^2 T + \frac{V\Delta H_f}{C_P}\frac{\partial h(\phi)}{\partial\phi}\nabla\phi \tag{B.48}$$

where V is the steady state interface velocity, and z is in moving coordination frame with

velocity V, i.e. $V = dx/dz$. $z = 0$ at the middle of the interface region. This yields

$$\nabla T = -\frac{\alpha}{V}\nabla^2 T - \frac{\Delta H_f}{C_P}\frac{\partial h(\phi)}{\partial \phi}\nabla\phi \tag{B.49}$$

At the thin-interface limit where the interface thickness is much thinner that the thermal boundary length, i.e. $\alpha/V >> \delta$, the temperature difference across the interface is negligibly small. Then, the right-side therms are assumed as zero. Integration of this terms gives

$$T(x) = T_0 + Az - \frac{\Delta H}{C_P}\frac{V}{\alpha}\int_0^z h(\phi)dz \tag{B.50}$$

where T_0 is the temperature at $z = 0$, and A is an integration constant.

In the region of $\frac{\delta}{2} \leq |z| << \frac{\alpha}{V}$, at $z < -\frac{\delta}{2}$,

$$\int_0^z h(\phi)dz \approx -\int_{-\infty}^0 h(\phi)dz \tag{B.51}$$

, and at $z > \frac{\delta}{2}$

$$\int_0^z h(\phi)dz \approx z - \int_{-\infty}^0 h(\phi)dz \tag{B.52}$$

. These yield

$$T(z) = T_0 + Az + \frac{\Delta H}{C_P}\frac{V}{\alpha}\int_{-\infty}^0 h(\phi)dz \tag{B.53}$$

at $z < -\frac{\delta}{2}$, and

$$T(z) = T_0 + \left(A - \frac{\Delta H}{C_P}\frac{V}{\alpha}\right)z + \frac{\Delta H}{C_P}\frac{V}{\alpha}\int_{-\infty}^0 h(\phi)dz \tag{B.54}$$

at $z > \frac{\delta}{2}$. Extension of these two temperature distributions should match at $z = 0$, i.e.

$$T(0) = T_0^* = T_0 + \frac{\Delta H}{C_P}\frac{V}{\alpha}\int_{-\infty}^0 h(\phi)dz \tag{B.55}$$

where T_0^* is the extended temperature at $z = 0$ from $|z| > \frac{\delta}{2}$. Then, the equation (B.50) as a function of T_0^* is

$$T(z) = T_0^* + Az - \frac{\Delta H}{C_P}\frac{V}{\alpha}\int_{-\infty}^z h(\phi)dz \tag{B.56}$$

This is the temperature profile in the thin-interface limit.

Using the temperature distribution in equation (B.56), the phase-field mobility parameter, M_ϕ, will be calculated. While ΔT across an interface for the sharp-interface limit condition is constant in equation (B.41), it is a function of z for this thin-interface limit, i.e. $\Delta T = T_M - T(z)$ where $T(z)$ as in the equation (B.56). Multiplied by $d\phi/dz$, integrated with z, and applied with the equation (B.56) for $T(z)$, the equation (B.41) yields

$$\Delta T = T_M - T_0^* = V\left[\frac{T_M\sigma}{M_\phi\epsilon^2\Delta H} - \frac{\Delta H}{C_P\alpha}\frac{\epsilon}{\sqrt{2W}}\int_0^1 \frac{h(\phi)\left[1-h(\phi)\right]}{\sqrt{g(\phi)}}d\phi\right] \tag{B.57}$$

Since this undercooling is the kinetic undercooling which equals $V\beta$, this gives the expression for M_ϕ as following

$$M_\phi^{-1} = \frac{\epsilon^2\Delta H}{T_M\sigma}\left[\beta + \frac{\Delta H}{C_P\alpha}\frac{\epsilon}{\sqrt{2W}}\int_0^1 \frac{h(\phi)\left[1-h(\phi)\right]}{\sqrt{g(\phi)}}d\phi\right] \tag{B.58}$$

Binary alloys

In case of alloys, the phase-field mobility parameter, M_ϕ, can be calculated by the same way as the pure material case, by using a solute diffusion equation instead of a thermal diffusion equation. The difference of solutal diffusivities in solid and liquid phases are, however, several orders, and this is much bigger than the difference of thermal diffusivities. As a thick interface is used, this big diffusivity difference between two adjacent phases causes several spurious interface kinetics and solute trapping. Karma [113] resolved this problem by introducing the anti-trapping current term in the phase-field evolution equation. This term gives a counterflux against unphysical solute trapping flux. Although this work is for the specific case of a dilute, one-sided binary alloys, Tong *et al.* showed that the same forms of the governing equations can be effectively valid for non-dilute alloys. Their governing equations are as following [122]:

$$\tau(T)\eta(\hat{n})^2\frac{\partial\phi}{\partial t} = \nabla\cdot\left[W(T)^2\eta(\hat{n})^2\nabla\phi\right] + \phi - \phi^3 - \lambda(T)(1-\phi^2)^2U + \nabla\cdot\left(\left|\nabla\phi\right|^2 W(T)^2\eta(\hat{n})\frac{\partial\eta(\hat{n})}{\partial(\nabla\phi)}\right) \tag{B.59}$$

$$\left(\frac{1+k(T)}{2}-\frac{1-k(T)}{2}\phi\right)\frac{\partial U}{\partial t}=\nabla\cdot\left(D(T)\frac{1-\phi}{2}\nabla U+\frac{1}{2\sqrt{2}}\left\{1+\left[1-k(T)\right]U\right\}\frac{\partial\phi}{\partial t}\frac{\nabla\phi}{|\nabla\phi|}\right)+\frac{1}{2}\left\{1+\left[1-k(T)\right]U\right\}\frac{\partial\phi}{\partial t} \tag{B.60}$$

where $\phi=+1$ in solid phase, $\phi=-1$ in liquid phase, τ is the time scale parameter related to the interface kinetic attachment, η is the anisotropy term, W is the interface thickness parameter which corresponds to $\delta/4$, λ is the coupling parameter between the phase-field and chemical diffusion dynamics, and U is the normalized supersaturation. According to the thin-interface limit analysis [115], the relationship between λ, τ, and W is

$$W=\frac{d_0\lambda}{a_1} \tag{B.61}$$

and

$$\tau=\frac{a_2\lambda}{D}W^2 \tag{B.62}$$

where the capillary length, $d_0=\Gamma/\Delta T$, $\Gamma=\sigma T/L$, $\Delta T=T_L^e(c_S^e)-T$, $a_1=0.8839$, and $a_2=0.6267$ [113]. $U=\left(e^u-1\right)/\left[1-k\right]$, and $u=\ln\left\{(2c/c_L^e)/\left(1+k-\left[1-k\right]\phi\right)\right\}$.

Other Issues

General form of free energy density equation

In case of regular binary alloys, the Gibbs free energy equation which is calculated by CALPHAD method can be used for the Phase-field simulation other than the using enthalpy of mixing term. The free energy equation from CALPHAD is given as:

$$G_\phi=\sum_{i=A,B}x^{i\circ}G_\phi^i+RT\sum_{i=A,B}x^i\ln x^i+{}^{xs}G_\phi \tag{B.63}$$

where x^i represents the mole fraction, ${}^\circ G_\phi^i$ is the molar Gibbs free energy for pure element i with the structure ϕ, and ${}^{xs}G_\phi^i$ is the excess molar Gibbs free energy, respectively. The excess

molar Gibbs free energy can be given by

$$^{xs}G_{\phi} = x^A x^B \sum_{j=0}^{n} {}^{j}L_{\phi}^{A,B}(x^A - x^B)^j \tag{B.64}$$

For the liquid and solid phases, the free energy densities are

$$f_L = \left\{ \left[x^A {}^{\circ}G_L^A + x^B {}^{\circ}G_L^B\right] + RT\left[x^A \ln x^A + x^B \ln x^B\right] + x^A x^B \left[\sum_{j=0}^{n} {}^{j}L_L^{A,B}(x^A - x^B)^j\right] \right\} / v_m \tag{B.65}$$

and

$$f_S = \left\{ \left[x^A {}^{\circ}G_S^A + x^B {}^{\circ}G_S^B\right] + RT\left[x^A \ln x^A + x^B \ln x^B\right] + x^A x^B \left[\sum_{j=0}^{n} {}^{j}L_S^{A,B}(x^A - x^B)^j\right] \right\} / v_m \tag{B.66}$$

Therefore, the free energy density difference between solid and liquid phases for the function of temperature and atomic fraction of concentration could be

$$f_L - f_S = \left\{ \begin{array}{l} \left[(1-c)({}^{\circ}G_L^A - {}^{\circ}G_S^A) + c({}^{\circ}G_L^B - {}^{\circ}G_S^B)\right] \\ \quad +(1-c)c\left[\sum_{j=0}^{n}({}^{j}L_L^{A,B} - {}^{j}L_S^{A,B})((1-c)-c)^j\right] \end{array} \right\} / v_m \tag{B.67}$$

This can be used for the phase-field evolution equation (B.9) and for the Cahn-Hilliard equation (B.27).

Anisotropy

Concerning the anisotropy of interfacial energy, the gradient energy penalty coefficient, ϵ, is a function of the orientation of the interface normal, θ, which is the angle between the direction of normal vector of interface and a reference coordination axis, i.e.

$$\epsilon = \bar{\epsilon}\eta(\theta) \tag{B.68}$$

where $\bar{\epsilon}$ is an average gradient energy penalty coefficient, and η is an interface orientation-dependent term. For an 4-fold symmetric anisotropy of cubic crystals in two-dimensional

system,

$$\eta = 1 + \epsilon_4 cos(4\theta) \tag{B.69}$$

. Considering more general three-dimensional anisotropies of interfacial stiffness, η can be a function of the components of the interface normal, i.e.

$$\eta(\hat{n}) = 1 + \epsilon_1 \left(\sum_{i=1}^{3} n_i^4 - \frac{3}{5} \right) + \epsilon_2 \left(3 \sum_{i=1}^{3} n_i^4 + 66 n_1^2 n_2^2 n_3^2 - \frac{17}{7} \right) \cdots \tag{B.70}$$

With this ϵ in equation (B.68), the phase-field evolution equation for binary alloys for two-dimensional growth in the sharp-interface limit (Eq. 4.4) can be

$$\begin{aligned} \frac{\partial \phi}{\partial t} &= -M_\phi \frac{\delta F}{\delta \phi} = M_\phi \left[\nabla \cdot (\epsilon^2 \nabla \phi) - \frac{\partial f}{\partial \phi} \right] \\ &= M_\phi \left[-\frac{\partial f}{\partial \phi} + \bar{\epsilon}^2 \nabla \cdot (\eta^2 \nabla \phi) - \bar{\epsilon}^2 \frac{\partial}{\partial x} \left(\eta \eta' \frac{\partial \phi}{\partial y} \right) + \bar{\epsilon}^2 \frac{\partial}{\partial y} \left(\eta \eta' \frac{\partial \phi}{\partial x} \right) \right] \end{aligned} \tag{B.71}$$

For a three-dimensional simulation of ideal binary alloys using the sharp-interface limit model, the evolution equation for ϕ-field can be described by equation (B.22) and (B.68) as

$$\frac{\partial \phi}{\partial t} = -M_\phi \begin{bmatrix} W \frac{\partial g}{\partial \phi} + \frac{\partial h}{\partial \phi} \left\{ (1-c) \frac{L^A}{T_M^A} (T_M^A - T) + c \frac{L^B}{T_M^B} (T_M^B - T) \right\} - \bar{\epsilon}^2 \nabla \cdot (\eta^2 \nabla \phi) \\ -\bar{\epsilon}^2 \frac{\partial}{\partial x} \left(|\nabla \phi|^2 \eta \frac{\partial \eta}{\partial \phi_x} \right) - \bar{\epsilon}^2 \frac{\partial}{\partial y} \left(|\nabla \phi|^2 \eta \frac{\partial \eta}{\partial \phi_y} \right) - \bar{\epsilon}^2 \frac{\partial}{\partial z} \left(|\nabla \phi|^2 \eta \frac{\partial \eta}{\partial \phi_z} \right) \end{bmatrix} \tag{B.72}$$

and for non-ideal binary alloys using the regular solution model, combining equations (B.21) and (B.68) yields

$$\frac{\partial \phi}{\partial t} = -M_\phi \begin{bmatrix} W \frac{\partial g}{\partial \phi} + \frac{\partial h}{\partial \phi} \left\{ (1-c) \frac{L^A}{T_M^A} (T_M^A - T) + c \frac{L^B}{T_M^B} (T_M^B - T) + c(1-c)(\Omega_L - \Omega_S) \right\} \\ -\bar{\epsilon}^2 \nabla \cdot (\eta^2 \nabla \phi) - \bar{\epsilon}^2 \frac{\partial}{\partial x} \left(|\nabla \phi|^2 \eta \frac{\partial \eta}{\partial \phi_x} \right) - \bar{\epsilon}^2 \frac{\partial}{\partial y} \left(|\nabla \phi|^2 \eta \frac{\partial \eta}{\partial \phi_y} \right) - \bar{\epsilon}^2 \frac{\partial}{\partial z} \left(|\nabla \phi|^2 \eta \frac{\partial \eta}{\partial \phi_z} \right) \end{bmatrix} \tag{B.73}$$

Noise

On the purpose of provoking interface instability to produce complex dendrite shapes as in the real nature, we can give some random noise to the free energy density distribution within the interface region in a *ad hoc* way which is applied by Warren and Boettinger [108]

as following;

$$\frac{\partial \phi}{\partial t} = M_\phi(\epsilon^2 \nabla^2 \phi - \frac{\partial f}{\partial \phi}) \rightarrow \frac{\partial \phi}{\partial t} = M_\phi \left\{ \epsilon^2 \nabla^2 \phi - \frac{\partial f}{\partial \phi}(1 - 16g\alpha r) \right\} \tag{B.74}$$

where α is maximum degree of noise amplitude, r is a random number between -1 and +1, and $16g$ has maximum value of unity at the interface and zero in the bulk phases.

BIBLIOGRAPHY

[1] J. C. Baker and J. W. Cahn, in *Solidification* (Am. Soc. Metals, Metals Park, OH, 1971), p. 23.

[2] M. J. Aziz, *J. Appl. Phys.*, *53*, 1158 (1982).

[3] P. Galenko and S. Sobolev, *Phys. Rev. E*, *55*, 343 (1997).

[4] J. W. Rutter and B. Chalmers, *Can. J. Phys.*, *31*, 15 (1953).

[5] L. R. Morris and W. C. Winegard, *J. Cryst. Growth*, *5*, 361 (1969).

[6] H. D. Keith and F. J. Padden, Jr., *J. Appl. Phys.*, *34*, 2409 (1963).

[7] W. A. Tiller and J. W. Rutter, *Can. J. Phys.*, *34*, 96 (1956).

[8] W. A. Tiller, K. A. Jackson, J. W. Rutter, and B. Chalmers, *Acta Metall.*, *1*, 428 (1953).

[9] V. G. Smith, W. A. Tiller, and J. W. Rutter, *Can. J. Phys.*, *33*, 723 (1955).

[10] W. W. Mullins and R. F. Sekerka, *J. Appl. Phys.*, *35*, 444 (1964).

[11] R. Trivedi and K. Somboonsuk, *Acta metall.*, *33*, 1061 (1985).

[12] K. Somboonsuk, J. T. Mason, and R. Trivedi, *Metall. Trans. A*, *15*, 967 (1984).

[13] J. A. Warren and J. S. Langer, *Phys. Rev. E*, *47*, 2702 (1993).

[14] W. Losert, B. Q. Shi, and H. Z. Cummins, *Proc. Natl. Acad. Sci. USA*, *95*, 431 (1998).

[15] W. Losert, B. Q. Shi, and H. Z. Cummins, *Proc. Natl. Acad. Sci. USA*, *95*, 439 (1998).

[16] N. Bergion, R. Trivedi, B. Billia, B. Echebarria, A. Karma, S. Liu, C. Weiss, and N. Mangelinck, *Adv. Space Res.*, *36*, 80 (2005).

[17] P. Duwez, R. H. Willens, and W. Klement, Jr., *J. Appl. Phys.*, *31*, 1136/1137 (1960).

[18] H. Biloni and B. Chalmers, *Trans. Soc. Min. Eng. AIME*, *233*, 373 (1965).

[19] J. C. Baker and J. W. Cahn, *Acta Metall.*, *17*, 575 (1969).

[20] C. W. White, J. Narayan, and R. T. Young, *Science*, *204*, 461 (1979).

[21] K. A. Jackson and H. J. Leamy, *AIP Conf. Proc.*, *50*, 102 (1979).

[22] C. W. White, S. R. Wilson, B. R. Appleton, and F. W. Young, Jr., *J. Appl. Phys.*, *51*, 738 (1980).

[23] C. W. White, B. R. Appleton, B. Stritzker, D. M. Zehner, and S. R. Wilson, *Mater. Res. Soc. Symp. Proc.*, *1*, 59 (1981).

[24] P. Baeri, J. M. Poate, S. U. Campisano, G. Foti, E. Rimini, and A. G. Cullis, *Appl. Phys. Lett.*, *37*, 912 (1980).

[25] W. J. Boettinger, S. R. Coriell, and R. F. Sekerka, *Mater. Sci. Eng.*, *65*, 27 (1984).

[26] W. J. Boettinger and S. R. Coriell, in *Science and Technology of the Undercooled Melt*, edited by P. R. Sahm, H. Jones, and C. M. Adam (Nato ASI Series, Montinus Nijhoff, Boston, MA, 1986) 81.

[27] D. Turnbull, *J. Phys. Chem.*, *66*, 609 (1962).

[28] M. J. Aziz, J. Y. Tsao, M. O. Thompson, P. S. Peercy, and C. W. White, *Phys. Rev. Lett.*, *56*, 1489 (1986).

[29] M. J. Aziz, J. Y. Tsao, M. O. Thompson, P. S. Peercy, C. W. White, and W. H. Christie, *Mat. Res. Soc. Symp. Proc.*, *35*, 153 (1985).

[30] D. E. Hoglund, M. J. Aziz, S. R. Stiffler, M. O. Thompson, J. Y. Tsao, and P. S. Peercy, *J. Cryst. Growth*, *109*, 107 (1991).

[31] P. M. Smith, R. Reitano, and M. J. Aziz, *Mat. Res. Soc. Symp. Proc.*, *279*, 749 (1993).

[32] P. M. Smith and M. J. Aziz, *Acta Metall. Mater.*, *42*, 3515 (1994).

[33] J. A. Kittl, M. J. Aziz, D. P. Brunco, and M. O. Thompson, *J. Cryst. Growth*, *148*, 172 (1995).

[34] D. P. Brunco, M. O. Thompson, D. E. Hoglund, M. J. Aziz, and H. -J. Gossmann,*J. Appl. Phys.*, *78*, 1575 (1995).

[35] C. B. Arnold, M. J. Aziz, M. Schwarz, and D. M. Herlach, *Phys. Rev. B*, *59*, 334 (1999).

[36] J. A. Kittl, P. G. Sanders, M. J. Aziz, D. P. Brunco, and M. O. Thompson, *Acta Mater.*, *48*, 4797 (2000).

[37] D. M. Herlach, *Mater. Sci. Eng. A*, *226-228*, 348 (1997).

[38] R. Willnecker, D. M. Herlach, and B. Feuerbacher, *Phys. Rev. Lett.*, *62*, 2707 (1989).

[39] D. M. Herlach, *Ann. Rev. Mater. Sci.*, *21*, 23 (1991).

[40] K. Eckler, R. F. Cochrane, D. M. Herlach, B. Feuerbacher, and M. Jurisch, *Phys. Rev. B*, *45*, 5019 (1992).

[41] K. Eckler, D. M. Herlach, R. G. Hamerton, and A, L. Greer, *Mater. Sci. Eng. A*, *133*, 730 (1991).

[42] M. Barth, K. Eckler, D. M. Herlach, and H. Alexander, *Mater. Sci. Eng. A*, *133*, 790 (1991).

[43] R. F. Cochrane, A. L. Greer, K. Eckler, and D. M. Herlach, *Mater. Sci. Eng. A*, *133*, 698 (1991).

[44] D. M. Herlach, *Mater. Sci. Eng.*, *R12*, 177 (1994).

[45] M. Barth, B. Wei, D. M. Herlach, and B. Feuerbacher, *Mater. Sci. Eng. A*, *178*, 305 (1994).

[46] W. Loser, T. Volkmann, and D. M. Herlach, *Mater. Sci. Eng. A*, *178*, 163 (1994).

[47] P. R. Algoso, W. H. Hofmeister, and R. J. Bayuzick, *Acta Mater.*, *51*, 4307 (2003).

[48] A. Altgibers, W. Hofmeister, and R. Bayuzick, *Mater. Sci. Eng. A*, *360*, 26 (2003).

[49] J. Lipton, M. E. Glicksman, and W. Kurz, *Mater. Sci. Eng.*, *65*, 57 (1984).

[50] J. Lipton, W. Kurz, and R. Trivedi, *Acta Metall.*, *35*, 957 (1987).

[51] W. J. Boettinger, S. R. Coriell, and R. Trivedi, in *Rapid solidification processing: principles and technologies*, edited by R. Mehrabian and P. A. Parrish (Claitor's Publishing, Baton Rouge, LA, 1988), p. 13.

[52] J. S. Langer and H. Müller-Krumbhaar, *Acta Metall.*, *26*, 1681 (1978).

[53] M. J. Aziz and T. Kaplan, *Acta Metall.*, *36*, 2335 (1988).

[54] M. Carrard, M. Gremaud, M. Zimmermann, and W. Kurz, *Acta Metall. Mater.*, *40*, 5, 983 (1992).

[55] P. K. Galenko, *Phys. Rev. E*, *76*, 031606 (2007).

[56] P. K. Galenko and D. A. Danilov, *Phys. Lett. A*, *235*, 271 (1997).

[57] P. K. Galenko and D. A. Danilov, *J. Cryst. Growth*, *197*, 992 (1999).

[58] H. Wang, F. Liu, Z. Chen, G. Yang, and Y. Zhou, *Acta Mater.*, *55*, 497 (2007).

[59] K. Eckler, D. M. Herlach, and M. J. Aziz, *Acta Metall. Mater.*, *42*, 975 (1994).

[60] J. Bragard, A. Karma, Y. H. Lee, and M. Plapp, *Interface Sci.*, *10*, 121 (2002).

[61] J. W. Lum, D. M. Matson, and M. C. Flemings, *Metall. Mater. Trans. B*, *27*, 865 (1996).

[62] D. M. Matson, in *Solidification*, edited by S. P. Marsh, J. A. Dantzig, R. Trivedi, W. Hofmeister, M. G. Chu, E. J. Lavernia, and J. H. Chun (The Mineral, Metals and Materials Society, Warrendale, PA, 1998), p. 233.

[63] P. K. Galenko, S. Reutzel, D. M. Herlach, D. Danilov, and B. Nestler, *Acta Mater.*, *55*, 6834 (2007).

[64] P. K. Galenko, S. Reutzel, D. M. Herlach, S. G. Fries, I. Steinbach, and M. Apel, *Acta Mater.*, *57*, 6166 (2009).

[65] G. V. S. Sastry, and C. Suryanarayana, *Mater. Sci. Eng.*, *47*, 193 (1981).

[66] W. J. Boettinger, D. Shechtman, R. J. Schaefer, and F. S. Biancaniello, *Metall. Trans. A*, *15*, 55 (1984).

[67] W. A. Elliott, F. P. Gagliano, and G. Krauss, *Appl. Phys. Lett.*, *21*, 23 (1972).

[68] S. M. Copley, M. Bass, E. W. V. Stryland, D. G. Beck, and O. Esquivel, *Rapidly Quenched Metals III*, *1*, 147 (1978).

[69] D. G. Beck, S. M. Copley, and M. Bass, *Metall. Mater. Trans. A*, *12*, 1687 (1981).

[70] D. G. Beck, S. M. Copley, and M. Bass, *Metall. Mater. Trans. A*, *13*, 1879 (1982).

[71] D. J. Thoma, T. K. Glasgow, S. N. Tewari, J. H. Perepezko, and N. Jayaraman, *Mater. Sci. Eng.*, *98*, 89 (1988).

[72] T. Sato, T. T. Long, H. Tezuka, A. Kamio, and T. Takahashi, *J. Japan Inst. Metals*, *48*, 748 (1984).

[73] M. Gremaud, M. Carrard, and W. Kurz, *Acta Metall. Mater.*, *39*, 7, 1431 (1991).

[74] S. K. Pandey, D. K. Gangopadhyay, and C. Suryanarayana, *Z. Metallk.*, *77*, 12 (1986).

[75] D. B. Williams and J. W. Edington, in *Rapidly Quenched Metals* (edited by N. J. Grant and B. C. Giessen), 135 (1976).

[76] M. Zimmermann, M. Carrard, and W. Kurz, *Proc. 2nd Eur. Conf. on Laser Treat. of Mater*, DVS-Berchte No.113, 143 (1988)

[77] S. R. Coriell and R. F. Sekerka, *J. Cryst. Growth*, *61*, 499 (1983).

[78] G. J. Merchant and S. H. Davis, *Acta Metall. Mater.*, *38*, 2683 (1990).

[79] W. Kurz and R. Trivedi, *Acta Metall. Mater.*, *38*, 1 (1990).

[80] A. Karma and A. Sarkissian, *Phys. Rev. Lett.*, *68*, 17, 2616 (1992).

[81] A. Karma, and A. Sarkissian, *Phys. Rev. E*, *47*, 1, 513 (1993).

[82] D. A. Huntley and S. H. Davis, *Phys. Rev. B*, *53*, 3132 (1990).

[83] M. Gremaud, M. Carrard, and W. Kruz, *Acta Metall. Mater.*, *38*, 2587 (1990).

[84] M. Zimmermann, M. Carrard, and W. Kurz, *Acta Metall.*, *37*, 3305 (1989).

[85] M. Zimmermann, M. Carrard, M. Gremaud, and W. Kurz, *Mater. Sci. Eng. A*, *134*, 1278 (1991).

[86] S. C. Gill and W. Kurz, *Acta Metall. Mater.*, *41*, 3563 (1993).

[87] J. S. Langer, *Rev. Mod. Phys.*, *52*, 1 (1980).

[88] W. J. Boettinger and J. A. Warren, *J. Cryst. Growth*, *200*, 583 (1999).

[89] S. G. Kim and W. T. Kim, *Mater. Sci. Eng. A*, *A304-306*, 281 (2001).

[90] J. Fan, M. Greenwood, M. Haataja, and N. Provatas, *Phys. Rev. E*, *74*, 031602 (2006).

[91] A. A. Wheeler, B. T. Murray, and R. J. Schaefer, *Physica D*, *66*, 243 (1993).

[92] N. A. Ahmad, A. A. Wheeler, W. J. Boettinger, and G. B. McFadden, *Phys. Rev. E*, *58*, 3436 (1998).

[93] D. Danilov and B. Nestler, *Acta Mater.*, *54*, 4659 (2006).

[94] M. Conti, *Phys. Rev. E*, *58*, 2071 (1998).

[95] K. Eckler, F. Gartner, H. Assadi, A. F. Norman, A. L. Greer, and D. M. Herlach, *Mater. Sci. Eng. A*, *226-228*, 410 (1997).

[96] J. D. van der Waals, *Verhandel. Konink, Akad. Weten. Amsterdam (sect. 1)*, *1*, (8), 56 (1893).

[97] J. S. Rowlinson, *J. Stat. Phys.*, *20*, 197 (1979).

[98] J. W. Cahn and J. E. Hilliard, *J. Chem. Phys.*, *28*, 258 (1958).

[99] W. J. Boettinger, J. A. Warren, C. Beckermann, and A. Karma, *Annu. Rev. Mater. Res.*, *32*, 163 (2002).

[100] S. M. Allen and J. W. Cahn, *J. Phys. Paris*, *38*, C7-51 (1977).

[101] S. M. Allen and J. W. Cahn, *Acta Metall.*, *27*, 1085 (1979).

[102] J. W. Cahn, *Acta Metall.*, *9*, 795 (1961).

[103] G. Caginalp, *Phys. Rev. A.*, *39*, 5887 (1989).

[104] A. A. Wheeler, W. J. Boettinger, and G. B. McFadden, *Phys. Rev. A*, *45*, 7424 (1992).

[105] S. L. Wang, R. F. Sekerka, A. A. Wheeler, B. T. Murray, S. R. Coriell, R. J. Braun, and G. B. McFadden, *Physica D*, 69, 189 (1993).

[106] A. Karma and W. J. Rappel, *Phys. Rev. E*, *53*, R3017 (1996).

[107] R. J. Braun, G. B. McFadden, and S. R. Coriell, *Phys. Rev. E*, *49*, 4336 (1994).

[108] J. A. Warren and W. J. Boettinger, *Acta Metall. Mater.*, *43*, 689 (1995).

[109] S. L. Wang and R. F. Sekerka, *Phys. Rev. E*, *53*, 3760 (1996).

[110] S. L. Wang and R. F. Sekerka, *J. Comput. Phys.*, *127*, 110 (1996).

[111] A. Karma and W. J. Rappel, *Phys. Rev. E*, *57*, 4323 (1998).

[112] R. F. Almgren, *SIAM J. Appl. Math.*, *59*, 2086 (1999).

[113] A. Karma, *Phys. Rev. Lett.*, *87*, 115701 (2001).

[114] R. Folch and M. Plapp, *Phys. Rev. E*, *72*, 011602 (2005).

[115] B. Echebarria, A. Folch, A. Karma, and M. Plapp, *Phys. Rev. E*, *70*, 0616604 (2004).

[116] M. Greenwood, M. Haataja, and N. Provatas, *Phys. Rev. Lett.*, *93*, 246101 (2004).

[117] J. C. Ramirez, C. Beckermann, A. Karma, and H. J. Diepers, *Phys. Rev. E*, *69*, 051607 (2004).

[118] J. C. Ramirez and C. Beckermann, *Acta Mater.*, *53*, 1721 (2005).

[119] A. Badillo and C. Beckermann, *Acta Mater.*, *54*, 2015 (2006).

[120] A. J. Pons, A. Karma, and S. Akamatsu, *et al.*, *Phys. Rev. E*, *75*, 021602 (2007).

[121] S. G. Kim, *Acta Mater.*, *55*, 4391 (2007).

[122] C. Tong, M. Greenwood, and N. Provatas, *Phys. Rev. B*, *77*, 064112 (2008).

[123] J. Agren, *Acta Metall.*, *37*, 181 (1989).

[124] S. L. Sobolev, *Phys. Rev. E*, *55*, 6845 (1997).

[125] M. Hillert, *Acta Mater.*, *52*, 5289 (1999).

[126] J. Svoboda, F. D. Fischer, and E. Gamsjager, *Acta Mater.*, *50*, 967 (2002).

[127] P. K. Galenko, *Phys. Rev. B*, *65*, 144103 (2002).

[128] M. Hillert, *Acta Mater.*, *52*, 5289 (2004).

[129] S. Li, J. Zhang, and P. Wu, *Scripta Mater.*, *62*, 716 (2010).

[130] D. Danilov and B. Nestler, *Phys. Rev. Lett.*, *93*, 215501 (2004).

[131] S. G. Kim, W. T. Kim, and T. Suzuki, *Phys. Rev. E*, *60*, 7186 (1999).